



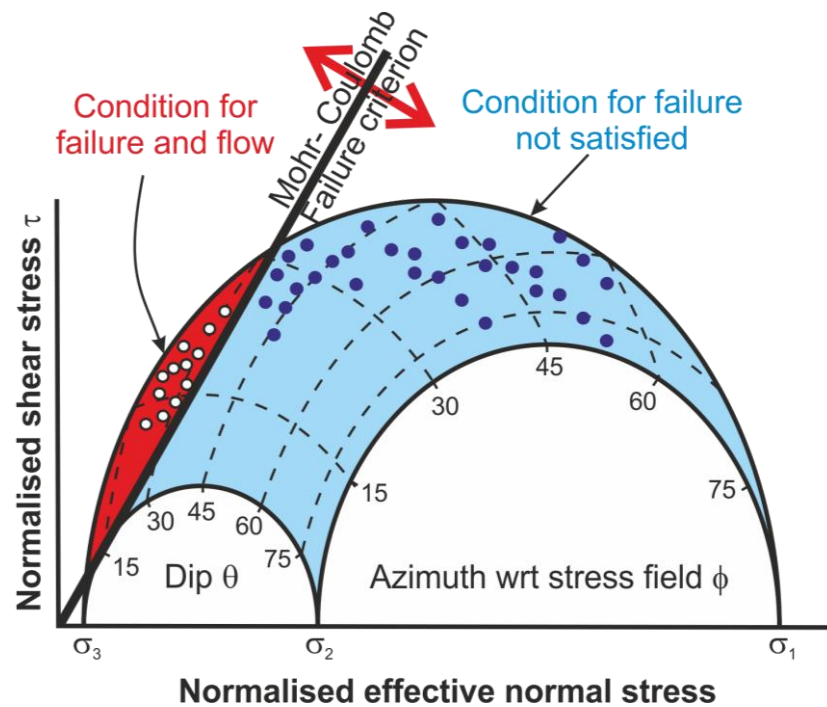
**British  
Geological Survey**

NATURAL ENVIRONMENT RESEARCH COUNCIL

# Final Report of FORGE WP4.1.2: Verification of critical stress theory applied to repository concepts

Minerals and Waste Programme

Commissioned Report CR/13/001





BRITISH GEOLOGICAL SURVEY

MINERALS AND WASTE PROGRAMME

COMMISSIONED REPORT CR/13/001

# Final Report of FORGE WP4.1.2: Verification of critical stress theory applied to repository concepts

R.J. Cuss, S. Sathar, and J.F. Harrington

## *Keywords*

fracture, transmissivity,  
permeability, kaolinite, critical  
stress theory.

## *Front cover*

The three-dimensional Mohr  
diagram displaying the horizontal  
stress and normal stress on faults  
and fracture surface with respect  
to the in situ stress field.

## *Bibliographical reference*

CUSS, R.J., SATHAR, S., AND  
HARRINGTON, J.F. 2013. Final  
Report of FORGE WP4.1.2:  
Verification of critical stress  
theory applied to repository  
concepts. *British Geological  
Survey Commissioned Report*,  
CR/13/001. 105pp.

Copyright in materials derived  
from the British Geological  
Survey's work is owned by the  
Natural Environment Research  
Council (NERC) and/or the  
authority that commissioned the  
work. You may not copy or adapt  
this publication without first  
obtaining permission. Contact the  
BGS Intellectual Property Rights  
Section, British Geological  
Survey, Keyworth,  
e-mail [ipr@bgs.ac.uk](mailto:ipr@bgs.ac.uk). You may  
quote extracts of a reasonable  
length without prior permission,  
provided a full acknowledgement  
is given of the source of the  
extract.

© NERC 2013. All rights reserved

Keyworth, Nottingham British Geological Survey 2013

## BRITISH GEOLOGICAL SURVEY

The full range of our publications is available from BGS shops at Nottingham, Edinburgh, London and Cardiff (Welsh publications only) see contact details below or shop online at [www.geologyshop.com](http://www.geologyshop.com)

The London Information Office also maintains a reference collection of BGS publications, including maps, for consultation.

We publish an annual catalogue of our maps and other publications; this catalogue is available online or from any of the BGS shops.

*The British Geological Survey carries out the geological survey of Great Britain and Northern Ireland (the latter as an agency service for the government of Northern Ireland), and of the surrounding continental shelf, as well as basic research projects. It also undertakes programmes of technical aid in geology in developing countries.*

*The British Geological Survey is a component body of the Natural Environment Research Council.*

*British Geological Survey offices*

### **BGS Central Enquiries Desk**

Tel 0115 936 3143 Fax 0115 936 3276  
email [enquires@bgs.ac.uk](mailto:enquires@bgs.ac.uk)

### **Kingsley Dunham Centre, Keyworth, Nottingham NG12 5GG**

Tel 0115 936 3241 Fax 0115 936 3488  
email [sales@bgs.ac.uk](mailto:sales@bgs.ac.uk)

### **Murchison House, West Mains Road, Edinburgh EH9 3LA**

Tel 0131 667 1000 Fax 0131 668 2683  
email [scotsales@bgs.ac.uk](mailto:scotsales@bgs.ac.uk)

### **London Information Office at the Natural History Museum (Earth Galleries), Exhibition Road, South Kensington, London SW7 2DE**

Tel 020 7589 4090 Fax 020 7584 8270  
Tel 020 7942 5344/45 email [bgs london@bgs.ac.uk](mailto:bgs london@bgs.ac.uk)

### **Columbus House, Greenmeadow Springs, Tongwynlais, Cardiff CF15 7NE**

Tel 029 2052 1962 Fax 029 2052 1963

### **Forde House, Park Five Business Centre, Harrier Way, Sowton EX2 7HU**

Tel 01392 445271 Fax 01392 445371

### **Maclean Building, Crowmarsh Gifford, Wallingford OX10 8BB**

Tel 01491 838800 Fax 01491 692345

### **Geological Survey of Northern Ireland, Colby House, Stranmillis Court, Belfast BT9 5BF**

Tel 028 9038 8462 Fax 028 9038 8461

[www.bgs.ac.uk/gsni/](http://www.bgs.ac.uk/gsni/)

*Parent Body*

### **Natural Environment Research Council, Polaris House, North Star Avenue, Swindon SN2 1EU**

Tel 01793 411500 Fax 01793 411501  
[www.nerc.ac.uk](http://www.nerc.ac.uk)

Website [www.bgs.ac.uk](http://www.bgs.ac.uk)

Shop online at [www.geologyshop.com](http://www.geologyshop.com)

# Foreword

This report is the product of a study by the British Geological Survey (BGS) undertaken on behalf of the Nuclear Decommissioning Authority – Radioactive Waste Management Directorate (NDA-RWMD) and the European Union 7<sup>th</sup> Framework Euratom Programme under the auspices of the Fate of repository Gases (FORGE) project, to examine the validation of critical stress theory applied to repository concept and the influence of fracture/fault angle on gas flow properties.

# Acknowledgements

The study was undertaken by staff of the Minerals and Waste Programme of the BGS using the experimental facilities of the Transport Properties Research Laboratory (TPRL). Funding for the study was provided by the Nuclear Decommissioning Authority – Radioactive Waste Management Directorate (NDA-RWMD), the European Union (FORGE Project) and the British Geological Survey through its well-founded laboratory programme. The authors would like to thank the skilled staff of the Research & Development Workshops at the BGS, in particular Humphrey Wallis, for their design and construction of the experimental apparatus.

# Contents

<b>Foreword</b> .....	<b>i</b>
<b>Acknowledgements</b> .....	<b>i</b>
<b>Contents</b> .....	<b>i</b>
<b>Executive summary</b> .....	<b>vi</b>
<b>1 Introduction</b> .....	<b>1</b>
1.1 Common host rock types chosen for subsurface radioactive waste disposal .....	1
1.2 State of stress and distribution of fractures around the excavation tunnels in the EDZ .....	3
1.3 Critical Stress Theory and related fluid flow .....	5
<b>2 Experimental apparatus and methodology</b> .....	<b>9</b>
2.1 Angled Shear Rig (ASR) .....	9
2.2 Sample preparation and experiment assembly .....	12
2.3 Experimental procedure.....	12
2.4 Calculation of fracture transmissivity.....	15
2.5 Note on stress convention.....	16
<b>3 Observations and results</b> .....	<b>17</b>
3.1 Fracture transmissivity evolution during variations in vertical load .....	17
3.2 Fracture transmissivity evolution during shear.....	31
3.3 Investigation of fault-valve behaviour during gas flow.....	35
<b>4 The effect of slip-plane orientations on gas flow through gouge-filled fractures</b> .....	<b>40</b>

4.1	Experimental methodology.....	40
4.2	Gas breakthrough experiments on a slip plane orientation of 0°.....	41
4.3	Gas breakthrough experiments on a slip plane orientation of 15°.....	48
4.4	Gas breakthrough experiments on a slip plane orientation of 30°.....	53
4.5	Gas breakthrough experiments on a slip plane orientation of 45°.....	59
4.6	Results and discussion for tests conducted at different orientations.....	64
4.7	The effect of shear displacement on gas entry and subsequent gas flow.....	68
4.8	Comparing results for tests conducted on a slip plane orientation of 0° with and without active shear.....	71
4.9	The effect of rate of pressurisation on gas entry and subsequent gas flow.....	79
4.10	Results for tests conducted at increased injection rate.....	81
4.11	Is gas entry at different angles simply related to normal load?.....	84
<b>5</b>	<b>Time-lapse study of fracture flow.....</b>	<b>85</b>
5.2	Discussion on time-lapse observations.....	87
<b>6</b>	<b>Water content of the gouge material.....</b>	<b>88</b>
<b>7</b>	<b>Conclusions.....</b>	<b>89</b>
7.1	Loading-unloading tests.....	89
7.2	Gas breakthrough experiments.....	91
7.3	General observations.....	92
<b>8</b>	<b>References:.....</b>	<b>93</b>
<b>9</b>	<b>Appendix I.....</b>	<b>95</b>

## FIGURES

Figure 1 - Stress trajectories around a non-hydrostatically loaded circular opening, such as a tunnel, demonstrating the prevailing stress inhomogeneity adjacent to the tunnel wall (from Cuss, 1999).....	4
Figure 2 - Complex network of fractures in the EDZ. The density of fractures decreases away from the tunnel opening (from Bossart <i>et al.</i> , 2002; Bossart <i>et al.</i> , 2004).....	4
Figure 3 - Distribution of permeability in a tunnel at Mont Terri URL. Zones within 10 – 20 cm of the tunnel exhibited high permeability ( $1 \times 10^{-14} \text{ m}^2$ ) (from Bossart <i>et al.</i> , 2004). .....	5
Figure 4 - The three-dimensional Mohr diagram displaying the horizontal stress and normal stress on faults and fracture surface with respect to the <i>in situ</i> stress field.....	6
Figure 5 - Detailed <i>in situ</i> stress data from the Sellafield area illustrating that none of the fractures are critically stressed at the present time. ....	7
Figure 6 - Common friction test arrangements. ....	9
Figure 7 - Angled shear rig (ASR). .....	10
Figure 8 - Components of the top block.....	11
Figure 9 - Fluid injection circuit displaying the servo-controlled ISCO <sup>TM</sup> injection pump and the gas-water interface vessel used to inject helium into the idealised slip plane.....	11

Figure 10 - Plan-view of the slip plane with fluid injection port in the centre and two orthogonally located pore pressure sensor ports.....	15
Figure 11 - Results from test ASR_Tau01_30wLU.....	19
Figure 12 - Results from test ASR_Tau05_30wLU.....	21
Figure 13 –Detail of effect of temperature fluctuations during the unloading stages in experiment ASR_Tau05_30wLU .....	22
Figure 14 – Comparison of results from experiments ASR_Tau01_30wLU and ASR_Tau05_30wLU .....	23
Figure 15 – Results from experiment ASR_Tau07_30gLU.....	26
Figure 16 – Results from experiment ASR_Tau08_30gLU.....	27
Figure 17 – Results from experiment ASR_Tau14_30gLU.....	28
Figure 18 – Comparison of results from tests ASR_Tau07_30gLU, ASR_Tau08_30gLU, and ASR_Tau14_30gLU .....	29
Figure 19 – Comparison of the hydraulic and gas injection experiments during loading and unloading.....	31
Figure 20 - Results from stages 1 to 3 of test ASR_Tau02_30wLUS .....	32
Figure 21 - Results from stages 4 to 9 of the ASR_Tau02_30wLUS experiment.....	33
Figure 22 - Results from stages 8 and 9 of the ASR_Tau02_30wLUS experiment .....	33
Figure 23 – Summary of observations for test ASR_Tau02_30wLUS.....	34
Figure 24 - The effect of shearing on hydraulic flow, resulting in a 40% reduction in flow.....	35
Figure 25 - Results from the fault-valve behaviour test (ASR_Tau06_30gGI).....	36
Figure 26 – Stage 1 – 2 of the fault-valve behaviour test (ASR_Tau06_30gGI).....	36
Figure 27 – Stage 3 of the fault-valve behaviour test (ASR_Tau06_30gGI).....	38
Figure 28 - Stage 4 – 5 of the fault-valve behaviour test (ASR_Tau06_30gGI) .....	38
Figure 29 – Stage 6 – 7 of the fault-valve behaviour test (ASR_Tau06_30gGI).....	39
Figure 30 – Evolution of pore pressure within the slip plane during the fault-valve behaviour test (ASR_Tau06_30gGI) .....	39
Figure 31 – Results for gas injection test 5 / ASR_Tau15_00gGI.....	42
Figure 32 – Results for gas injection test 6 / ASR_Tau16_00gGI.....	43
Figure 33 – Results for gas injection test 7 / ASR_Tau17_00gGI.....	44
Figure 34 – Results for gas injection test 11 / ASR_Tau21_00gGI.....	45
Figure 35 – Results for gas injection test 12 / ASR_Tau22_00gGI.....	46
Figure 36 – Results for five gas injection tests conducted on a fracture oriented 0° to the slip plane.....	47
Figure 37 – Gas entry pressure predicted from the average flow at STP for five gas injection tests conducted on a fracture oriented 0° to the slip plane.....	48
Figure 38 – Results for gas injection test 8 / ASR_Tau18_15gGI.....	49
Figure 39 – Results for gas injection test 9 / ASR_Tau19_15gGI.....	50
Figure 40 – Results for gas injection test 10 / ASR_Tau20_15gGI.....	51

Figure 41 –Results for three gas injection tests conducted on a fracture oriented 15° to the slip plane .....	52
Figure 42 –Gas entry pressure predicted from the average flow at STP for three gas injection tests conducted on a fracture oriented 15° to the slip plane.....	53
Figure 43 – Results for gas injection test 1 / ASR_Tau09_30gGI.....	54
Figure 44 – Results for gas injection test 2 / ASR_Tau11_30gGI.....	55
Figure 45 – Results for gas injection test 3 / ASR_Tau12_30gGI.....	56
Figure 46 – Results for gas injection test 4 / ASR_Tau13_30gGI.....	57
Figure 47 –Results for four gas injection tests conducted on a fracture oriented 30° to the slip plane .....	58
Figure 48 – Gas entry pressure predicted from the average flow at STP for four gas injection tests conducted on a fracture oriented 30° to the slip plane.....	58
Figure 49 – Results for gas injection test 15 / ASR_Tau25_45gGI.....	60
Figure 50 – Results for gas injection test 16 / ASR_Tau26_45gGI.....	61
Figure 51 – Results for gas injection test 17 / ASR_Tau27_45gGI.....	62
Figure 52 –Results for three gas injection tests conducted on a fracture oriented 45° to the slip plane .....	63
Figure 53 – Gas entry pressure predicted from the average flow at STP for three gas injection tests conducted on a fracture oriented 45° to the slip plane.....	63
Figure 54 – Relationship of gas entry pressure determined from STP gas flow into the fracture for all tests .....	65
Figure 55 – Relationship of gas entry pressure determined from the ideal gas law for all tests...	66
Figure 56 – Comparison of results from the two methods used to determine gas entry pressure .....	67
Figure 57 – Results for gas injection test 18 / ASR_Tau28_00gGIS.....	69
Figure 58 – Results for gas injection test 19 / ASR_Tau29_00gGIS.....	70
Figure 59 – Comparing results for gas injection tests conducted on a fracture oriented 0° to the slip plane with and without active shear .....	71
Figure 60 – Comparing results for gas entry pressure predicted from the average flow at STP for gas injection tests conducted on a fracture oriented 0° to the slip plane with and without active shear.....	72
Figure 61 – Results for gas injection test 20 / ASR_Tau30_30gGIS.....	73
Figure 62 – Results for gas injection test 21 / ASR_Tau31_45gGIS.....	75
Figure 63 – Results for gas injection test 22 / ASR_ Tau32_15gGIS.....	76
Figure 64 –Results for five gas injection tests conducted with active shear.....	77
Figure 65 – Gas entry pressure for all tests showing the influence of shear.....	78
Figure 66 – Results for gas injection test 13 / ASR_Tau23_00gGI.....	80
Figure 67 – Results for gas injection test 14 / ASR_Tau24_00gGI.....	81
Figure 68 – Results for two gas injection tests conducted at higher gas injection rates, compared with five tests conducted on a fracture oriented 0° to the slip plane.....	82

Figure 69 – Gas entry pressure predicted from the average flow at STP for two tests conducted at higher gas injection rate, compared with five gas injection tests conducted on a fracture oriented 0° to the slip plane.....	83
Figure 70 – Gas entry pressure for all tests showing the influence of gas injection rate.....	83
Figure 71 – Comparing gas entry pressure with normal load on the fracture.....	84
Figure 72 – Time-lapse results for gas injection test 10 / ASR_Tau20_15gGI.....	85
Figure 73 – Time-lapse results for gas injection test 11 / ASR_Tau21_00gGI.....	86
Figure 74 – Time-lapse results for gas injection test 12 / ASR_Tau22_00g GI.....	86
Figure 75 – Time-lapse results for gas injection test 13 / ASR_Tau23_00g GI.....	87
Figure 76 – Time-lapse results for gas injection test 12 / ASR_Tau22_00g GI.....	87
Figure 77 – Water content of the kaolinite gouge material measured at five locations on the sample surface.....	88

## TABLES

Table 1 – List of all experiments undertaken as part of the current study.....	13
Table 2 - Variation in load cell reading during variation in ISCO syringe pump pressure.....	14
Table 3 - The loading and unloading stages in test ASR_Tau01_30wLU.....	18
Table 4 - The loading and unloading stages in test ASR_Tau05_30wLU.....	20
Table 5 – Loading and unloading stages during gas injection loading/unloading experiments ASR_Tau07_30gLU, ASR_Tau08_30gLU, and ASR_Tau14_30gLU.....	25
Table 6 – Experimental stages of test ASR_Tau02_30wLUS.....	31
Table 7 – The normal stress acting on the experimental slip plane at different orientations. The normal stress decreases as the slip plane orientation increases.....	40
Table 8 – List of gas-injection experiments conducted.....	41
Table 9 – Results for gas entry pressure for the five gas injection experiments conducted on a fracture oriented 0° to the slip-plane.....	48
Table 10 – Results for gas entry pressure for three gas injection experiments conducted at an angle of 15°.....	53
Table 11 – Results for gas entry pressure for four gas injection experiments conducted at an angle of 30°.....	59
Table 12 – Results for gas entry pressure for three gas injection experiments conducted at an angle of 45°.....	64
Table 13 – Results for gas entry pressure for all gas injection experiments.....	67
Table 14 – Results for gas entry pressure for all gas injection experiments conducted at 0°. @ with shear.....	72
Table 15 – Results for gas entry pressure for all gas injection experiments.....	77
Table 16 – Results for gas entry pressure for all gas injection experiments.....	82
Table 17 – Results for gas entry pressure for all gas injection experiments.....	95

## Executive summary

This report describes an experimental study of 48 separate experiments examining the validity of critical stress theory. Two main types of experiment were conducted: 1). Loading-unloading tests, where fracture flow was monitored at constant injection pressure as normal load was increased in steps to a given level and then reduced back to the starting stress state; 2). Gas breakthrough experiments, where gas injection pressure was increased in a pressure ramp at constant vertical load. These were conducted with and without active shear. It was found that critical stress theory is valid in predicting the preferential flow of gas in relation to the orientation of the fracture plane with respect to the maximum horizontal stress direction. However, loading unloading experiments showed that understanding the stress history of the rocks is of paramount importance and a mere knowledge of the current stress state is insufficient in accurately predicting the nature of fluid flow.

A total of 17 loading-unloading experiments were conducted, all on a 30° slip-plane. The main conclusions of this part of the study were; a). During a loading (vertical stress) and unloading cycle considerable hysteresis in flow was observed signifying the importance of stress history on fracture flow; b). For the case of gas injection the change in flow is chaotic at low normal loads, whereas for water injection the flow reduces smoothly with increased normal load; c). Hysteresis in horizontal stress observed during unloading demonstrates the importance of the ratio between horizontal stress and vertical stress and its control on flow; d). Differences have been observed between injection fluids (water and helium), especially the hysteresis observed in flow. For water injection flow is only partially recovered during unloading, whereas for gas enhanced flow is seen at low normal loads.

A total of 26 gas breakthrough experiments were conducted on 0°, 15°, 30°, and 45° discontinuities; both with and without active shear. All tests were conducted in an identical manner. The main conclusions of this part of the study were; a). During gas breakthrough experiments episodic flow/fault valve behaviour was seen with a decrease in subsequent peak pressures and the form of the pressure response was different during subsequent breakthrough events; b). Repeat gas injection testing had shown a consistent gas entry pressure but considerably different, non-repeatable, gas peak pressures; c). Differences in gas entry pressure were seen dependent on the orientation of the fracture; d). Shear can be seen to reduce the gas entry pressure, suggesting that shearing in kaolinite has the opposite effect of self-sealing to gas.

Other general observations of gas flow along fractures included; a). The flow of fluids through clay filled fractures is non-uniform and occurs via localised preferential pathways; b). The pressure recorded within the slip-plane showed a negligible fracture pressure and did not vary much in all tests.

# 1 Introduction

Deep geological disposal is being widely considered as a viable option for the safe storage of high level radioactive waste. Safe management and disposal of radioactive waste in an isolated sub-surface setting is necessary to minimize the long term effects of radioactive waste on the biosphere. Deep geological disposal is currently the only available pragmatic solution for the storage and safe disposal of radioactive waste in Europe.

According to the current concepts, high level and long lived radioactive waste and spent fuel are intended to be stored/disposed of in a geological disposal facility (GDF) within a stable geological formation (host rock) at depth (typically ~50 – 800 m) beneath the ground surface. Hence, the radioactive waste is securely isolated and contained. At depth the rock mass may be a naturally fractured environment and the excavation of underground repositories is recognized to induce additional fractures (Bossart *et al.*, 2002; Rutqvist *et al.*, 2009). The zone of the host rock in the vicinity of the underground opening whose hydromechanical properties are modified as a consequence of excavation activities are referred to as excavation damaged zones (EDZ)<sup>1</sup>. The interplay of existing fractures and newly formed fractures in the EDZ will result in a complex array of fractures around the GDF. Depending on the in situ stress conditions, preferential pathways may form along faults, joints and the EDZ. Understanding the significance of such fractures and their connectivity in the transmission of repository fluids is of paramount importance in the long term storage of radioactive waste in the repository.

This study aimed to experimentally understand the dependence of different fracture orientations and stress states on the transmissivity of repository fluids through both natural and induced EDZ fractures. Furthermore, this study attempted to experimentally validate the critical stress theory proposed by Barton *et al.* (1995).

## 1.1 COMMON HOST ROCK TYPES CHOSEN FOR SUBSURFACE RADIOACTIVE WASTE DISPOSAL

The host rock formations considered for radioactive waste disposal can be broadly classified into crystalline rock, rock salt, indurated clay, and plastic clay formations. The rock salt, indurated clay, and plastic clay formations may self-heal and self-seal with time whereas crystalline formations may not do so. However, excavation of repositories in a crystalline formation is relatively stable when compared to those of rock salt, indurated clay, or plastic clay. Different host rocks behave in diverse ways during the various stages of repository development. During the excavation stage construction damage may lead to enhanced flow properties and result in stress redistribution. During the open-drift stage ventilation of the repository may modify the sealing properties of EDZ considerably. During the course of the early closure stage the effect of backfilling, resaturation and heating from waste canisters are likely to modify the properties of host rock and the EDZ. The degree of cooling, support degradation and self-sealing will influence the flow properties of an EDZ in the late closure stage. An extensive comparison of processes and issues associated with different EDZ host rock formations can be found in Tsang *et al.* (2005). A brief summary of different processes and factors affecting the EDZ in different host rock types is presented below.

---

<sup>1</sup> The term EDZ has been used interchangeably in scientific literature to denote either Excavation Disturbed Zone or the Excavation Damaged Zone. The definitions of these zones differ for specific host rock types such as crystalline rock, rock salt, indurated clay, and plastic clay. Detailed discussion about the terminology and characteristics of the Excavation Disturbed Zone or the Excavation Damaged Zone are presented in Tsang *et al.* (2005). In the present study we have adopted the definition of EDZ proposed by Bäckblom *et al.* (2004) where EDZ is defined as “the part of the rock mass closest to the underground opening that has suffered irreversible deformation where shearing of existing fractures as well as propagation or development of new fractures has occurred”.

### 1.1.1 Crystalline rock

In crystalline rocks the type of excavation method used can have a profound influence on the thickness of the EDZ and the resulting change in permeability. Excavation by drill-and-blast can lead to approximately 2 – 3 orders of magnitude increase in permeability with an EDZ thickness of between 10 and 150 cm; whereas the use of a tunnel boring machine will result in only one order of magnitude increase in permeability and the thickness of the damage zone is likely to be of the order of 1 cm. Stress redistribution following the excavation results in different parts of the drift experiencing either tension, compression, or shear. The extent of this stress anisotropy may extend up to 2 – 3 meters beyond the wall of the drift. In the open-drift stage, the EDZ may dehydrate and the air flow through the shafts may lead to oxidizing conditions and potential chemical and biological activities. In the early closure stage, the presence of faults within the EDZ control the swelling pressure imparted by the wetting and swelling of a bentonite buffer and bentonite/sand mixture backfill material. During the late closure stage of a repository, the inability of the fractures in crystalline rocks to self-seal may cause problems in containing radionuclides. However, over a period of thousands of years, clay minerals are expected to migrate into the fractures as a consequence of long-term heating and thermohydrologic effects and are expected to offer a suitable seal. Moreover, parameters such as *in situ* stress, density of fractures, orientation of fractures, rock strength, and the orientation of the drift with respect to the principal stress field needs to be taken into consideration. The Äspö Hard Rock Laboratory (Sweden) and the Underground Research Laboratory at Pinawa, Manitoba (Canada) are examples of research laboratories which have been studied to experimentally assess the viability of radioactive waste disposal in crystalline host rocks.

### 1.1.2 Rock salt

Dilatancy, healing and creep properties of rock salt help minimise the effect of excavation on the fluid flow properties in the EDZ during the excavation stage. Ventilation and salt dehydration may affect salt creep properties whilst the drift is open. In the early closure stage, the increase in humidity is likely to affect the EDZ properties. The heating from the canisters will induce high temperature gradients which will in turn affect the creep properties of the salt. During the late closure stage self-healing of the fractures and microcracks will occur by means of viscoplastic deformation and recrystallization in the presence of brine which will reduce the permeability of the rock salt. Irrespective of its excellent self-healing and sealing properties, excavation of repositories in rock salt may require the installation of a stiff liner during or immediately after excavation which may be problematic. The Asse Mines (Germany) and the Waste Isolation Pilot Plant (New Mexico, USA) are examples of research laboratories which have been studied to experimentally assess the viability of radioactive waste disposal in rock salt.

### 1.1.3 Indurated clay

In the case of indurated clays, the stress redistribution that results from excavation may give rise to strongly anisotropic, deviatoric compression and/or tensile stresses; these result in: a) tensile and shear fracturing along bedding planes, and b) vertical extensional or tensile fracturing in rock adjoining side walls. Similar to crystalline rocks, rock property parameters, *in situ* stress state, drift orientation relative to bedding plane direction, moisture content of rocks, and drift shape play a crucial role in controlling the properties of the EDZ. During the open-drift stage, rock creep may result in gallery wall convergence. Dehydration of the host rock due to ventilation may result in rock strengthening and contraction. Potential microbiological processes may also operate under these conditions. In the early closure stage of the repository, humidity increase during resaturation may weaken the rock, enhance creep, and induces closure of fractures and faults formed during excavation. However, the influence of transient and spatially varying temperature and water-saturation on rock properties is crucial in the early closure stage. In the late closure stage self-sealing of fractures may occur via precipitation of infill minerals. The Mont Terri Rock Laboratory (Switzerland) and the Laboratory Souterrain Meuse/Haute

Marne (Bure, France) are examples of research laboratories which have been studied to experimentally assess the viability of radioactive waste disposal in indurated clay rocks.

#### 1.1.4 Plastic clay

During the excavation of drifts in plastic clay formations, stress redistributions may result in contractant and dilatant processes with induced fracturing. During the open-drift stage of the repository, the drift wall moves towards the support offered by the liner. The hydromechanical properties of the clay are likely to be modified by drift ventilation and rock dehydration with ventilation leading to retardation in self-sealing capability of the rock. The effect of oxidation is usually limited to around 1 m into the rock. In the early closure stage, the effect of heating from the canister will result in a varying degree of saturation and thermal expansion/contraction and is likely to modify the rock properties. The creep rate of plastic clays will be boosted under increasing temperature conditions and open fractures are expected to heal. Piezometric studies in natural analogues have indicated that open fractures do not extend beyond a metre of the drift during simulated heating experiments. In the late closure stage, slow healing of fractures may take place during consolidation due to swelling and creep. Ensuing transport of radionuclides is likely to occur via diffusion mechanism. The Hades Underground Research Laboratory (Mol, Belgium) is an example of a research laboratory which has been studied to experimentally assess the viability of radioactive waste disposal in plastic clays.

### 1.2 STATE OF STRESS AND DISTRIBUTION OF FRACTURES AROUND THE EXCAVATION TUNNELS IN THE EDZ

The removal of rock mass during underground tunnel excavation significantly alters the local stress field (Figure 1). As a result of the redistribution of the *in-situ* stresses, the rock in the vicinity of the EDZ has to accommodate the stress borne earlier by the excavated rock mass. Tunnelling methodologies, such as drill & blasting or use of a tunnel boring machine, tends to damage the host rock which in combination with the inhomogeneous distribution of stress field results in the creation of complex fracture networks around the EDZ (Figure 2). Bossart *et al.* (2004) identified two distinct zones within the EDZ in Opalinus Clay of the Mont Terri Underground Research Laboratory (URL). The inner zone extends a metre from the tunnel wall made up of interconnected fracture network connected to the tunnel. The outer zone extends from the inner zone boundary to approximately 2 m from the tunnel wall and comprises non-connected unloading fractures (Figure 2). The fracture density decreases away from the tunnel wall with the inner zone containing many more fractures than the outer zone.

The hydromechanical and geochemical modification in the EDZ during excavation may lead to one or more orders of magnitude increase in permeability (Tsang *et al.*, 2005). However, the extent of this hydromechanical and geochemical modification will be determined by the nature of the host rock and the associated physicochemical conditions. Studies by Bossart *et al.* (2004) on the permeability distribution around a test tunnel at the Mont Terri URL on Opalinus Clay have shown zones of high permeability located within the first 10 – 20 cm within the inner zone of the EDZ with permeability values in the range of  $10^{-11}$  to  $10^{-13}$  m<sup>2</sup> (Figure 3). However, between 40 and 100 cm from the tunnel permeability values were up to two orders of magnitude lower than in the previous case with typical permeability values in the range of  $10^{-15}$  to  $10^{-16}$  m<sup>2</sup> (Figure 3) .

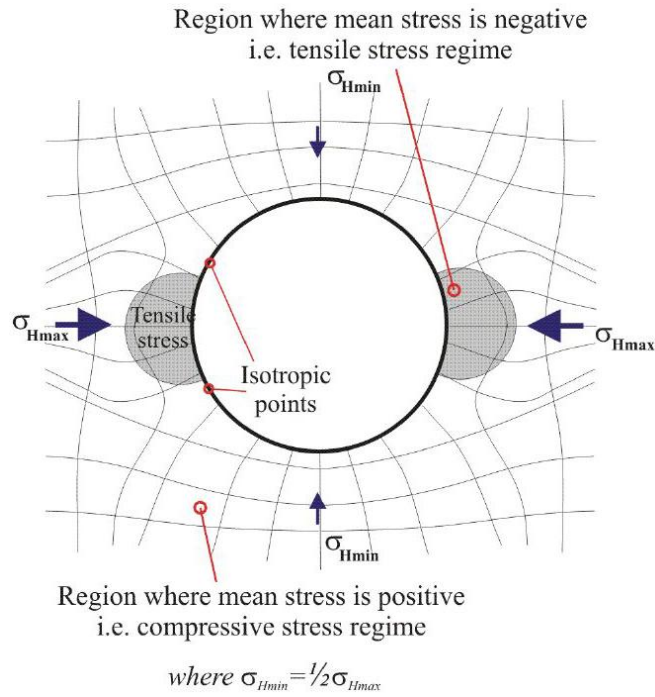


**Figure 1** - Stress trajectories around a non-hydrostatically loaded circular opening, such as a tunnel, demonstrating the prevailing stress inhomogeneity adjacent to the tunnel wall (from Cuss, 1999).

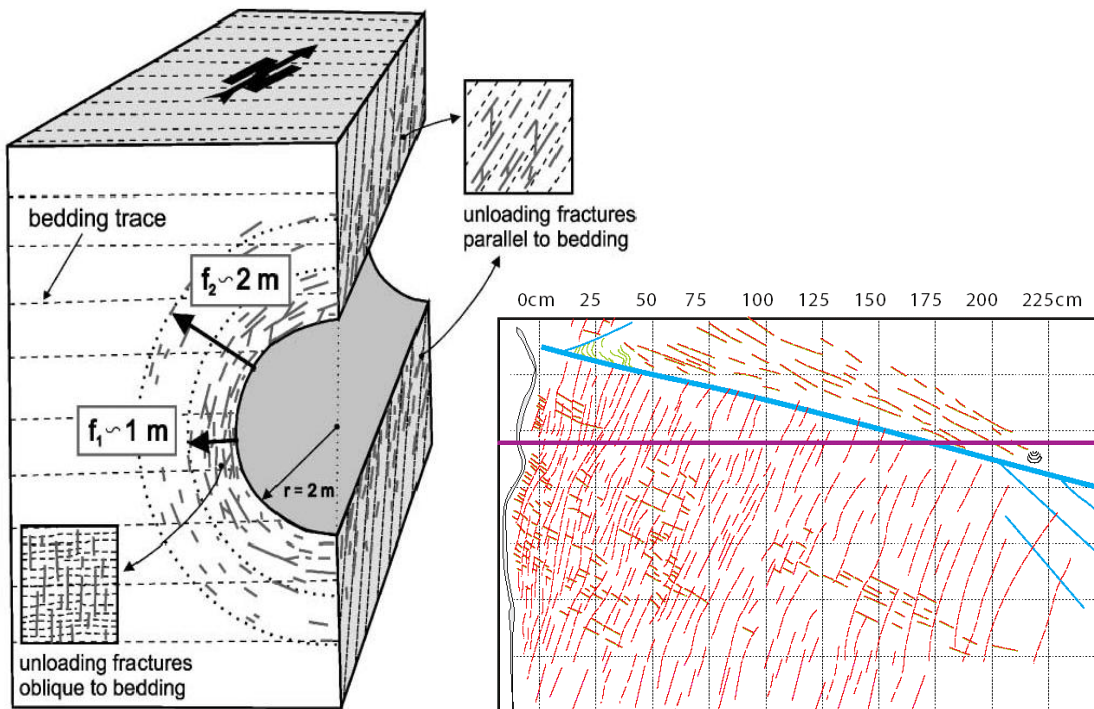


**Figure 2** - Complex network of fractures in the EDZ. The density of fractures decreases away from the tunnel opening (from Bossart *et al.*, 2002; Bossart *et al.*, 2004).

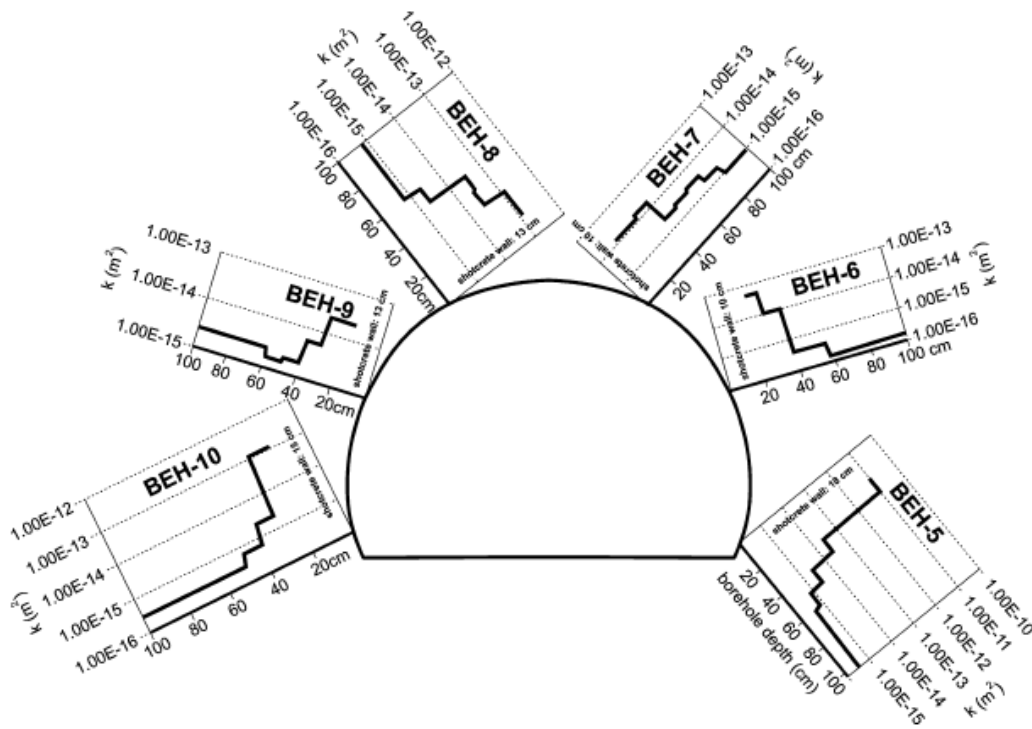


**Figure 3** - Distribution of permeability in a tunnel at Mont Terri URL. Zones within 10 – 20 cm of the tunnel exhibited high permeability ( $1 \times 10^{-14} \text{ m}^2$ ) (from Bossart *et al.*, 2004).

### 1.3 CRITICAL STRESS THEORY AND RELATED FLUID FLOW

The formation of fractures during tunnel excavation provides preferential pathways for fluids within the EDZ. The flow of repository fluids (water and/or gas) away from the repository along the fracture network will be determined by the fracture density, aperture of the fracture, extent of the fracturing, connectivity of the fractures, permeability through the fracture planes, and the orientation of the fractures (Barton *et al.*, 1997; Barton *et al.*, 1995; Finkbeiner *et al.*, 1997; Rogers, 2003). Previous studies have shown that only some fractures within a fractured system act as conduits for fluid movement whereas other fractures do not contribute towards fluid movement. Critical stress theory has been proposed to explain these differences in fracture conductivities.

It has been proposed that fractures and faults that are oriented parallel to  $\sigma_{Hmax}$  have the lowest normal stresses acting across them and therefore will undergo the least amount of closure and hence will be the most permeable (Heffer & Lean, 1993). Fractures and faults experiencing the least amount of stress will offer minimum resistance to flow and therefore will have relatively high permeability. Studies by Laubach *et al.* (2004) on a number of sedimentary basins in the western United States using core permeability datasets, stress measurements, and fluid flow data have shown that at a depth greater than three kilometres the open fractures do not parallel the  $\sigma_{Hmax}$  direction. Hence, *in situ* stress direction cannot be used as an indicator for predicting maximum permeability directions.

Barton *et al.* (1995) suggested that fractures whose state of stress is close to the failure criterion are likely to be more conductive because of the localised failure as a consequence of large shear component acting along the fracture. Such fractures were termed to be critically stressed. To apply the critical stress theory for fracture flow, the *in situ* stress field acting along all the faults and fractures are resolved into shear and normal stress components. When the magnitude and direction of the stress field has been constrained, the horizontal stress ( $\tau$ ) and normal stress ( $\sigma_n$ ) acting on a fracture surface can be given by (Jaeger *et al.*, 2007):

$$\tau = \beta_{11} \beta_{21} \sigma_1 + \beta_{12} \beta_{22} \sigma_2 + \beta_{13} \beta_{23} \sigma_3 \quad \text{and}$$

$$\sigma_n = \beta_{11}^2 \sigma_1 + \beta_{12}^2 \sigma_2 + \beta_{13}^2 \sigma_3$$

Where;  $\beta_{ij}$  = directional cosines between the fracture surface and the stress tensor;  $\sigma_1$ ,  $\sigma_2$ , and  $\sigma_3$  = magnitude of the maximum, intermediate, and minimum principal stresses respectively.

A three dimensional Mohr diagram (Figure 4) is commonly used to display the stress and orientation data. Since the magnitudes of the stresses increase with depth in a borehole all the data are normalised with respect to the vertical stress component to facilitate plotting of all data points within the same Mohr circle space. The Mohr-Coulomb failure criterion can be used to recognize whether a fracture or fault surface is expected to shear under the prevailing stress conditions (Figure 4). Assuming conditions of effective stress, the Coulomb failure criterion is given as:

$$\tau = \mu (\sigma_n - P_p)$$

Where;  $\mu$  = coefficient of friction;  $P_p$  = pore pressure.

Later studies by Byerlee (1978) proposed that up to normal stresses of 200 MPa, the horizontal stress required to cause frictional sliding can be given by the equation:

$$\tau = 0.85 \sigma_n$$

and for normal stresses above 200 MPa, the horizontal stresses required for sliding can be given by the equation:

$$\tau = 50 + 0.6 \sigma_n$$

The intrinsic shear strength or cohesion of rocks is assumed to be negligible under the crustal stress conditions and hence neglected. Critical stress theory proposes that fractures with their horizontal stress and normal stress data that fall above the Mohr-Coulomb failure criterion are in a critically stressed state and therefore are likely to exhibit enhanced permeability.

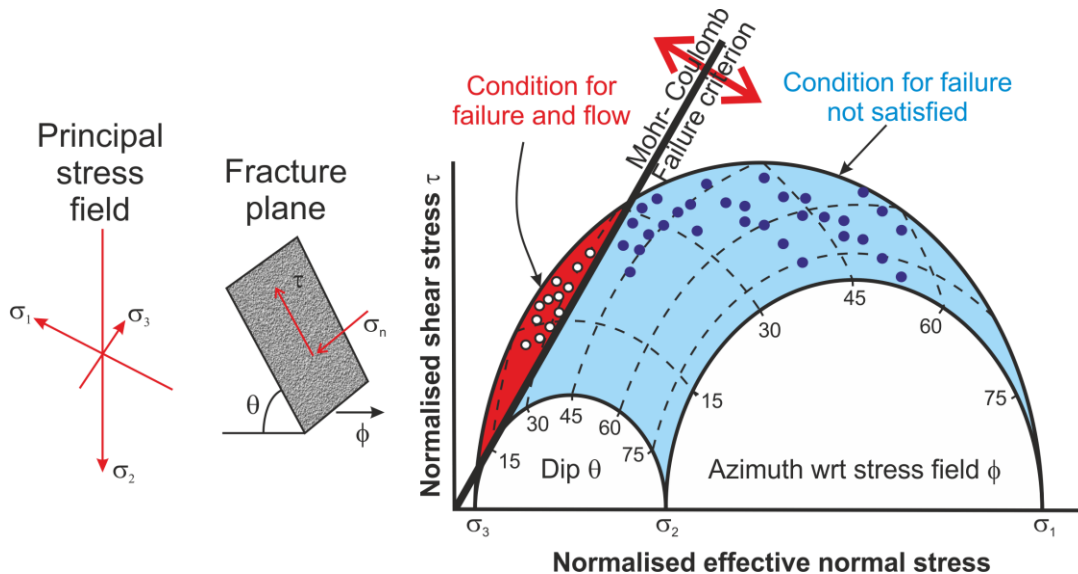


**Figure 4** - The three-dimensional Mohr diagram displaying the horizontal stress and normal stress on faults and fracture surface with respect to the *in situ* stress field. The points lying above the Mohr-Coulomb failure criterion are critically stressed and are likely to be conductive. Conversely, the points lying below the Mohr-Coulomb failure criterion have not reached the condition for failure and hence will be impermeable to fluid flow (from Rogers, 2003).

Based on field observations in the Sellafield area, Cumbria, UK, Rogers (2003) suggested that maximum flow is unlikely to occur along the  $\sigma_{Hmax}$  direction and is more likely to occur along a direction  $\pm 30$  degree to the  $\sigma_{Hmax}$  direction (Figure 4). However, detailed studies of the *in situ*

stress distribution at Sellafield confirmed that a majority of fractures lie below the Mohr-Coulomb failure criterion and are not critically stressed (Reeves, 2002; Figure 5). Experimental understanding of critical stress behaviour and variations in fracture orientation in assisting fluid (water and gas) flow through discontinuities become important in the light of these uncertainties in field observations.

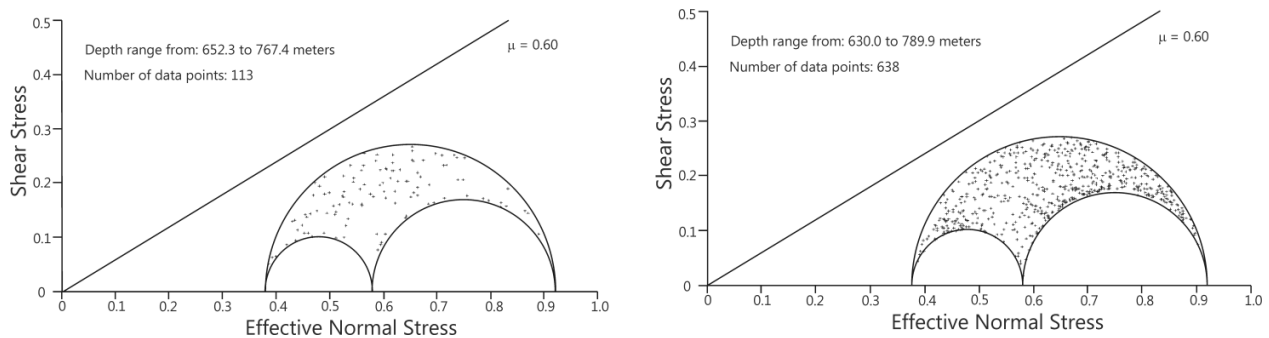


**Figure 5** - Detailed *in situ* stress data from the Sellafield area illustrating that none of the fractures are critically stressed at the present time. Flowing fractures are plotted on the left and the non-flowing fractures are plotted on the right.

Analysis of fracture permeability and *in situ* stress by Ito & Zoback (2000) for fractures in the depth range of 3 to 7 km in the KTB scientific drillhole have shown that the permeable faults and fracture were aligned close to the Mohr-Coulomb failure envelope for a coefficient of friction of 0.6. They concluded that critically stressed fractures in the crust are the most conductive to fluid flow and non-critically stressed fractures are least conductive.

Berge *et al.* (1999) modelled the geomechanical behaviour of the Topopah Springs tuff, Yucca Mountain, Nevada by applying the concept of critical stress theory. The zones of enhanced permeability were determined following the work of Barton *et al.* (1995; 1997). Their Thermo-hydro-mechanical (THM) modelling showed a factor of two increase in permeability for vertical fractures and up to a factor of four increase in permeability for fractures with slip movement.

Analysis of fracture and fluid flow datasets from the geothermal reservoir at Dixie Valley by Barton *et al.* (1998) indicated that the majority of fractures with high permeability were critically stressed for frictional failure. However, many non-flowing but critically stressed fractures were also encountered in the same area. They concluded that in the Dixie Valley high fault zone high permeability was observed only when the individual fractures along with the Stillwater fault zone within the area were optimally oriented and critically stressed for frictional failure.

A review of the role of hydro-mechanical (HM) coupling in fractured rock engineering by Rutqvist & Stephansson (2003) concluded that stress-dependant permeability plays a major role in rocks containing flat microcracks and macrofractures. They suggested that the fracture permeability under varying stress conditions depends on hydraulic properties such as fracture permeability and connectivity of the fracture network, and also on mechanical parameters such as fracture normal stiffness and fracture shear strength. Additionally, they ascribed the enhancement of permeability during shear slip on a critically stressed fracture to mechanisms such as brecciation, surface roughness, and breakdown of seals as proposed by Barton *et al.* (1995).

Talbot & Sirat (2001) studied the hydraulic conductivity in highly fractured granitoid bedrock with large range of orientations and complicated deformation histories exposed in the Äspö Hard Rock Laboratory in Sweden. Out of ~ 11,000 documented fractures in the locality, only 8 % of those fractures appeared to be conductive during initial excavation. The majority of the wet fractures were either sub-horizontal, which were prone to thrusting, or sub-vertical with an underlying stress regime susceptible to wrench faulting. They concluded that faults favourably oriented for slip or dilation in the ambient stress field were most conductive to fluid flow. Similar observations were reported in the case of groundwater flow in Monterey Formation,

Santa Maria Basin, California by Finkbeiner *et al.* (1997) and in the vicinity of Yucca mountain, Nevada by Ferrill *et al.* (1999).

Evans (2005) evaluated the fluid flow properties of critically stressed fractures in a 3.5 km deep borehole in granite at the Soultz-sous-Forets Hot Dry Rock (HDR) project site in the Rhinegraben area in France. He observed that all 18 naturally flowing fractures were critically stressed. Nonetheless, a significant number (~ 500) of fractures were non-flowing irrespective of fulfilling the critical stress criterion. He concluded that being critical stressed is a necessary condition for fracture flow but not a sufficient criteria for identifying flowing fractures.

Rutqvist *et al.* (2009) presented numerical modelling of excavation-induced damage, permeability changes and fluid pressure responses during the excavation of a test tunnel in Lac du Bonnet granite as part of the tunnel sealing experiment (TSX) at the URL, Canada. They observed that the permeability changes during excavation are related to the combined effects of disturbance induced by stress redistribution around the tunnel and by the drill-and-blast-operation. The decrease in mean effective stress at the side of the tunnel and the high horizontal stress and strain at the top of the tunnel resulted in permeability increase. The increase in permeability at the top of the tunnel was ascribed to the formation of fractures as a consequence of a series of microseismic events during excavation.

An investigation into the stress controlled fluid flow in fractures within the crystalline basement of Fennoscandian shield in the Olkiluoto Island (Finland) by Matilla & Tammisto (2012) showed that the critical stress theory could not predict which of the fractures were conducting or not. The study involved the analysis of fluid flow properties of 38,703 fractures. They observed that between a depth range of 0 to 300 metres the majority of the conductive fractures were critically stressed. However, at depths of 300 to 800 metres almost all conductive fractures lay well below the critical stress criterion. They concluded that the transmissivity of fluids along fractures is determined by the normal traction acting across the fractures and suggested the integrated use of contemporary stress state in addition to slip & dilation tendency analysis of the fractures to predict fluid flow.

The concept of critical stress has been widely applied in predicting and modelling the fluid flow through fractures under *in situ* stress conditions under many geological settings. The relationship between critically stressed fractures and fluid flow from field studies has been inconclusive. Moreover, the occurrence of flowing fractures in non-critically stressed rocks, and conversely, the presence of non-flowing fractures in critically stressed rocks call for an experimental investigation into the conductivity of critically stressed fractures. In order to experimentally validate the critical stress theory under controlled hydromechanical conditions, a series of experiments were planned and performed using the bespoke Angled Shear Rig at the Transport Properties Research Laboratory (TPRL) of the British Geological Survey (BGS).

## 2 Experimental apparatus and methodology

A variety of different experimental geometries have been employed in the laboratory simulation of shear deformation. Different methods have distinct advantages and disadvantages. The most commonly used methods in laboratory fracture studies are (after Mogi, 2007):

- A) Conventional direct shear test;
- B) Conventional double-shear test;
- C) Biaxial compression shear test;
- D) Conventional triaxial compression test.

Schematic representations of the different experimental setups are shown in Figure 6. The conventional direct shear test can be used to study large samples with large shear planes. The major disadvantage with this kind of experimental setup is that large contact area between the top and bottom blocks can result in non-uniform distribution of normal stresses along the experimental slip plane. Moreover, larger contact surface area implies that the maximum stresses that can be applied to the slip plane are relatively low. In the conventional double-shear test, two sliding surfaces are present; this setup also results in inhomogeneous distribution of stresses along the slip planes. In a biaxial compression shear test, uniform normal stresses could be applied but constant normal stresses cannot be maintained for stick-slip and the stresses that can be achieved are quite low. Conventional triaxial compression tests are employed in studies where higher stresses are required. The contact area of the slip plane is small and the contact area changes with shearing leading to variation in normal stress values. Apart from these fundamental shear apparatuses, rotary shear (ring-shear) apparatus are also employed where large displacements of the gouge can be achieved by rotary movement of the blocks.

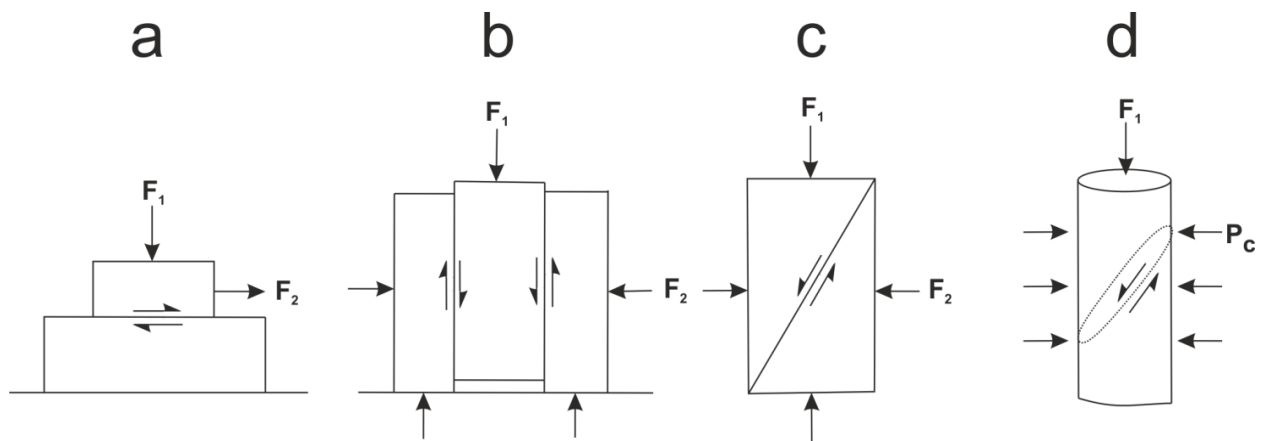


**Figure 6** - Common friction test arrangements. a) Conventional shear test. b) Conventional double shear test. c) Biaxial test. d) Conventional triaxial test (from Mogi, 2007).

In order to achieve the objective of the present study, conventional direct shear was adopted. A bespoke Angled Shear Rig (ASR) was built at the Transport Properties Research Laboratory (TPRL), British Geological Survey (BGS), and was employed to validate the applicability of critical stress theory in repository scenarios.

### 2.1 ANGLED SHEAR RIG (ASR)

The ASR (Figure 7) used in the present study is a custom-modified form of the standard soil-shear apparatus (conventional direct shear apparatus) as outlined by Gutierrez *et al.* (2000). The ASR facilitated independent control of the slip plane orientation, vertical and horizontal stresses,

pore pressure, and horizontal displacement (shear) rate. This assisted in experimentally understanding the relationship of fracture conductivity and the combined effect of variations in fracture orientation and stress conditions. The core components of the ASR are listed below:

1. Rigid frame that has been designed to withstand the applied vertical and horizontal stresses.
2. Vertical loading system comprised of a rigid loading beam, a rigid loading frame, two load cells, and a hydraulic jack controlled by a servo controlled ISCO syringe pump.
3. Horizontal force actuator connected in parallel with a load cell. The force actuator was capable of a linear horizontal movement as slow as  $14 \mu\text{m}$  a day along a low friction bearing.
4. Pore pressure system comprised of an ISCO syringe pump connected to a water/gas interface vessel that could be used to inject either water or gas at a constant rate or at a constant pressure. A schematic of the fluid injection system is shown in Figure 9.
5. Data acquisition system connected to the pressure transducers, load cells, thermocouples by means of acquisition software written in National Instruments LabVIEW™ environment. This software also allowed remote monitoring and control of all experimental parameters.
6. The experimental slip plane assembly consisting of precision machined 316 stainless steel top and bottom blocks with dips of  $0^\circ$ ,  $15^\circ$ ,  $30^\circ$ , and  $45^\circ$ . The top block was connected to the vertical loading mechanism by means of a swivel mechanism which was engaged to the shoulders on either side of the top block (Figure 8a).

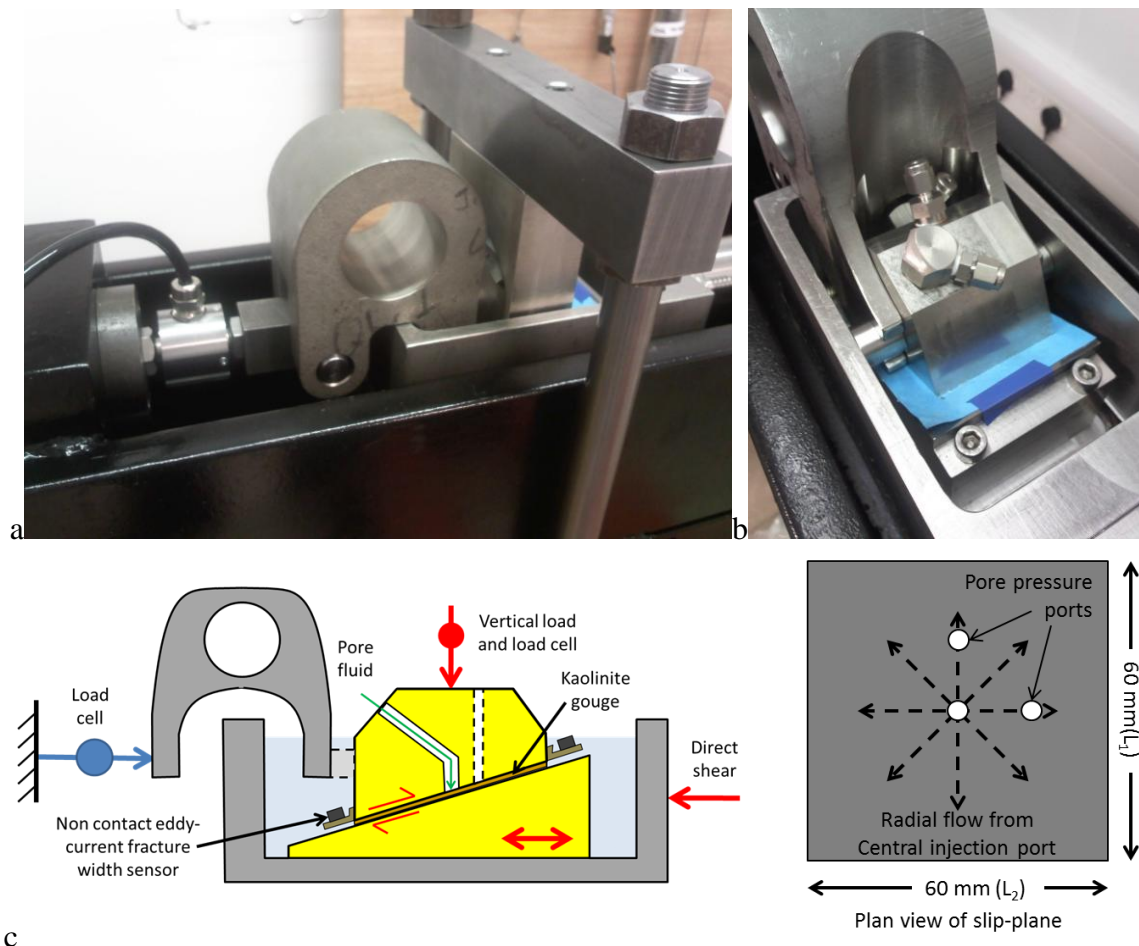


**Figure 7** - Angled shear rig (ASR). a) Photograph of the vertical and horizontal loading system. b) Photograph of the angled shear block and the upper platen arrangement. c) Schematic of the ASR.

A fully saturated kaolinite clay sample (80 % gravimetric water content) was placed between two stainless-steel blocks forming a  $60 \times 60$  mm slip plane surface and was deformed by applying a vertical load and/or horizontal displacement which resulted in a gouge thickness of

approximately  $70 \pm 10 \mu\text{m}$ . The kaolinite paste was selected for two reasons; firstly it prevented cold-welding of the steel blocks, and secondly kaolinite is a low swelling clay which is commonly found as fracture fill.

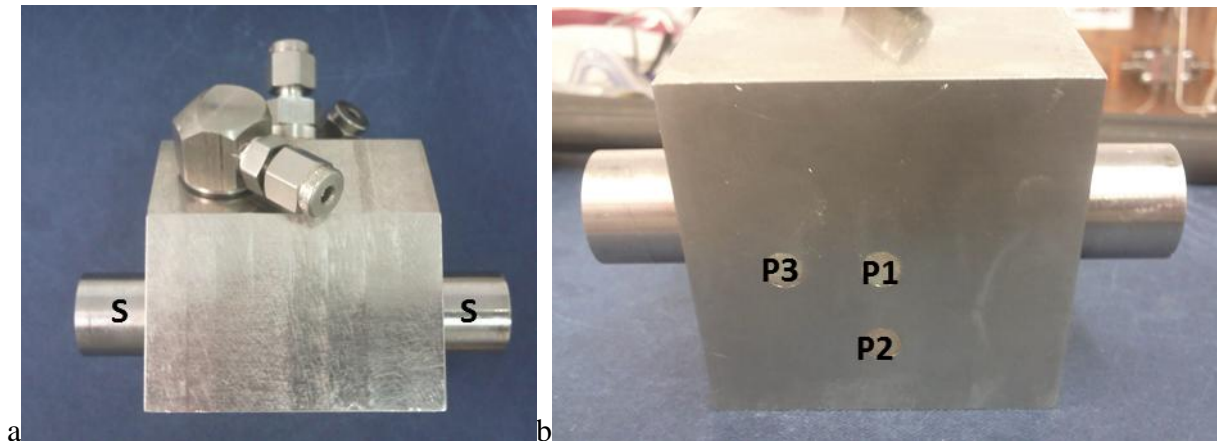


**Figure 8** - Components of the top block. a) Frontal-view of top block. “S” depicts the shoulders that are engaged to the loading mechanism to impart uniform normal stress along the slip plane. b) The bottom-view of the top block showing the central pore fluid injection port (P1) and the two orthogonally spaced pore pressure ports (P2 & P3) to monitor the pore pressure within the slip plane during the course of the experiment.

### Fluid injection circuit

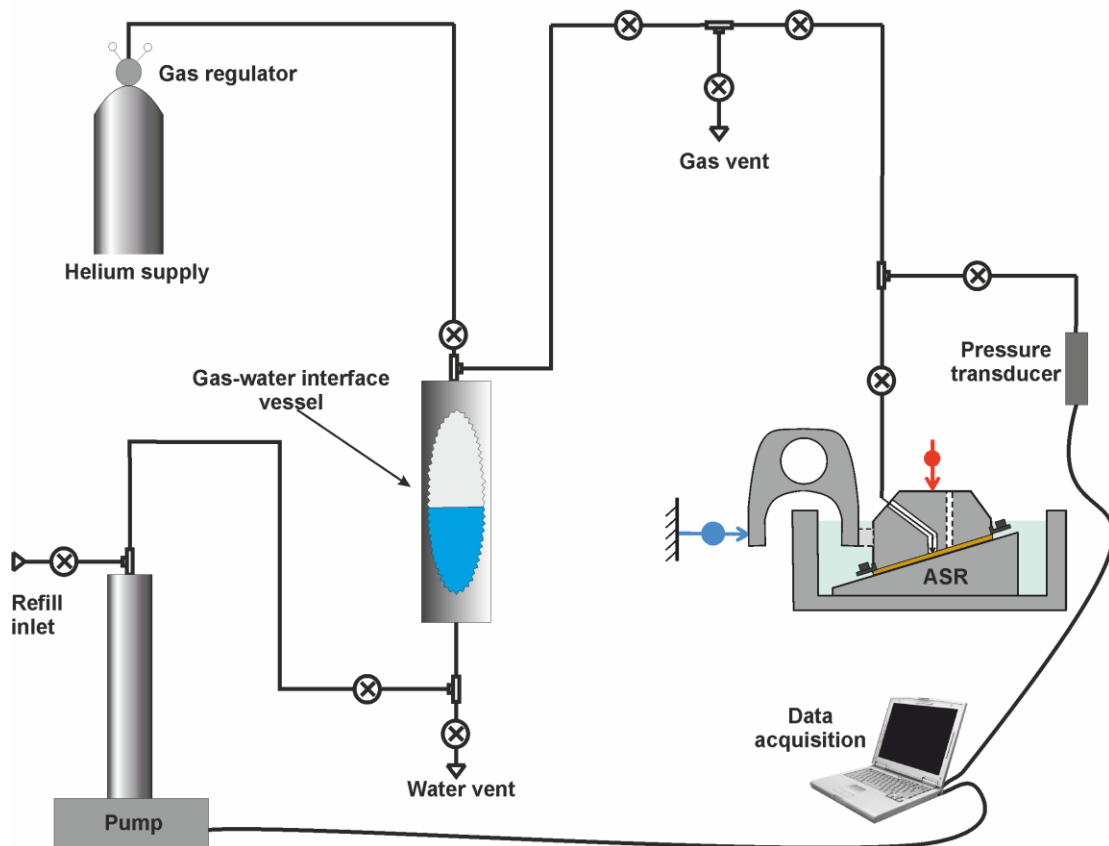


**Figure 9** - Fluid injection circuit displaying the servo-controlled ISCO™ injection pump and the gas-water interface vessel used to inject helium into the idealised slip plane.

## 2.2 SAMPLE PREPARATION AND EXPERIMENT ASSEMBLY

The powdered kaolinite (Echantillon Sample – Supreme Powder) used in the present study was acquired from ECC International (presently known as Imerys Minerals Ltd.). Kaolinite paste was prepared by adding 16 g of de-ionised water to 20 g of kaolinite powder. The water and kaolinite powder were then meticulously stirred for about five minutes giving a kaolinite paste with a gravimetric water content of  $80 \pm 1$  %. The paste was smeared uniformly onto the surface of the top block, which was then carefully lowered onto the bottom block thus forming a kaolinite paste gouge. The initial thickness of the gouge was measured to be 1 – 2 mm. However, with loading the gouge thickness decreased to approximately  $70 \pm 10$  microns.

The experiments were conducted after carefully setting the load frame of the vertical loading system in order to ensure even loading across the width of the slip plane. The pore fluid was injected into the centre of the slip plane by means of an injection port (P1) in the top block and the distribution of fluid pressures within the slip plane was monitored using two orthogonally spaced ports (P2 and P3) positioned 1cm away from P1 (Figure 8b). Whilst setting the experiment the pipework and pressure transducers were filled with de-ionised water to ensure air volumes in P2 and P3 were minimised.

## 2.3 EXPERIMENTAL PROCEDURE

A series of experiments (Table 1) were performed to study the fluid flow properties through experimental slip planes under different stress conditions. Experiments were performed on slip plane orientations of  $0^\circ$ ,  $15^\circ$ ,  $30^\circ$ , and  $45^\circ$  relative to the maximum horizontal stress direction. All the experiments can be broadly categorised into two types:

1. Loading-Unloading (LU) Experiments
2. Gas Injection (GI) Experiments

In a few selected experiments, the effect of shear on fluid flow was investigated in both LU and GI experiments. In such cases, the bottom block attached to a servo controlled shear mechanism was allowed to move at a fixed rate to induce horizontal movement whereas the top block was locked into stationary position.

### 2.3.1 Loading-Unloading (LU) Experiments

In loading-unloading (LU) experiments the vertical stress acting across the slip plane was increased and decreased in stages and the corresponding response of flow-rate was monitored. As previously stated, vertical load was applied to the slip plane by means of a ISCO syringe pump connected to a hydraulic jack. The pressure of the syringe pump was increased in steps of 1 MPa from 1 MPa up to 14 MPa and subsequently decreased in steps to 1 MPa. As shown in Table 2, a 1 MPa increase in pump pressure resulted in a force of 73.95 kg, or a stress of 172 kPa. The vertical load was controlled within  $\pm 1$  kg.f throughout each stage. In the case of LU experiments with water, the injection pressure was maintained at 1 MPa. In the case of LU experiments with helium a gas pressure in excess of the gas breakthrough pressure was used. Gas breakthrough was achieved by systematically increasing the gas injection pressure in steps of 50 kPa until significant gas flow was detected; gas pressure was then maintained constant and the normal load was varied accordingly to test the effect of normal load variation on gas flow. The list of LU experiments using water and gas injection fluids are given in Table 1.

	Experiment	Start date	Sample Material	Type of test	Pore fluid	Slip-plane orientation	Gas Injection test number
1	ASR_Cal01_30	26-Jan-10	None	Calibration	He		
2	ASR_Cal02_30			Calibration			
3	ASR_Cal03_30			Calibration			
4	ASR_Cal04_30			Calibration			
5	ASR_Tau01_30wLU	09-Nov-10	Kaolinite	LU	H <sub>2</sub> O		
6	ASR_Tau02_30wLUS	10-Dec-10	Kaolinite	LU + shear			
7	ASR_Cal05_30xLU	26-Apr-11	Dry kaolin	LU	None	30°	A
8	ASR_Cal06_30xLU	04-May-11	Kaolinite				
9	ASR_Cal07_30xLU	09-May-11	None	Leak test			
10	ASR_Cal08_30xLU	12-May-11	Kaolinite				
11	ASR_Cal09_30xLU	12-May-11	Dry	LU			
12	ASR_Cal10_30xLU	17-May-11					
13	ASR_Cal11_30xLU	19-May-11					
14	ASR_Cal12_30xLU	20-May-11	Kaolinite	Pore fluid permeability test	H <sub>2</sub> O		
15	ASR_Tau03_30wLU	24-May-11	Kaolinite (100%)				
16	ASR_Tau04_30wLU	25-May-11		Flow test			
17	ASR_Tau05_30wLU	27-May-11					
18	ASR_Tau06_30gGI	24-Jun-11		Kaolinite (80% saturated)	Helium gas permeability (GI)	Helium	1
19	ASR_Tau07_30gLU	22-Jul-11					
20	ASR_Tau08_30gLU	22-Aug-11					
21	ASR_Tau09_30gGI	27-Sep-11					
22	ASR_Tau10_30gGI	10-Oct-11					
23	ASR_Tau11_30gGI	11-Oct-11					
24	ASR_Tau12_30gGI	09-Nov-11					
25	ASR_Tau13_30gGI	18-Nov-11					
26	ASR_Cal13_30xLU	08-Dec-11					
27	ASR_Tau14_30gLU	12-Dec-11					
28	ASR_Tau15_00gGI	14-Feb-12	0°	5			
29	ASR_Tau16_00gGI	23-Feb-12		6			
30	ASR_Tau17_00gGI	05-Mar-12	15°	7			
31	ASR_Tau18_15gGI	22-Mar-12		8			
32	ASR_Tau19_15gGI	03-Apr-12	0°	9			
33	ASR_Tau20_15gGI	18-Apr-12		10			
34	ASR_Tau21_00gGI	01-May-12	45°	11			
35	ASR_Tau22_00gGI	14-May-12		12			
36	ASR_Tau23_00gGI	28-May-12	0°	13			
37	ASR_Tau24_00gGI	06-Jun-12		14			
38	ASR_Tau25_45gGI	19-Jun-12	45°	15			
39	ASR_Tau26_45gGI	03-Jul-12		16			
40	ASR_Tau27_45gGI	13-Jul-12	0°	17			
41	ASR_Tau28_00gGIS	25-Jul-12		18			
42	ASR_Tau29_00gGIS	06-Aug-12	30°	19			
43	ASR_Cal14_30x	20-Aug-12		20			
44	ASR_Tau30_30gGIS	29-Aug-12	45°	21			
45	ASR_Tau31_45gGIS	10-Sep-12		22			
46	ASR_Tau32_15gGIS	25-Sep-12	15°				

**Table 1** – List of all experiments undertaken as part of the current study.

	ASR_Tau05_30wLU		ASR_Tau07_30gLU	
	ISCO Pump Pressure (MPa)	Load cell (kg.f)	ISCO Pump Pressure (MPa)	Load cell (kg.f)
LOADING	1	73.95	-	-
	2	151.40	2	149.18
	3	229.19	3	227.42
	4	304.00	4	302.69
	5	380.46	5	378.97
	6	458.59	6	458.74
	7	538.37	7	538.33
	8	615.83	8	617.43
	9	700.60	9	700.53
	10	781.22	10	779.96
	11	863.66	11	859.56
	12	944.27	12	940.16
	13	1022.89	13	1021.09
	14	1106.15	14	1103.36
UNLOADING	13	1044.49	13	1042.03
	12	977.68	12	974.56
	11	904.55	11	903.93
	10	826.42	10	830.81
	9	741.49	9	751.04
	8	663.86	8	666.79
	7	579.92	7	596.83
	6	498.64	6	499.29
	5	417.68	5	417.86
	4	336.74	4	336.77
	3	255.45	3	254.01
	2	164.37	2	162.62
	1	79.42	-	-

**Table 2** - Variation in load cell reading during variation in ISCO syringe pump pressure.

### 2.3.2 Gas Injection (GI) Experiments

All the GI experiments reported here (Table 1) were performed at a pressure of 10 MPa in the controlling ISCO syringe pump, giving a load of 782 kg.f (2 MPa vertical load). The gas injection rate was controlled using a second ISCO pump as shown in Figure 9. All the GI experiments were started at a gas pressure of 4 MPa. It should be noted that the starting volume of gas within the water/gas interface vessel was  $200 \pm 0.2$  cc in all GI experiments. Gas injection was performed by injecting water into the gas/water interface vessel at a flow rate of  $700 \mu\text{l.h}^{-1}$  using the ISCO pump. This increased the gas pressure within the interface vessel at a steady rate. Boyle's law allowed gas pressure to be predicted knowing the initial volume and change in volume. Gas entry could be determined by carefully comparing the recorded pressure with the predicted pressure. When the two values begin to differ it showed that gas was moving into the clay gouge. The pressure at which gas entry occurred provided valuable information about the dependence of gas flow on the orientation of the slip plane along with the evolution of gas pressure after gas breakthrough and the evolution of fluid.

## 2.4 CALCULATION OF FRACTURE TRANSMISSIVITY

Assuming radial flow of injection fluids (gas or water) from the central injection port (Figure 10), transmissivity of fluid was determined from flow rate using the equation:

$$Q = \frac{2\pi TH}{\ln(r_2/r_1)} \quad \text{Equation 1}$$

where,  $Q$  = flow rate of the fluid ( $\text{m}^3 \cdot \text{s}^{-1}$ );  $T$  = transmissivity ( $\text{m}^2 \cdot \text{s}^{-1}$ );  $H$  = pressure head (m);  $r_1$  = radius of the injection tube (m);  $r_2 = \sqrt{(L_1 L_2)/\pi}$  = equivalent outer radius of the slip plane surface (m).

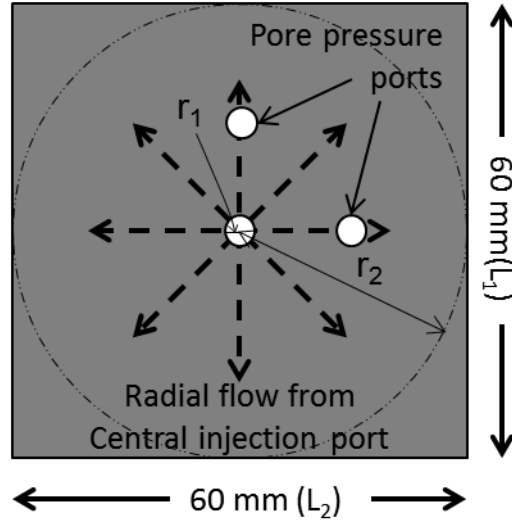


**Figure 10** - Plan-view of the slip plane with fluid injection port in the centre and two orthogonally located pore pressure sensor ports. The parameters  $L_1$ ,  $L_2$ ,  $r_1$ , and  $r_2$  are also depicted.

Equation 1 can be rewritten as:

$$T = \frac{Q \ln(r_2/r_1)}{2\pi H} \quad \text{Equation 2}$$

since,

$$H = \frac{P_i}{\rho_f g} \quad \text{Equation 3}$$

where;  $P_i$  = fluid injection pressure (Pa);  $\rho_f$  = density of the fluid ( $\text{kg} \cdot \text{m}^{-3}$ );  $g$  = acceleration due to gravity ( $\text{m} \cdot \text{s}^{-2}$ ).

Substituting  $H$  in Equation 2 with Equation 3, transmissivity can be determined from the following:

$$T = \frac{Q \rho_f g \ln(r_2/r_1)}{2\pi P_i} \quad \text{Equation 4}$$

Hydraulic conductivity can be determined from  $T$  by the relation:

$$K = \frac{T}{e} = \frac{Q \rho_f g \ln(r_2/r_1)}{2\pi e P_i} \quad \text{Equation 5}$$

Where;  $K$  = hydraulic conductivity ( $\text{m} \cdot \text{s}^{-1}$ );  $e$  = conducting aperture of the slip plane (m)

Permeability can then be determined by the relation:

$$k = \frac{K\mu_f}{\rho_f g} = \frac{Q\mu_f \ln(r_2/r_1)}{2\pi e H \rho_f g} = \frac{Q\mu_f \ln(r_2/r_1)}{2\pi e P_i} \quad \text{Equation 6}$$

Where;  $k$  = permeability ( $\text{m}^2$ );  $\mu_f$  = dynamic viscosity of the fluid ( $\text{kg}\cdot\text{s}^{-1}\cdot\text{m}^{-1}$ ).

## 2.5 NOTE ON STRESS CONVENTION

Stress is described in this report with reference to the experimental apparatus; i.e. stress is horizontal (parallel with movement direction of the apparatus) and vertical. Stresses have not been converted to normal and shear directions parallel with and perpendicular to the fracture orientation. This approach has been adopted as the boundary condition of vertical stress is constant in different experiments with fractures at varying angles. Therefore variations observed in flow are in part due to differences in normal and horizontal stress at different fracture orientation, but illustrate the differences that would be seen in a similar location where multiple fracture directions are observed.

## 3 Observations and results

### 3.1 FRACTURE TRANSMISSIVITY EVOLUTION DURING VARIATIONS IN VERTICAL LOAD

The effect of loading and unloading on fracture transmissivity was studied by sequentially loading and unloading an idealised kaolinite gouge filled slip plane (fracture plane) oriented at an angle of  $60^\circ$  to the vertical stress direction by means of a bespoke shear apparatus (Figure 7). Both water (de-ionised) and gas (helium) were used as permeants (pore fluids) in order to understand the differences in behaviour of water and gas transmissivity.

#### 3.1.1 Hydraulic flow during loading and unloading through an idealised slip plane

Two experiments (ASR\_Tau01\_30wLU and ASR\_Tau05\_30wLU) were conducted to understand the effect of loading and unloading on hydraulic fracture transmissivity. Test ASR\_Tau01\_30wLU was a short duration experiment where vertical load was varied a couple of times a day whereas in test ASR\_Tau05\_30wLU the vertical load was varied once every day.

##### 3.1.1.1 RESULTS

Test ASR\_Tau01\_30wLU comprised of a quick loading-unloading test devised to assess the experimental apparatus and to understand how the hydraulic flow along the slip plane was affected during variations in vertical load (Figure 11). The kaolinite gouge filled slip plane was loaded in stages of 0.2 MPa from 0 to 2.6 MPa and unloaded from 2.6 to 0 MPa in similar 0.2 MPa steps (Figure 11b). The loading-unloading stages and their respective durations are listed in Table 3. The temperature fluctuation during the entire duration of the experiment is shown in Figure 11a. An abrupt drop in temperature from  $21.4^\circ\text{C}$  to  $20.5^\circ\text{C}$  was observed around Day 9. The variation in flow rate at an injection pressure of 1 MPa in response to variations in vertical load was analysed. Flow rate decreased from  $87\ \mu\text{l.h}^{-1}$  at 0.2MPa to  $5\ \mu\text{l.h}^{-1}$  at 2.6MPa (Figure 11c&d). During unloading a partial recovery of flow rate to  $22\ \mu\text{l.h}^{-1}$  was observed. An abrupt increase in flow from  $10\ \mu\text{l.h}^{-1}$  to  $30\ \mu\text{l.h}^{-1}$  was recorded at Day 9. Similarly, transmissivity decreased from  $9.3 \times 10^{-14}\ \text{m}^2.\text{s}^{-1}$  to  $7 \times 10^{-15}\ \text{m}^2.\text{s}^{-1}$  during loading. Unloading of the slip plane surface from 2.6 to 0 MPa resulted in an increase in transmissivity from  $7 \times 10^{-15}\ \text{m}^2.\text{s}^{-1}$  to  $2.3 \times 10^{-14}\ \text{m}^2.\text{s}^{-1}$  (Figure 11f). Horizontal stress increased linearly with each vertical load increase during loading. However, during unloading considerable hysteresis was observed in horizontal stress (Figure 11e). The pore pressures within the slip plane remained low (23 kPa and 15 kPa) and unchanged irrespective of the high injection pressures of 1 MPa applied approximately 1 cm away from the slip plane pressure sensors (Figure 11g).

In order to understand the effect of loading and unloading on hydraulic flow in more detail, a longer duration repeat experiment ASR\_Tau05\_30wLU was performed (Table 4). Vertical stress was sequentially increased in stages of 0.2 MPa per day to a maximum vertical stress of 2.6 MPa (Figure 12). The pore fluid injection pressure was maintained at a constant value of 1 MPa. Although no horizontal stress was applied, the increase in horizontal stress as a consequence of vertical stress increase was logged throughout the duration of the experiment (Figure 12b). During the unloading stage, the vertical stress was decreased in steps of 0.2 MPa from 2.6 MPa to 0.2 MPa.

	Stage	Vertical stress (MPa)	Time (days)
LOADING	1	0.2	0.0
	2	0.4	0.8
	3	0.6	1.3
	4	0.8	1.8
	5	1.0	2.3
	6	1.3	2.8
	7	1.5	3.4
	8	1.7	3.8
	9	1.9	4.3
	10	2.1	4.8
	11	2.3	5.4
	12	2.6	5.8
	13	2.8	6.2
	14	3.0	6.8
UNLOADING	15	2.6	7.8
	16	2.2	8.3
	17	1.8	8.8
	18	1.3	9.8
	19	0.9	10.3
	20	0.6	10.8
	21	0.4	11.5
	22	0.3	12.0
	23	0.2	12.8
	24	0.1	13.2

**Table 3** - The loading and unloading stages in test ASR\_Tau01\_30wLU.

Temperature remained uniform at  $20.5 \pm 0.1$  °C throughout the entire duration of the experiment, with a few fluctuations of 0.2 °C at Day 17, 18, and 21 (Figure 12a). During loading (stages 1 to 14), a linear increase of horizontal stress was observed with increase in vertical stress whereas during unloading (stages 15 to 27), the horizontal stress showed considerable hysteresis (Figure 12b,e). The flow rate decreased an order of magnitude from  $50 \mu\text{l.h}^{-1}$  to  $5 \mu\text{l.h}^{-1}$  during loading from 0 to 2.6 MPa. During unloading from 2.6 to 0.2 MPa, flow rate doubled from  $5 \mu\text{l.h}^{-1}$  to  $10 \mu\text{l.h}^{-1}$ . Also from 2.6 MPa to 1.0 MPa vertical stress, the flow rate remained more or less constant at  $5 \mu\text{l.h}^{-1}$  irrespective of the significant reduction in vertical load (Figure 12c,d). Pore pressure within the slip plane recorded much lower pressures (50 – 80 kPa and 5 – 25 kPa) than the injection pressure (1 MPa) (Figure 12f). Vertical stress to normal stress ratio decreased from 1.6 to a minimum value of 0.7 during loading and increased to 1.9 during unloading (Figure 12g). Moreover, a close correlation between the horizontal stress to vertical stress ratio and flow rate was observed in the unloading phase particularly when the initial horizontal stress to vertical stress ratio of 1.5 was exceeded and the flow rate doubled from  $5 \mu\text{l.h}^{-1}$  to  $10 \mu\text{l.h}^{-1}$ . During loading, transmissivity decreased from  $5 \times 10^{-14} \text{ m}^2\text{.s}^{-1}$  to  $0.6 \times 10^{-14} \text{ m}^2\text{.s}^{-1}$ . However, during unloading transmissivity recovered to only  $1.1 \times 10^{-14} \text{ m}^2\text{.s}^{-1}$  (Figure 12h). The thickness of the kaolinite gouge decreased with loading from 54  $\mu\text{m}$  at a vertical stress of 0.2 MPa to 42  $\mu\text{m}$  at a vertical stress of 2.6 MPa. During unloading slip plane width continued to decrease further to 40  $\mu\text{m}$  before finally recovering to 43  $\mu\text{m}$  after full unloading.

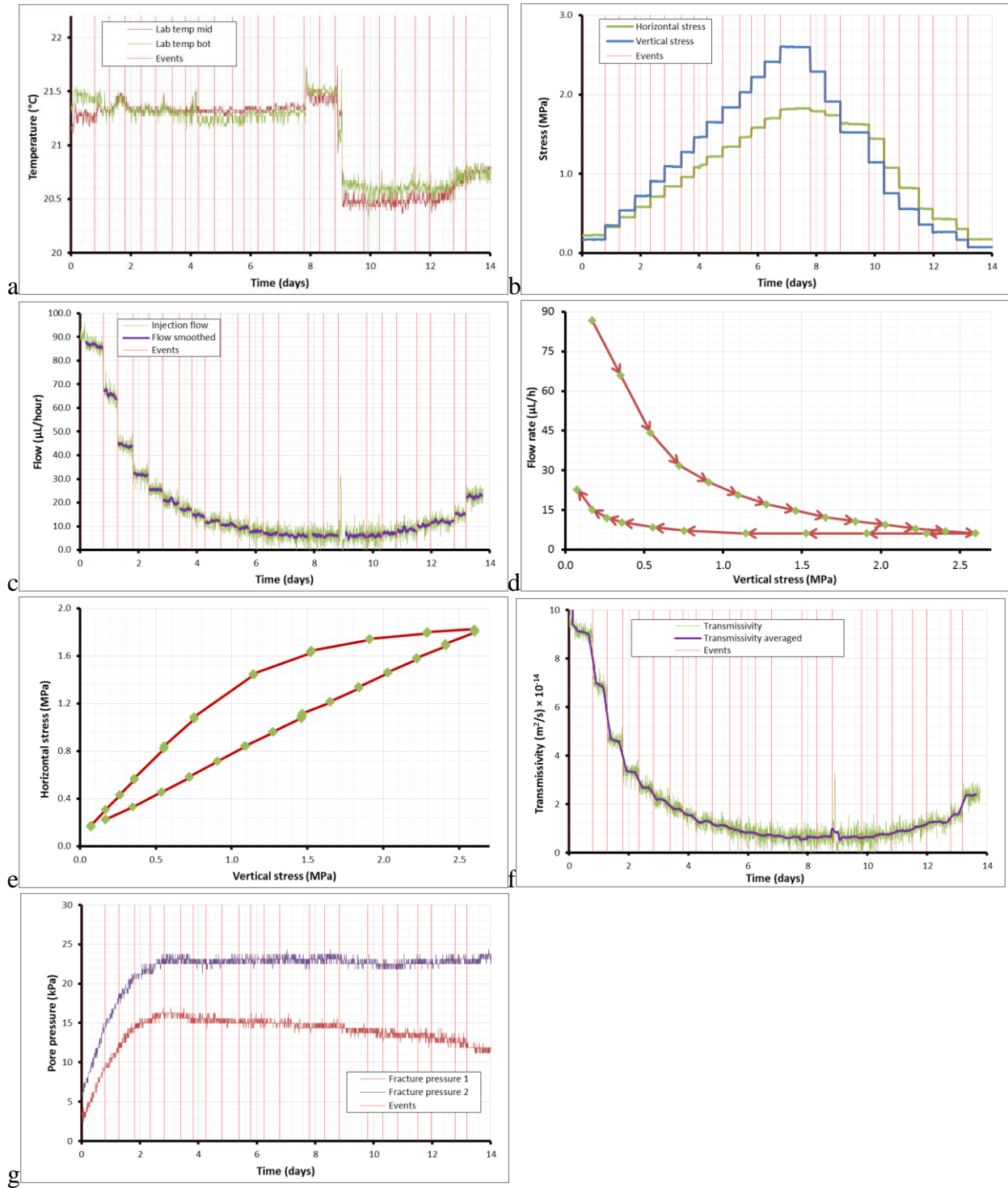


**Figure 11** - Results from test ASR\_Tau01\_30wLU: a) Temperature; b) Loading and unloading steps showing the stepwise variation in vertical stress and corresponding variations in horizontal stress; c) Hydraulic flow with time; d) Hydraulic flow variation with vertical stress; e) Horizontal stress versus vertical stress plot showing hysteresis; f) Hydraulic transmissivity; g) Pore pressures within the slip plane.

	Stage	Vertical stress (MPa)	Time (days)
<b>LOADING</b>	1	0.2	0
	2	0.4	1
	3	0.5	2
	4	0.7	3
	5	0.9	4
	6	1.1	5
	7	1.3	6
	8	1.5	7
	9	1.7	8
	10	1.8	9
	11	2.0	10
	12	2.2	11
	13	2.4	12
	14	2.6	13
<b>UNLOADING</b>	15	2.5	14
	16	2.3	15
	17	2.1	16
	18	1.9	17
	19	1.8	18
	20	1.6	19
	21	1.4	20
	22	1.2	21
	23	1.0	22
	24	0.8	23
	25	0.6	24
	26	0.4	25
	27	0.2	26

**Table 4** - The loading and unloading stages in test ASR\_Tau05\_30wLU.

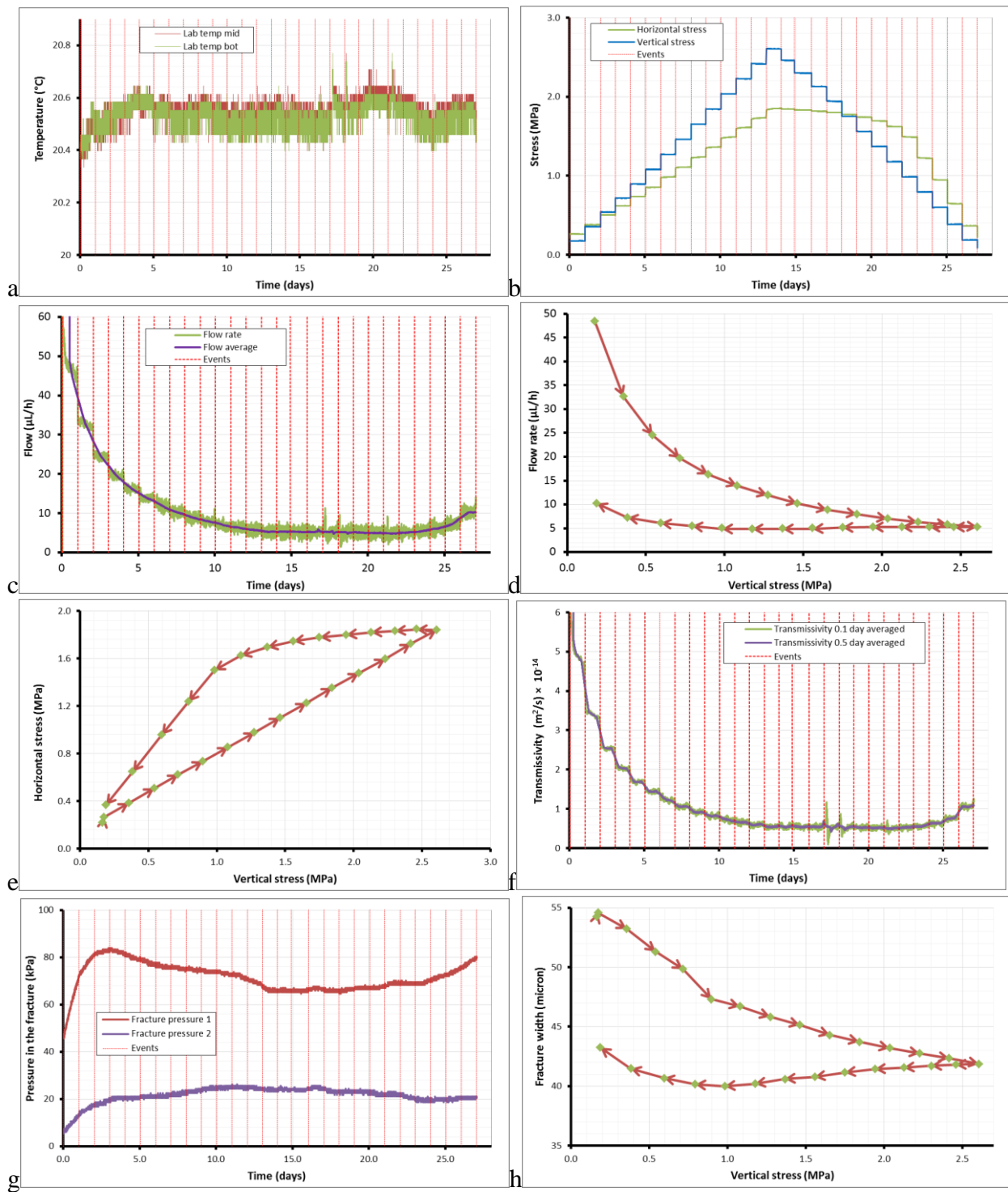


**Figure 12** - Results from test ASR\_Tau05\_30wLU: a) Temperature; b) Loading and unloading steps showing the stepwise variation in vertical stress and corresponding variations in horizontal stress; c) Hydraulic flow with time; d) Hydraulic flow variation with vertical stress; e) Horizontal stress versus vertical stress plot showing hysteresis; f) Hydraulic transmissivity; g) Pore pressures within the slip plane; h) Fracture width variation. Since only one eddy-current sensor was used in this experiment the decrease in fracture width during unloading might have been a result of the tilting of the top block when the vertical stress was decreased.

The abrupt increase in laboratory temperature during unloading is presented in additional detail in Figure 13a. Abrupt increases in temperature were detected at Days 17, 18 and 21.

Corresponding increase in flow rate and transmissivity were also observed (Figure 13 b&c). Figure 13d shows the increase in horizontal stress to vertical stress ratio during unloading.

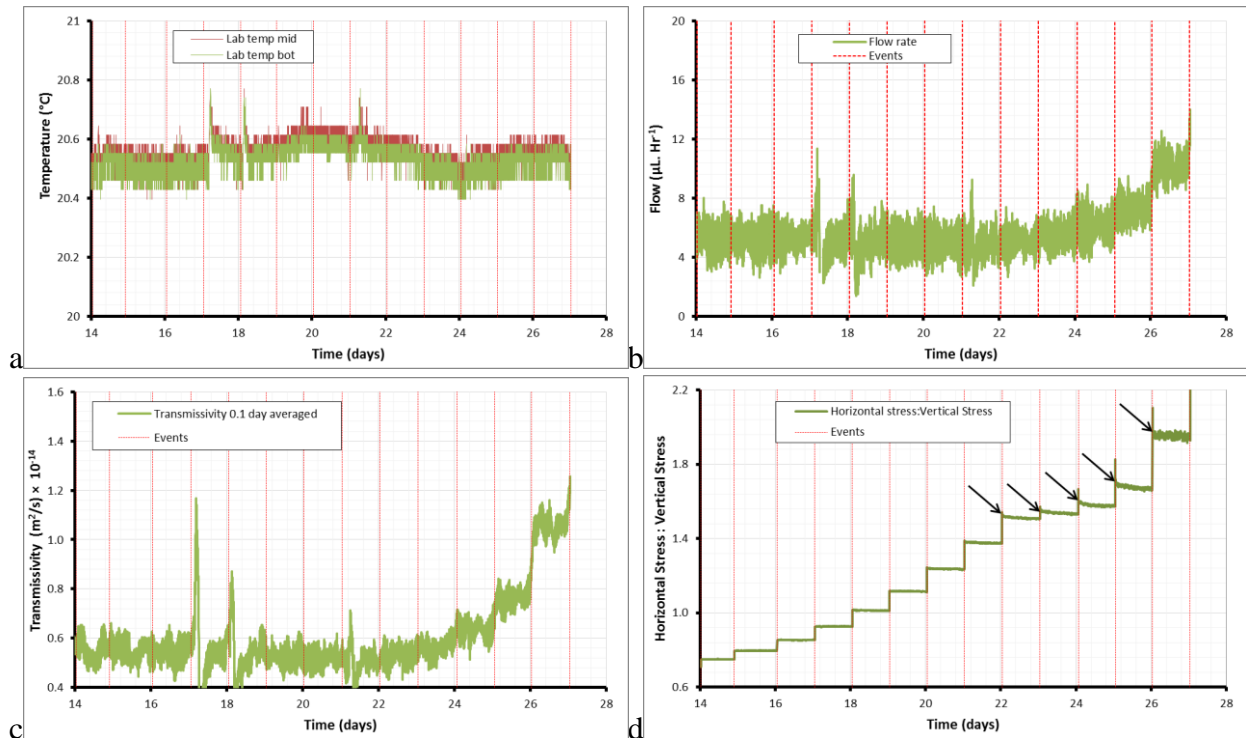


**Figure 13** –Detail of effect of temperature fluctuations during the unloading stages in experiment ASR\_Tau05\_30wLU. a) Temperature; b) Flow rate; c) Transmissivity; d) Horizontal stress to vertical stress ratio. The arrows indicate the initial increase in horizontal stress to vertical stress ratio during unloading which might be due to the movement of the top block during each stepwise decrease in vertical stress. These steps also mark the stages where horizontal stress decreases rapidly during unloading as shown in Figure 12e.

### 3.1.1.2 DISCUSSION

A comparison of results from experiments ASR\_Tau01\_30wLU and ASR\_Tau05\_30wLU (Figure 14) shows that an increase in vertical stress resulted in a corresponding linear increase in horizontal stress during loading. The hysteresis in horizontal stress observed during unloading may be attributed to the cohesive strength of the clay as a result of hydrogen bonding between adsorbed water molecules and atomically charged clay mineral surfaces (Ikari & Kopf, 2011; Marry *et al.*, 2008). The decrease in flow rate and transmissivity during loading suggests the progressive constriction of fluid pathways during loading. The initial dissimilarities in flow rate during loading between ASR\_Tau01\_30wLU and ASR\_Tau05\_30wLU might have been due to the initial packing of the clay platelets and the geometry of the initial pathways formed. However, at a vertical stress of 2.6 MPa, flow decreased to a uniform value of  $5 \mu\text{L}\cdot\text{h}^{-1}$  irrespective of the initial flow rates. After complete unloading, flow increased uniformly in both tests ASR\_Tau01\_30wLU and ASR\_Tau05\_30wLU to  $12 \pm 2 \mu\text{L}\cdot\text{h}^{-1}$  (Figure 14). The hysteresis in flow rate and horizontal stress during a loading and unloading cycle suggests that understanding the complete stress history rather than the current stress state is of paramount importance in predicting the flow of fluids through fractures. Heterogeneous distribution of pore pressures away from the central pore fluid injection port within the idealised slip plane suggests that the hydraulic flow through clays occurs via localised channel/s within the slip plane. Fluctuations in laboratory temperatures during the course of the experiments revealed an inexplicit relationship to fluid flow rates. In ASR\_Tau01\_30wLU an abrupt decrease in temperature of  $1^\circ\text{C}$  on Day 9 from  $21.5^\circ\text{C}$  to  $20.5^\circ\text{C}$  resulted in the flow rate increasing from  $5 \mu\text{L}\cdot\text{h}^{-1}$  to  $30 \mu\text{L}\cdot\text{h}^{-1}$  and transmissivity values increasing from  $0.3 \times 10^{-14} \text{m}^2\cdot\text{s}^{-1}$  to  $3.3 \times 10^{-14}$

$\text{m}^2 \cdot \text{s}^{-1}$  (Figure 11 c & f). An increase in temperature in ASR\_Tau05\_30wLU of  $0.2^\circ\text{C}$  resulted in a flow rate increase from  $4 \mu\text{l} \cdot \text{h}^{-1}$  to  $11 \mu\text{l} \cdot \text{h}^{-1}$  and a corresponding doubling of transmissivity from  $0.6 \times 10^{-14} \text{m}^2 \cdot \text{s}^{-1}$  to  $1.2 \times 10^{-14} \text{m}^2 \cdot \text{s}^{-1}$  (Figure 13 a-c). This short-term increase in flow rate and transmissivity may be attributed to the thermal expansion and/or contraction of water or stainless steel pore fluid pump reservoir and pipe networks with rise or fall in laboratory temperature respectively. The exact process responsible for this anomalous observation is unclear from the present dataset. The diverse differences in the injection pressure and the pressure within the slip plane (Figure 11g & Figure 12g) suggests that the concept of effective stress (total stress minus pore fluid pressure) cannot be applied consistently to clays with the same assurance as it has been applied in the study of more porous and permeable rocks such as sandstones and fractured crystalline rocks (Cuss *et al.*, 2011).

Kaolinite being a non-swelling clay might behave differently to other swelling clays such as montmorillonite, illite and smectite during hydraulic flow. The flow rates in fault gouges filled with swelling-clays is expected to be significantly lower compared to that of a non-swelling clay. The process of swelling is likely to constrict any open pathways. Additional experiments with swelling clays are necessary to completely understand the hydraulic flow properties through a slip plane containing a mixture of swelling and non-swelling clays.

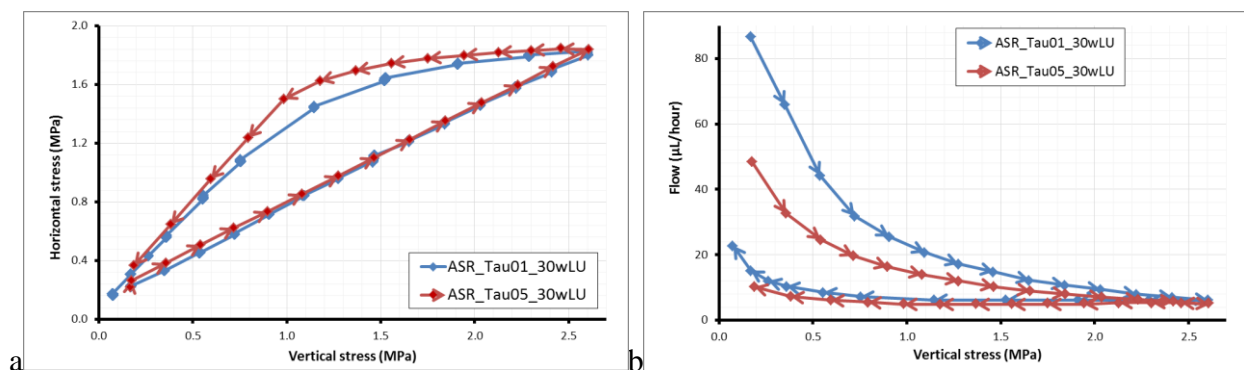


**Figure 14** – Comparison of results from experiments ASR\_Tau01\_30wLU and ASR\_Tau05\_30wLU. a) Horizontal stress versus vertical stress plot. Similar results are seen during loading, with only marginally differences seen during unloading; b) Flow versus vertical stress. During loading the initial flow rate in ASR\_Tau01\_30wLU were higher ( $90 \mu\text{l} \cdot \text{h}^{-1}$ ) than the initial flow rate observed in ASR\_Tau05\_30wLU ( $50 \mu\text{l} \cdot \text{h}^{-1}$ ) during the initial part of the loading cycle. After loading to 2.6 MPa flow rate decreased to  $5 \mu\text{l} \cdot \text{h}^{-1}$  for tests. Both tests also followed a similar unloading path.

### 3.1.2 Gas flow during loading and unloading through an idealised slip plane

Three loading and unloading experiments (ASR\_Tau07\_30gLU, ASR\_Tau08\_30gLU, and ASR\_Tau14\_30gLU) were conducted with gas injection to understand the effect of stress on gas flow through fractures. In all the experiments, vertical load was varied in steps of  $0.2 - 0.3 \text{MPa}$  per day. These experiments were performed at gas injection pressures equivalent to the pressure at which gas flow was detected (gas breakthrough pressures) which were different in each experiment. The injection pressures used were 3.55, 4.95, and 4.45 MPa for ASR\_Tau07\_30gLU, ASR\_Tau08\_30gLU, and ASR\_Tau14\_30gLU respectively. The experimental stages are listed in Table 5.

#### 3.1.2.1 RESULTS

In ASR\_Tau07\_30gLU, the experimental slip plane was loaded and unloaded in steps at a constant gas injection pressure of 3.55 MPa (Figure 15). The temperature within the laboratory was maintained at  $20 \pm 0.25^\circ\text{C}$  throughout the test (Figure 15a). The vertical stress was increased in steps of  $0.2 - 0.3 \text{MPa}$  per day up to a maximum stress of 2.6 MPa and decreased in

similar steps to 0.4 MPa and the corresponding variations in gas flow rate were recorded (Table 5, Figure 15b). As stated earlier, vertical load was varied only after gas flow through the slip plane had been achieved. During the loading stages of the experiment, flow rate increased and decreased randomly from  $100 \mu\text{l.h}^{-1}$  at 0.4 MPa through  $80 \mu\text{l.h}^{-1}$  at 0.5 – 0.7 MPa and  $117 \mu\text{l.h}^{-1}$  at 0.9 – 1.1 MPa to  $225 \mu\text{l.h}^{-1}$  at a normal stress of 1.3 MPa (see Figure 15 c&d). Subsequent loading of the slip plane to a maximum stress of 2.6 MPa resulted in a steady decrease in flow rate from  $225 \mu\text{l.h}^{-1}$  to  $90 \mu\text{l.h}^{-1}$ . During unloading, gas flow rate increased slowly from  $90 \mu\text{l.h}^{-1}$  at 2.6 MPa to  $144 \mu\text{l.h}^{-1}$  at 1.2 MPa. Significant increase in flow rate was observed during further unloading with flow rate increasing to  $186 \mu\text{l.h}^{-1}$ ,  $360 \mu\text{l.h}^{-1}$ , and  $961 \mu\text{l.h}^{-1}$  at 1.0 MPa, 0.8 MPa, and 0.6 MPa respectively (Figure 15d). Horizontal stress increased linearly during loading and hysteresis was observed during the unloading stages (Figure 15e). The significant increase in flow rate on Day 27 during unloading appears to be related to the corresponding rapid decrease in horizontal stress as shown in Figure 15c,e. Pore pressure within the slip plane remained more or less unchanged during the entire duration of the experiment irrespective of the high injection pressure around 1cm away from the pore pressure sensors (Figure 15f). Horizontal stress to vertical stress ratio decreased during loading from 1 to 0.7 and during unloading increased remarkably to 1.6 (Figure 15g). Horizontal stress to vertical stress ratios above 1.5 corresponded to abrupt increases in flow rate as observed in Figure 15c,d. Similar to fluid flow, transmissivity increased and decreased during the initial loading stages up to 1.3 MPa. However, with further loading, transmissivity decreased from  $1.2 \times 10^{-17} \text{ m}^2.\text{s}^{-1}$  at 1.3 MPa to  $4 \times 10^{-18} \text{ m}^2.\text{s}^{-1}$  at a maximum vertical stress of 2.6 MPa (Figure 15h). During unloading, transmissivity increased gradually from  $4 \times 10^{-18} \text{ m}^2.\text{s}^{-1}$  to  $7 \times 10^{-18} \text{ m}^2.\text{s}^{-1}$  at 1.2 MPa vertical stress. With further unloading transmissivity of gas increased by up to an order of magnitude to  $5.1 \times 10^{-17} \text{ m}^2.\text{s}^{-1}$  at a vertical stress of 0.6 MPa. The thickness of the gouge within the slip plane decreased from  $48.1 \mu\text{m}$  to  $34.5 \mu\text{m}$ , and during unloading decreased further to  $34.1 \mu\text{m}$  (Figure 15i).

In experiment ASR\_Tau08\_30gLU, the kaolinite gouge-filled slip plane was subjected to a loading and unloading cycle and the effect of variations in load on gas flow was studied. The results are presented in Figure 16. Random increase and decrease in flow rate was observed during the initial part of the loading cycle (Figure 16 c&d) as observed in previously. The flow rate fluctuated between  $165 \mu\text{l.h}^{-1}$  and  $550 \mu\text{l.h}^{-1}$  during stepwise loading from 0.4 MPa to 1.1 MPa. Further loading resulted in more or less steady decrease in flow rate from  $550 \mu\text{l.h}^{-1}$  at 1.1 MPa to  $276 \mu\text{l.h}^{-1}$  at 2.6 MPa. During unloading, flow rate increased gradually from  $276 \mu\text{l.h}^{-1}$  at 2.6 MPa to  $298 \mu\text{l.h}^{-1}$  at 1.4 MPa. The final unloading step at 0.4 MPa saw a considerable increase in flow resulting in approximately  $1000 \mu\text{l.h}^{-1}$ . Horizontal stress increased linearly with loading and displayed hysteresis during unloading (Figure 16e). The pressure within the gouge remained approximately zero throughout the entire duration of the loading and unloading stages (Figure 16f). Horizontal stress to vertical stress ratio decreased during loading from 1.0 to 0.7 and during unloading significantly increased to 1.8 (Figure 16g). The transmissivity of gas through the slip plane fluctuated between  $6 \times 10^{-18} \text{ m}^2.\text{s}^{-1}$  and  $2 \times 10^{-17} \text{ m}^2.\text{s}^{-1}$  during the initial loading stages and decreased to  $1 \times 10^{-17} \text{ m}^2.\text{s}^{-1}$  (Figure 16h). During unloading of the slip plane gas transmissivity increased to  $3.8 \times 10^{-17} \text{ m}^2.\text{s}^{-1}$  at 0.4 MPa vertical stress. Fracture width decreased with loading from  $65 \mu\text{m}$  to  $51 \mu\text{m}$  and during unloading remained relatively constant (Figure 16i).

A third experiment (ASR\_Tau14\_30gLU) was performed at identical test conditions (Figure 17), with the slip plane loaded in steps to a maximum vertical stress of 1.8 MPa followed by unloading (Figure 17b). Flow rate fluctuated during the loading stages as observed in the previous experiments. The experiment was commenced at a flow rate of  $85 \mu\text{l.h}^{-1}$  at an injection pressure of 4.45 MPa and a vertical stress of 0.3 MPa (Figure 17c,d). However, an increase in vertical stress to 0.5 MPa resulted in a remarkable increase in flow rate from  $85 \mu\text{l.h}^{-1}$  to  $262 \mu\text{l.h}^{-1}$ . Even though the flow rate fluctuated during loading, the general trend shows a decrease in flow rate during loading (Figure 17d). Flow at the maximum vertical stress of 1.8 MPa was  $158 \mu\text{l.h}^{-1}$ . With unloading flow rate increased to  $548 \mu\text{l.h}^{-1}$  at a vertical stress of 0.6 MPa. Hysteresis

in horizontal stress was observed during the unloading stages and the pore pressures within the fracture remained relatively unaffected during the course of the experiment (Figure 17e,f). Horizontal stress to vertical stress ratio decreased from 0.9 to 0.7 during loading and subsequently increased to 1.5 during unloading (Figure 17g). Transmissivity of gas through the slip plane increased from  $3.8 \times 10^{-18} \text{ m}^2 \cdot \text{s}^{-1}$  to  $1 \times 10^{-17} \text{ m}^2 \cdot \text{s}^{-1}$  during a slight increase in vertical stress from 0.3 MPa to 0.5 MPa (Figure 17h). Further loading resulted in the gas transmissivity to decrease randomly to  $5.9 \times 10^{-18} \text{ m}^2 \cdot \text{s}^{-1}$  at a vertical stress of 1.8 MPa. During the unloading stage, transmissivity increased gradually to  $8.4 \times 10^{-18} \text{ m}^2 \cdot \text{s}^{-1}$  at a vertical stress of 1.0 MPa followed by an abrupt increase to  $2.3 \times 10^{-17} \text{ m}^2 \cdot \text{s}^{-1}$  at a low stress of 0.6 MPa. When vertical stress was decreased further to 0.2 MPa, transmissivity increased by an order of magnitude to  $1.8 \times 10^{-16} \text{ m}^2 \cdot \text{s}^{-1}$ . Contrary to ASR\_Tau07\_30gLU and ASR\_Tau08\_30gLU where only one fracture width measuring eddy-current sensor was employed, ASR\_Tau14\_30gLU used two fracture-width sensors. The fracture width measured by one sensor showed a decrease in fracture width with loading from 10  $\mu\text{m}$  to -9  $\mu\text{m}$  whereas the second sensor showed a corresponding increase in from 28  $\mu\text{m}$  to 75  $\mu\text{m}$  (Figure 17i). The opposite behaviour in fracture width evolution was observed during the unloading stage. The average fracture width showed unexpected increase from 22  $\mu\text{m}$  to 32  $\mu\text{m}$  during loading. However, during unloading the fracture width remained constant at  $33 \pm 1 \mu\text{m}$  (Figure 17i).

	ASR_Tau07_30gLU			ASR_Tau08_30gLU			ASR_Tau14_30gLU		
	Stage	Vertical Stress (MPa)	Time (Days)	Stage	Vertical Stress (MPa)	Time (Days)	Stage	Vertical Stress (MPa)	Time (Days)
Loading	1	0.4	3	1	0.4	11	1	0.3	28
	2	0.5	5	2	0.5	12	2	0.5	29
	3	0.7	6	3	0.7	13	3	0.7	30
	4	0.9	7	4	0.9	14	4	0.9	31
	5	1.1	8	5	1.1	15	5	1.1	32
	6	1.3	9	6	1.3	16	6	1.3	33
	7	1.5	10	7	1.5	17	7	1.4	35
	8	1.7	11	8	1.6	18	8	1.6	36
	9	1.8	12	9	1.8	19	9	1.8	37
	10	2.0	13	10	2.0	20	–	–	–
	11	2.2	14	11	2.2	21	–	–	–
	12	2.4	15	12	2.4	22	–	–	–
	13	2.6	16	13	2.6	23	–	–	–
Unloading	14	2.5	19	14	2.5	24	–	–	–
	15	2.3	20	15	2.3	25	–	–	–
	16	2.1	21	16	2.1	26	–	–	–
	17	1.9	22	17	1.9	27	–	–	–
	18	1.8	23	18	1.8	28	10	1.7	38
	19	1.6	24	19	1.6	29	11	1.5	39
	20	1.4	25	20	1.4	30	12	1.4	40
	21	1.2	26	21	1.2	31	13	1.2	41
	22	1.0	27	22	1.0	32	14	1.0	42
	23	0.8	28	23	0.8	33	15	0.8	43
	24	0.6	29	24	0.6	34	16	0.6	44
	25	0.4	30	25	0.4	35	17	0.4	45

**Table 5** – Loading and unloading stages during gas injection loading/unloading experiments ASR\_Tau07\_30gLU, ASR\_Tau08\_30gLU, and ASR\_Tau14\_30gLU.

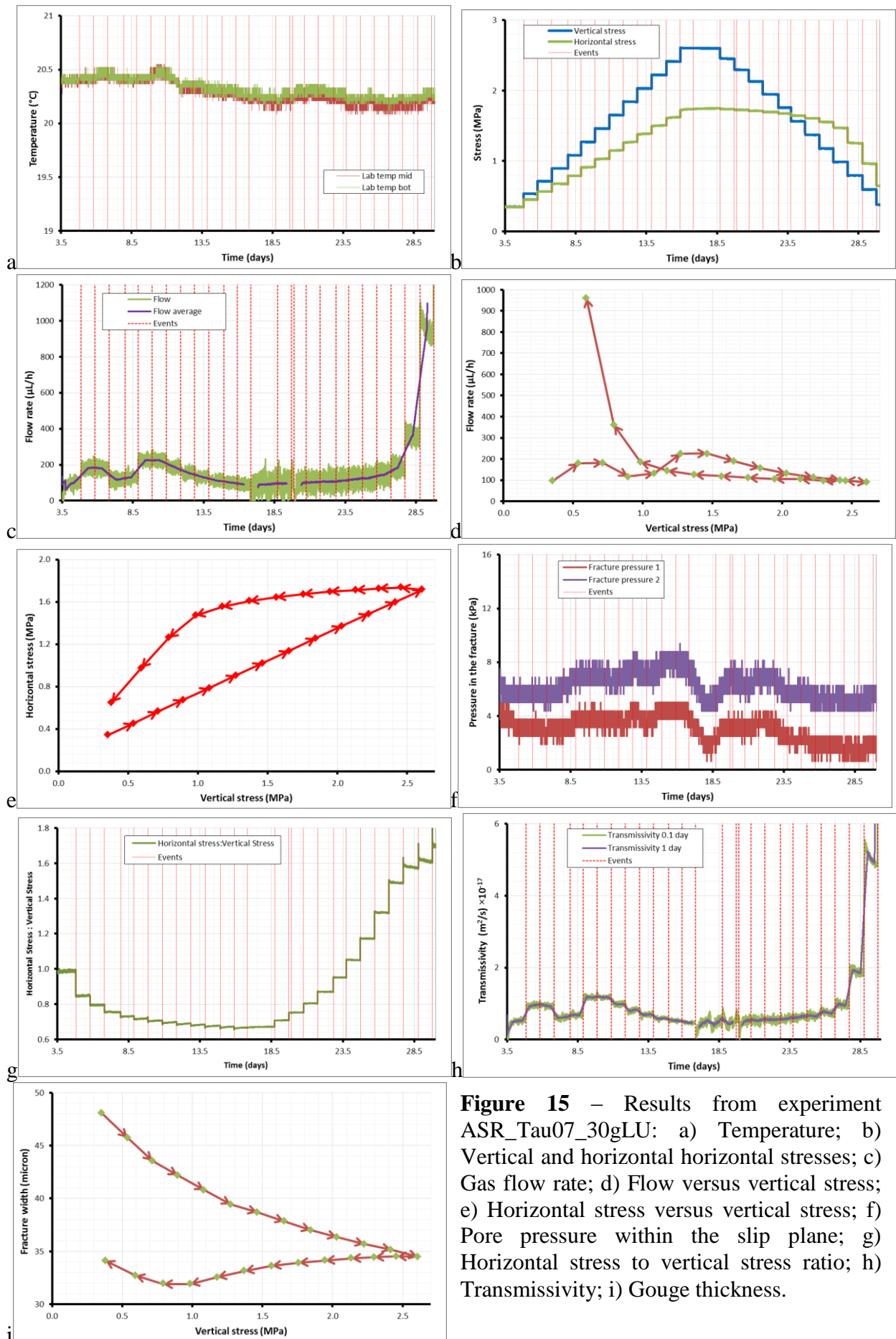


**Figure 15** – Results from experiment ASR\_Tau07\_30gLU: a) Temperature; b) Vertical and horizontal horizontal stresses; c) Gas flow rate; d) Flow versus vertical stress; e) Horizontal stress versus vertical stress; f) Pore pressure within the slip plane; g) Horizontal stress to vertical stress ratio; h) Transmissivity; i) Gouge thickness.

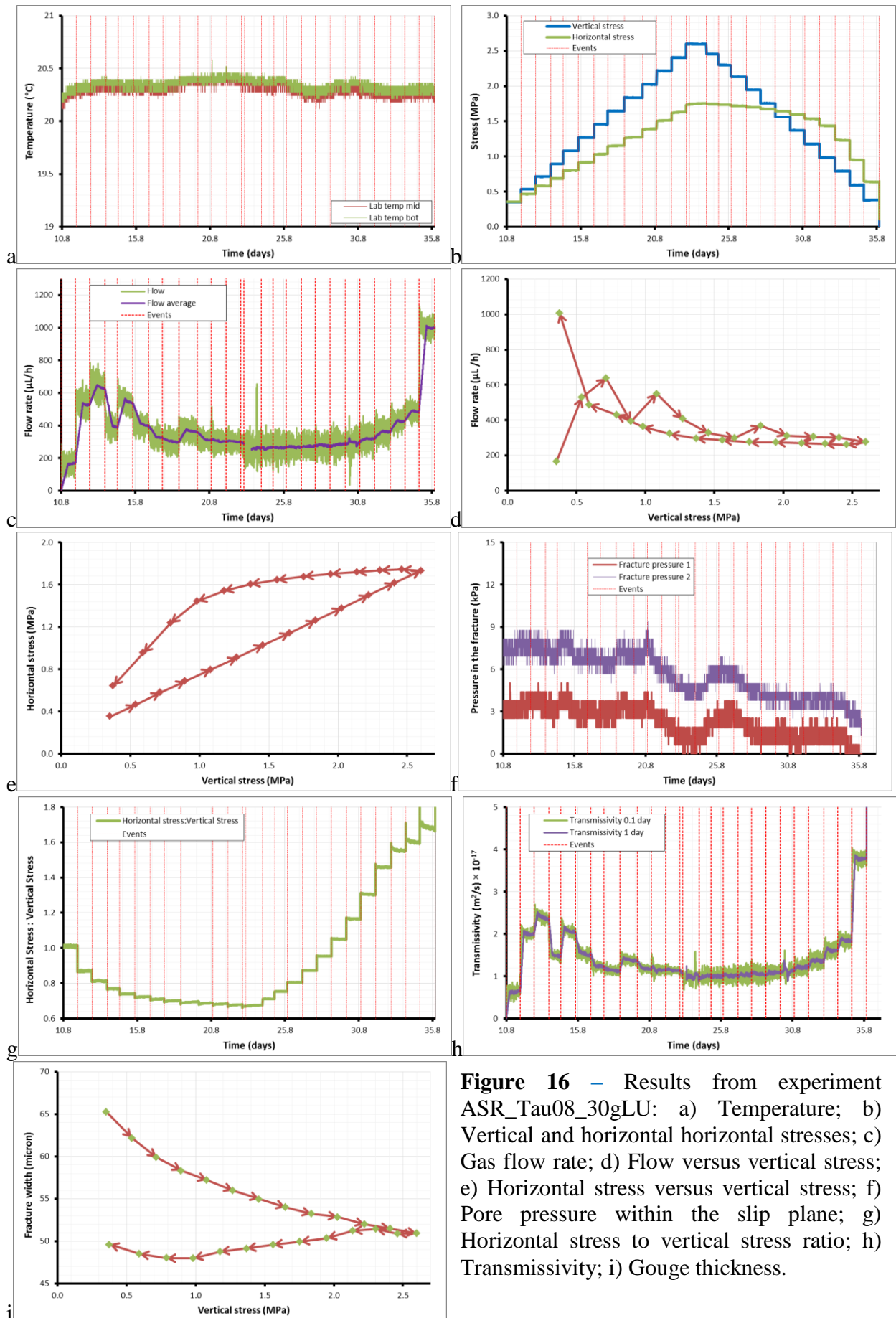


**Figure 16** – Results from experiment ASR\_Tau08\_30gLU: a) Temperature; b) Vertical and horizontal horizontal stresses; c) Gas flow rate; d) Flow versus vertical stress; e) Horizontal stress versus vertical stress; f) Pore pressure within the slip plane; g) Horizontal stress to vertical stress ratio; h) Transmissivity; i) Gouge thickness.

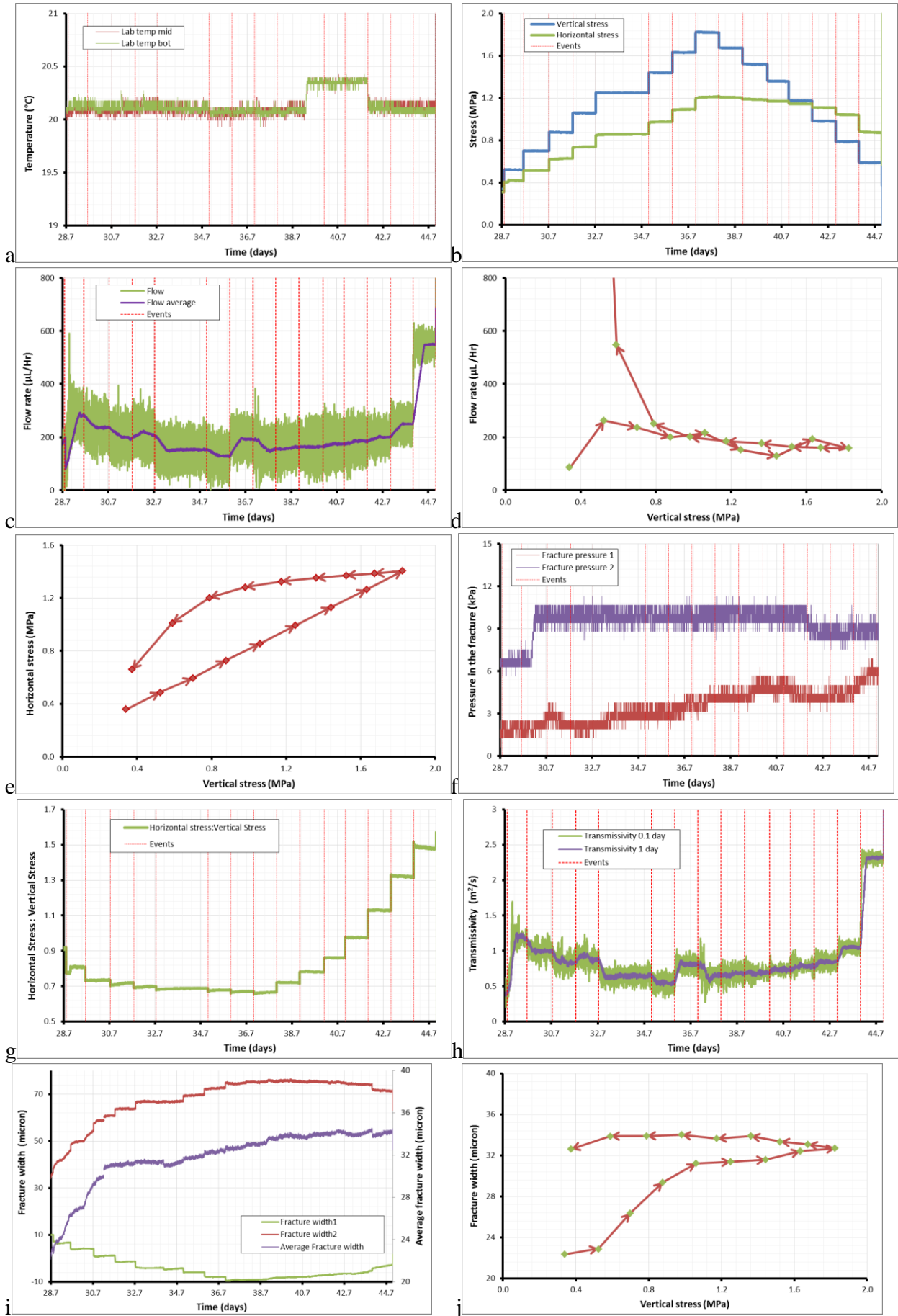


**Figure 17** – Results from experiment ASR\_Tau14\_30gLU: a) Temperature; b) Vertical and horizontal horizontal stresses; c) Gas flow rate; d) Flow versus vertical stress; e) Horizontal stress versus vertical stress; f) Pore pressure within the slip plane; g) Horizontal stress to vertical stress ratio; h) Transmissivity; i) Gouge thickness; j) Gouge thickness with vertical load.

### 3.1.2.2 DISCUSSION ON GAS INJECTION LOADING-UNLOADING EXPERIMENTS

The three gas injection loading-unloading experiments were initiated at dissimilar injection pressures of 3.55, 4.95, and 4.45 MPa. The injection pressures in these experiments corresponded to the pressures at which gas breakthrough was detected. Gas breakthrough pressure varied irrespective of identical sample preparation and sample assembly routines. This might be attributed to the formation of preferential pathways which exploited a multitude of inherent weaknesses within the gouge matrix which may have varied in each experiment. The flow rate of gas fluctuated seemingly in a random manner during the initial loading stages of the experiments (Figure 18a). However, during further loading a decrease in flow rate was observed. The random nature of flow rate variation during the initial loading stages may be due to the horizontal movement of the steel blocks during each step wise increase in load which in turn affected the geometry and nature of the gas flow-pathways. Flows observed during almost total unloading of the fracture were an order of magnitude higher than flow observed during the initial loading stages. The significant enhancement of flow during the unloading stages of the experiments may also be ascribed to the effect of movement of the steel blocks on the gas flow-pathways with each stepwise decrease in normal stress. Since different injection pressures were applied in each experiment, direct comparisons of the variations in flow rates between the different experiments were not attempted here. However, the flow rate of gas has been observed to be directly proportional to the injection pressure applied with higher injection pressures resulting in higher flow rates and vice versa. In experiment ASR\_Tau07\_30gLU run at an injection pressure of 3.55 MPa, the flow rate recorded at 1.8 MPa normal stress was  $112 \mu\text{l.h}^{-1}$ . In ASR\_Tau14\_30gLU performed at an injection pressure of 4.45 MPa, flow rate of  $158 \mu\text{l.h}^{-1}$  was recorded. In the case of ASR\_Tau08\_30gLU performed at the uppermost injection pressures amongst the experiments reported here, a flow rate of  $276 \mu\text{l.h}^{-1}$  was recorded at a normal stress of 1.8 MPa.

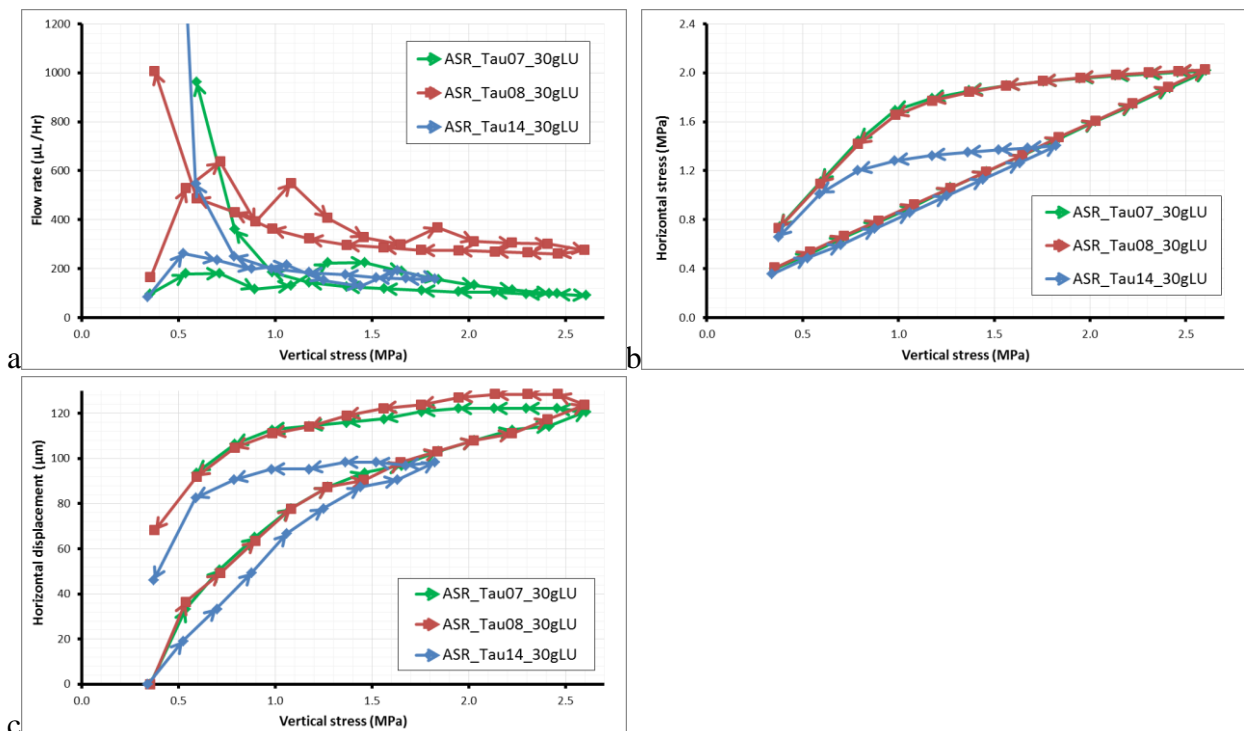


**Figure 18** – Comparison of results from tests ASR\_Tau07\_30gLU, ASR\_Tau08\_30gLU, and ASR\_Tau14\_30gLU. a) Flow rate versus vertical stress; b) Horizontal stress versus vertical stress showing hysteresis during unloading; c) Horizontal displacement with vertical stress.

Horizontal stress increased linearly with step wise increase in vertical stress during loading. However, prominent hysteresis was observed in horizontal stress during the unloading stages of

the experiment (Figure 18b). As discussed earlier, this hysteresis may be attributed to the cohesive strength of the clay as a result of hydrogen bonding between adsorbed water molecules and atomically charged clay mineral surfaces (Ikari & Kopf, 2011; Marry *et al.*, 2008). Even though horizontal movement of the top block was prevented as much as possible during the course of the experiment by securing the movement of the force actuator, horizontal displacements of 100 – 120  $\mu\text{m}$  were recorded in all the experiments. The amount of horizontal displacement appear to be linearly proportional to the degree of vertical loading with ASR\_Tau14\_30gLU which was subjected to a maximum vertical stress of 1.8 MPa recorded a horizontal displacement of 98  $\mu\text{m}$  whereas ASR\_Tau07\_30gLU and ASR\_Tau08\_30gLU which were subjected to a maximum vertical stress of 2.6 MPa underwent horizontal displacements of 120  $\mu\text{m}$  and 125 $\mu\text{m}$  respectively (Figure 18c). Since different gas injection pressures were employed in these experiments, the accurate determination of the effect of above mentioned horizontal displacement in decreasing the overall transmissivity of gas was not possible. However, shear displacement is a well-established self-sealing mechanism and would have contributed to some decrease in gas transmissivity and the contribution of shear mechanism in the decrease in gas transmissivity observed in these present experiments cannot be entirely ruled out.

### 3.1.3 Comparison of hydraulic flow and gas flow during loading and unloading

A direct comparison of the effect of water and gas transmissivity during loading and unloading was not feasible because of the different injection pressures used. Irrespective of these differences, a general decrease in flow rate was observed during loading in the case of both water and gas injection experiments (Figure 19a). Hydraulic flow through the gouge-filled slip plane decreased with corresponding increase in normal stress. In the case of gas injection, the flow rate through the slip plane decreased and increased with corresponding normal load increase suggesting that new gas flow-pathways were being formed during the initial loading stages. In the case of water injection experiments, flow rates increased to only 0.25 of the starting flow rate during unloading (Figure 14b). However, in the case of gas injection, the flow rates observed during the unloading stages were up to an order of magnitude higher than that observed during the loading stages (Figure 18a). These observations suggest that the mechanism of gas flow and water flow through a gouge filled fracture during loading and stress-relaxation are significantly different. The gas flow properties through fractures are likely to be severely influenced by stress relaxation during tectonic uplift compared to that of hydraulic flow. Moreover, the pore pressures within the experimental slip plane recorded via two orthogonally located pore pressure ports located 10 mm from the central injection port remained unchanged throughout the duration of the experiment irrespective of the high injection pressure (Figure 8b). This inhomogeneous distribution of pore pressures within the slip plane indicates that the fluid flow must have occurred via localised fluid pathways within the fracture plane as reported by Cuss *et al.* (2012).

In both water and gas injection experiments, horizontal stress increased linearly during loading (Figure 14a, Figure 19b). A close correlation between the horizontal stress to vertical stress ratio and increase in flow rate was observed during the unloading stage with manifest increase in flow rate during unloading occurring when the horizontal stress to vertical stress ratio values were above the starting ratio prior to loading. The present observations indicate the importance of horizontal stress to vertical stress ratio in determining the rate of fluid flow through fractures as reported by Zoback *et al.* (1985) and Brudy *et al.* (1997). Prominent hysteresis in horizontal stress was observed during the unloading stage and implies that understanding the stress history of the fractured rocks is of paramount importance in predicting the fluid flow behaviour. Complex stress histories are common for fractured crystalline bedrock which may have undergone complex subsidence and uplift histories, with multiple stressing and stress-relaxation events. Hence the predictions of fluid flow behaviour through fractures based on mere datasets of present-day stress regimes are insufficient and are likely to result in erroneous predictions of fluid flow behaviour.

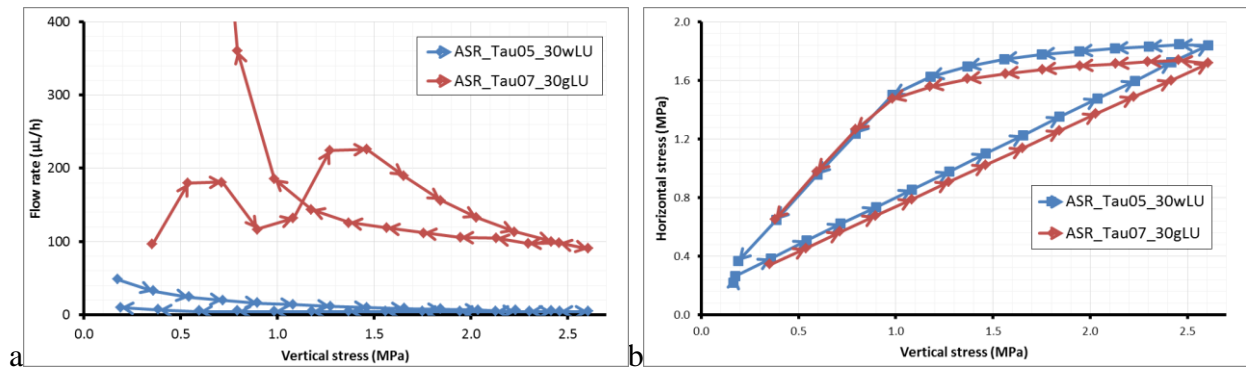


**Figure 19** – Comparison of the hydraulic and gas injection experiments during loading and unloading. a) Flow rate versus vertical stress plot for water injection experiment ASR\_Tau05\_30wLU and gas injection experiment ASR\_Tau07\_30gLU. b) Horizontal stress versus vertical stress plot showing identical hysteresis in horizontal stress in the case of water and gas injection experiments.

### 3.2 FRACTURE TRANSMISSIVITY EVOLUTION DURING SHEAR

Test ASR\_Tau02\_30wLUS was carried out to understand the influence of shear on fracture fluid flow.

#### 3.2.1 Experimental methodology

The experiment was performed using water as the permeant. The kaolinite gouge filled slip plane was subjected to independent variations in vertical load, horizontal displacement rate, and injection pressure while keeping other parameters constant. The different stages involved in ASR\_Tau02\_30wLUS experiment are listed in Table 6.

Stage	Pore pressure (kPa)	Vertical load pump (kPa)	Horizontal displacement rate (mm.day <sup>-1</sup> )	TIME (days)
1	1000	5000	0	0.0
2	1000	10000	0	5.8
3	1000	1000	0	12.1
4	1000	1000	0.3	14.2
5	1000	2000	0.3	17.8
6	1000	3000	0.3	27.0
7	1000	3000	0.9	33.9
8	1000	3000	0	38.1
9	2000	3000	0	39.8
10	2000	3000	0	40.1

**Table 6** – Experimental stages of test ASR\_Tau02\_30wLUS.

Stages 1 to 3 aimed to understand the effect of vertical stress variation on fluid flow through the gouge. In stage 1 the vertical stress was increased to 0.96 MPa while the injection pressure was maintained constant at 1 MPa and the resulting flow rate was monitored. In stage 2 at day 5.8, the vertical stress was increased from 0.96 MPa to 1.86 MPa while maintaining other parameters constant. In Stage 3 the vertical stress was reduced to 0.15 MPa and the effect on flow rate was monitored. Stages 3 to 7 were carried out to understand the effect of shearing and vertical load on fluid flow through the gouge. In stage 4 the slip plane was displaced horizontally at a rate of 0.3 mm.day<sup>-1</sup>. In stage 5 the vertical stress was increased from 0.17 MPa to 0.37 MPa and the corresponding variation in flow rate was analysed. In stage 6 the vertical stress was increased

from 0.37 MPa to 0.56 MPa whilst the sample still underwent shear. The horizontal displacement rate was increased from 0.3 mm.day<sup>-1</sup> to 0.9 mm.day<sup>-1</sup> in stage 7. Shearing was stopped in stage 8 and the hydraulic flow rate was monitored. In stage 9 the pore fluid injection pressure was increased from 1 MPa to 2 MPa and stage 10 signifies the end of the test. The time duration of each stage in ASR\_Tau02\_30wLUS and the boundary conditions of each stage are listed in Table 6.

### 3.2.2 Results and discussion

The results from stages 1 to 3 are shown in Figure 20. In stage 1 at a vertical stress of 0.96 MPa and a pore fluid injection pressure of 1 MPa an initial flow rate of 20  $\mu\text{l.h}^{-1}$  was recorded. However the flow rate decreased rapidly from to 8  $\mu\text{l.h}^{-1}$  within 7 hours. Subsequently, the flow rate further decreased gradually to 2.8  $\mu\text{l.h}^{-1}$  at Day 6. The initial sharp decline in flow rate may be attributed to the healing or the blocking of the fluid pathways. Since the pathways constantly evolved with time, no steady state flow was reached. The flow rate decreased marginally to 1.4  $\mu\text{l.h}^{-1}$  when the vertical stress acting on the slip plane was doubled in stage 2 from 0.96 MPa to 1.86 MPa. Data acquisition problems resulted in a loss of data from days 8.6 to 9.8. However, when the vertical stress was decreased in stage 3 from 1.86 MPa to 0.15 MPa, the hydraulic flow rate increased from 1.4  $\mu\text{l.h}^{-1}$  to 50  $\mu\text{l.h}^{-1}$ . As discussed in section 3.1.1, the hydraulic flow rate decreased during an increase in vertical stress and vice versa.

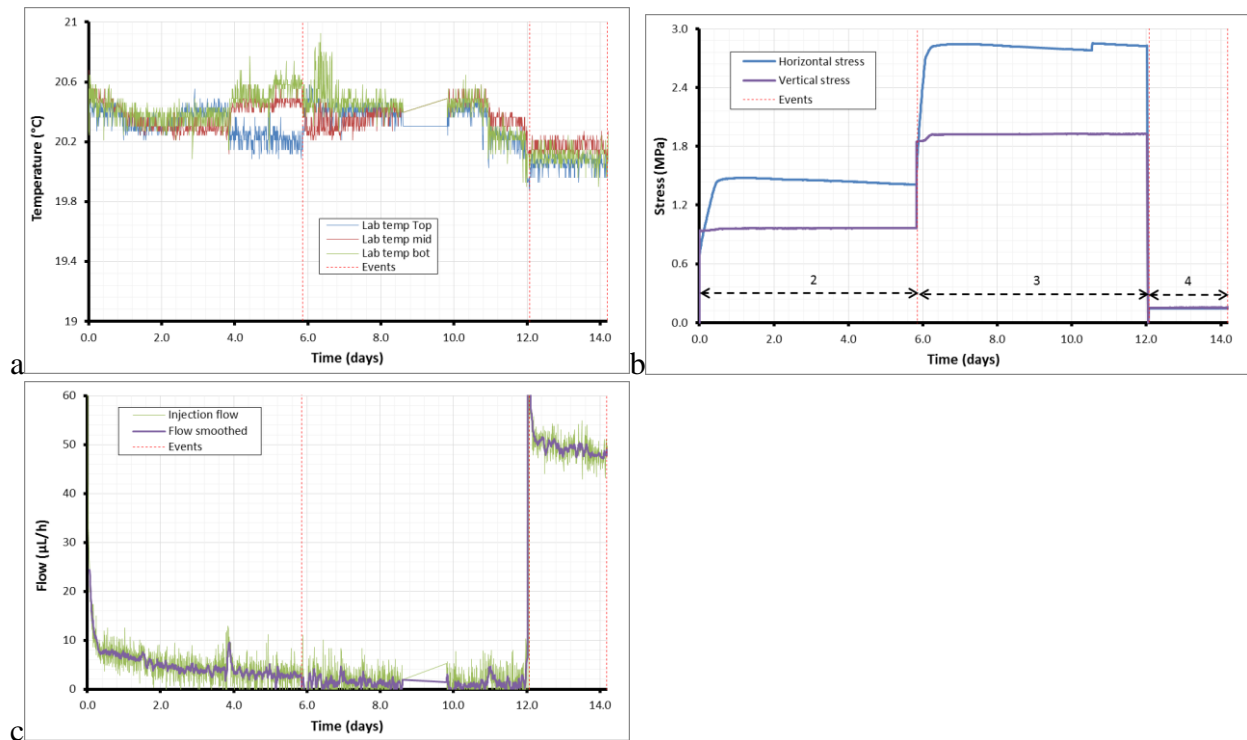


**Figure 20** - Results from stages 1 to 3 of test ASR\_Tau02\_30wLUS. a) Temperature; b) Vertical and horizontal stress; c) Hydraulic flow.

The hydraulic flow rate under conditions of shear from stage 4 to 8 is shown in Figure 21. The temperature of the laboratory remained constant at  $20 \pm 0.2$  °C until day 32.1 when an abrupt increase of 0.5 °C occurred. Spikes in hydraulic flow were observed during the temperature fluctuation. However the effect of the temperature perturbations was negligible on the overall flow rate. At stage 4, the slip plane was subjected to horizontal movement at a rate of 0.3 mm.day<sup>-1</sup>. As a result of horizontal movement, the hydraulic flow rate decreased significantly from 50  $\mu\text{l.h}^{-1}$  to 29  $\mu\text{l.h}^{-1}$ . This suggests that shearing is an effective self-sealing mechanism and hence fractures undergoing shear are likely to be less conductive to hydraulic flow than fractures which are not experiencing any horizontal movement. An increase in vertical stress from 0.17 MPa to 0.37 MPa in stage 5 with simultaneous horizontal displacement rate of 0.3 mm.day<sup>-1</sup>

resulted in a further reduction in hydraulic flow from  $29 \mu\text{l.h}^{-1}$  to  $15 \pm 5 \mu\text{l.h}^{-1}$ . The flow rate failed to attain steady state conditions even after 10 days (stage 5). An increase in vertical stress from 0.37 MPa in stage 5 to 0.56 MPa in stage 6 led to a gradual decrease in flow rate from  $15 \pm 5 \mu\text{l.h}^{-1}$  to  $9 \pm 1 \mu\text{l.h}^{-1}$ . The horizontal displacement rate was increased from  $0.3 \text{ mm.day}^{-1}$  to  $0.9 \text{ mm.day}^{-1}$  during stage 7 resulting in a decrease in flow from  $9 \pm 1 \mu\text{l.h}^{-1}$  to  $5 \pm 1 \mu\text{l.h}^{-1}$ .

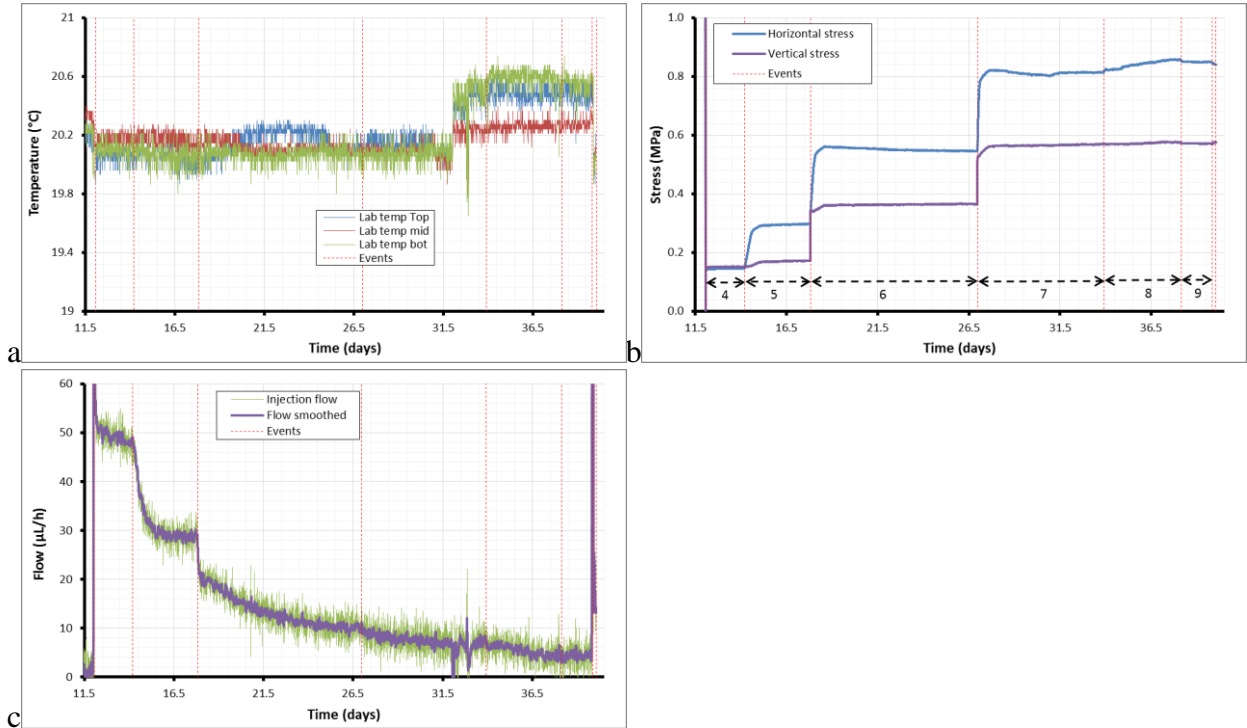


**Figure 21** - Results from stages 4 to 9 of the ASR\_Tau02\_30wLUS experiment. a) Temperature; b) Horizontal and vertical stress; c) Flow.

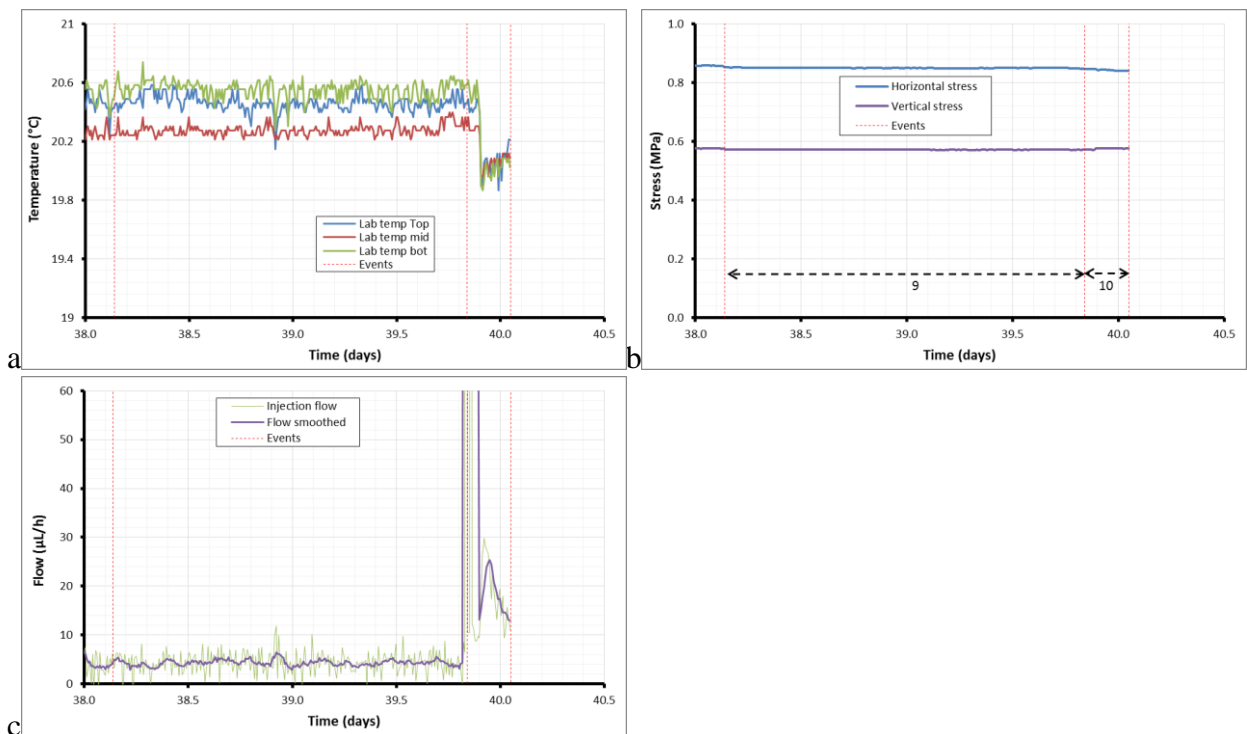


**Figure 22** - Results from stages 8 and 9 of the ASR\_Tau02\_30wLUS experiment. a) Temperature; b) Horizontal and vertical stress; c) Flow rate.

Flow rate remained virtually unchanged at  $5 \pm 1 \mu\text{l.h}^{-1}$  when the horizontal movement was stopped in stage 8 (Figure 22). This observation suggests that the sealing of fluid flow-pathways achieved as a result of shear displacement is perpetual and is not likely to be affected by the ending of any shear displacement that the rocks have undergone. The decrease in hydraulic flow-rate through the kaolinite gouge observed in the present experiment might be due to the stacking of individual kaolinite clay platelets in an orientation parallel to its c-axis thus forming a dense framework of clay material and concomitant reduction in bulk porosity of the gouge. However, shear experiments on intact Opalinus Clay by Cuss *et al.* (2011) have shown evidence of enhanced flow as a result of the formation of new fractures during shearing. An increase in hydraulic injection pressure from 1 MPa to 2 MPa during stage 9 resulted in an increase in hydraulic flow from  $5 \pm 1 \mu\text{l.h}^{-1}$  to  $20 \pm 7 \mu\text{l.h}^{-1}$  even though steady state flow was not attained.

Flow progressively decrease form  $50 \mu\text{l.h}^{-1}$  at a vertical stress of 0.15 MPa to  $7 \mu\text{l.h}^{-1}$  at a vertical stress of 0.56 MPa (Figure 23a). From the results presented in Figure 20, Figure 21, and Figure 22 along with the results presented in Figure 23b, we conclude that an increase in vertical stress and shear rate leads to a general decrease in hydraulic flow rate and on the other hand an increase in hydraulic injection pressure results in an increase in hydraulic flow rate.

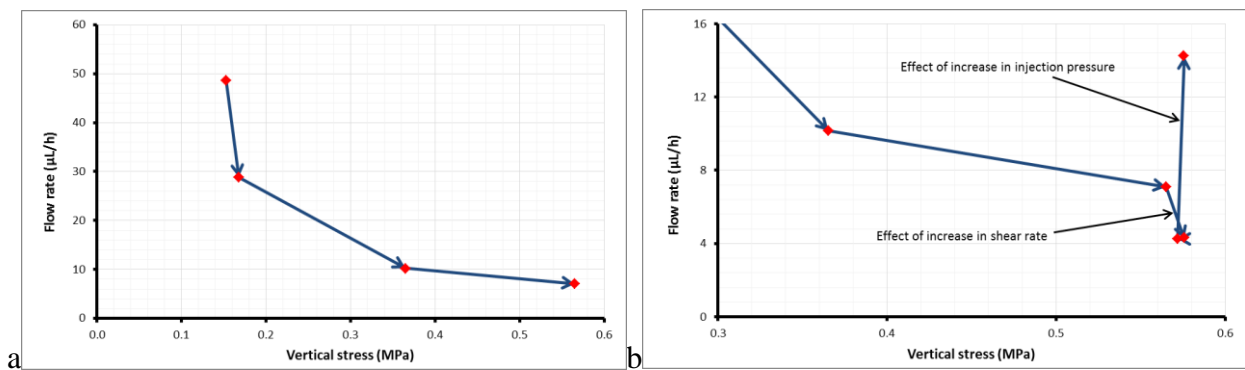


**Figure 23** – Summary of observations for test ASR\_Tau02\_30wLUS. a) Variation in flow rate with increasing vertical stress; b) Effect of increase in shear rate and increase in injection pressure on hydraulic flow rate.

### 3.2.3 The effect of shearing on hydraulic flow rate

In order to understand the magnitude of flow rate reduction during shearing, a comparison of hydraulic flow rate evolution during loading-unloading experiments with horizontal movement (ASR\_Tau02\_30wLUS) and without horizontal movement (ASR\_Tau05\_30wLU) was done. The results are presented in Figure 24. The initial hydraulic flow rates recorded in the experiments ASR\_Tau05\_30wLU and ASR\_Tau02\_30wLUS were similar at  $49 \mu\text{l.h}^{-1}$ . However, in ASR\_Tau02\_30wLUS the slip plane was subjected to shear at a rate of  $0.3 \text{ mm.day}^{-1}$  and the horizontal movement resulted in approximately 40% reduction in hydraulic flow rate (Figure 24). With progressive loading of the slip plane under conditions of shear resulted in a flow rate of  $7 \mu\text{l.h}^{-1}$  at a vertical stress of 0.56 MPa. On the other hand, under conditions of no horizontal movement, vertical stress as high as 2.04 MPa was required to reduce the hydraulic flow rate to  $7 \mu\text{l.h}^{-1}$ . These observations suggest that shear displacement along a fracture plane is an efficient sealing mechanism and the effect of shear on sealing is considerably more pronounced than that of the effect of an increase in vertical stress.

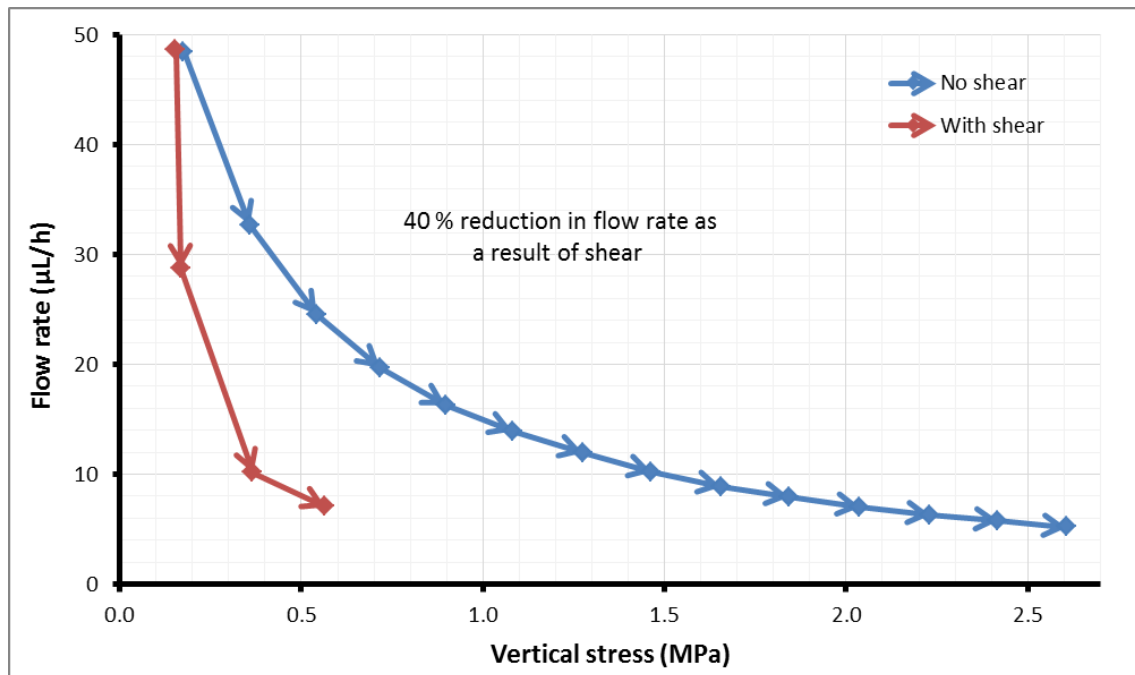


**Figure 24** - The effect of shearing on hydraulic flow, resulting in a 40% reduction in flow.

### 3.3 INVESTIGATION OF FAULT-VALVE BEHAVIOUR DURING GAS FLOW

Experiment ASR\_Tau06\_30gGI was initially planned to understand the effect of loading and unloading on the rate of flow of helium gas through a kaolinite gouge-filled experimental slip plane. A comparison with the observations of hydraulic flow (test ASR\_Tau05\_30wLU) could then be made. However, the injection pressure of 1 MPa applied was far below the gas entry/breakthrough pressures required for gas flow through the slip plane. Consequently it was decided to test for gas entry pressures in the current experimental setup and investigate the likelihood of studying the fault-valve behaviour during gas flow through fractures.

#### 3.3.1 Experimental methodology

Experiment ASR\_Tau06\_30gGI included 7 stages lasting 28 days in total. Stage 1 was performed at a vertical stress of 0.17 MPa and a constant gas injection pressure of 1 MPa, with gas flow monitored. Since no gas flow was detected, constant gas injection rate was commenced. In stage 2, gas was injected into the slip plane at a constant injection rate of  $500 \mu\text{l.h}^{-1}$  and the corresponding increase in gas pressure was monitored. As the gas entry/breakthrough pressure was reached an abrupt drop in gas pressure was anticipated. Stages 3 to 7 represent stages of discrete gas injection rate where multiple gas breakthrough events occurred. The gas injection rates employed in the different stages in ASR\_Tau06\_30gGI are shown in Figure 25a.

#### 3.3.2 Results and discussion

Results for the entire duration of the fault-valve behaviour test (ASR\_Tau06\_30gGI) are presented in Figure 25. Detailed descriptions of the results from each stage of the experiment are given below.

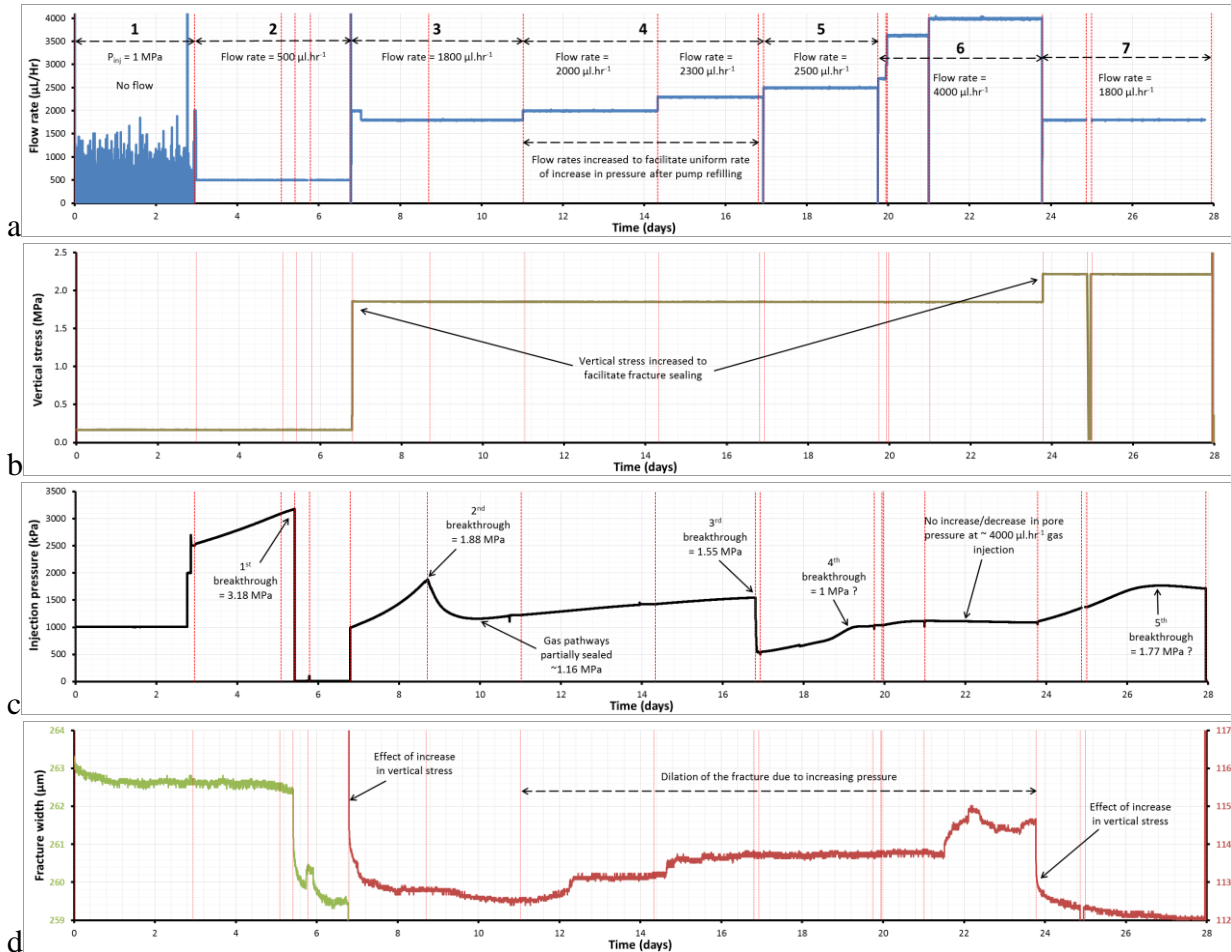


**Figure 25** - Results from the fault-valve behaviour test (ASR\_Tau06\_30gGI). a) Flow rate; b) Vertical stress; c) Gas injection pressure; d) Fracture width.

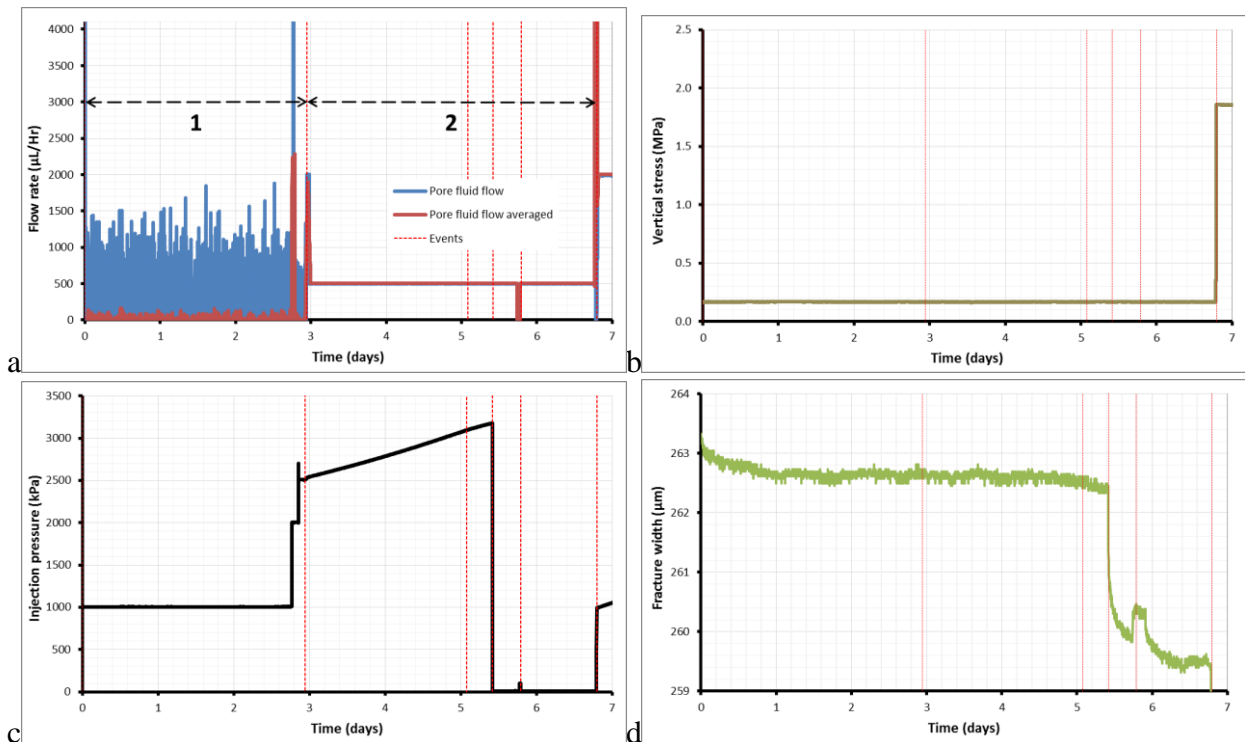


**Figure 26** – Stage 1 – 2 of the fault-valve behaviour test (ASR\_Tau06\_30gGI). a) Flow rate. In stage 1, no flow was detected. Stage 2 was conducted as a constant flow gas injection test; b) Vertical stress; c) Injection pressure; d) Fracture width showing an abrupt decrease in gouge thickness after the gas breakthrough event.

In stage 1 the gas injection pressure was maintained constant at 1 MPa and resulting flow of gas through the slip plane was monitored. No flow of gas was detected and hence it was concluded that gas injection pressure had to be increased so as to achieve gas entry and subsequent gas flow. Vertical stress was maintained constant at 0.17 MPa and the thickness of the gouge material was 262.6 microns. Maintaining the vertical stress at 0.17 MPa, stage 2 was commenced by increasing the gas injection pressure to 2.5 MPa followed by a constant gas injection rate of  $500 \mu\text{l.h}^{-1}$ . The constant gas injection rate resulted in an increase in gas pressure from 2.5 MPa at day 2.9 to 3.18 MPa at day 5.4. Subsequently gas entry and breakthrough occurred and the gas pressure dropped from 3.18 MPa to 0 MPa. The gas breakthrough event was associated with removal of gouge material from the slip plane as displayed by the abrupt decrease in gouge thickness from 262.6 microns to 260.7 microns during the gas breakthrough event. Flow rate was kept constant for an additional period of time (from day 5.4 to day 6.8) to test whether the formed gas pathway(s) had self-sealed. The gouge could not sustain any pressure and showed that the pathway(s) had not self-sealed and was still conductive. Subsequently it was decided to increase the vertical stress so as to facilitate sealing.

Stage 3 started at Day 6.8 with an injection rate at  $2000 \mu\text{l.h}^{-1}$  (Figure 27). However, at day 7 the gas injection rate was reduced from  $2000 \mu\text{l.h}^{-1}$  to  $1800 \mu\text{l.h}^{-1}$ . The gas pressure increased gradually with gas injection from 1 MPa at day 6.8 to 1.84 MPa at day 8.7. Gas breakthrough occurred at day 8.7 and as a result gas pressure dropped from 1.84 MPa to 1.16 MPa. Constant gas injection rate of  $1800 \mu\text{l.h}^{-1}$  was maintained in stage 3 after gas breakthrough to test the sealing of the gas pathway(s) (Figure 27). By Day 10 the pressure reduction had stabilised and resulted in a slow increase in gas pressure. An increase in gas pressure will be observed when the rate of injection of gas into the system is greater than the rate at which the gas escapes through the gas pathways. The gradual sealing of the gas pathways can be deciphered easily from the gas pressure versus time curve in Figure 27c. After the gas breakthrough event new gas flow pathways formed and the rate of gas escaping through the pathways was more than the gas being injected into the slip plane. As the gas pathways gradually sealed the rate of decline in gas pressure decreased up until between days 9.8 and 10 when no decrease or increase in gas pressure was observed. The steady state in gas pressure between days 9.8 and 10 marks the stage when the rate of gas injection was equal to the rate of gas leakage. With time, the gas pathway(s) exhibited improved sealing and the gas pressure started to increase with continued gas injection. The thickness of the gouge (fracture width) remained constant at 113 microns after the gas breakthrough event which suggests that the gas breakthrough event between stage 3 and 4 might have occurred as a result of the reopening of the pre-existing gas pathway(s) which formed during the first gas breakthrough event reported in stage 2 (Figure 26c).

Stage 4 was conducted with a continuous gas injection at a rate of  $2000 \mu\text{l.h}^{-1}$  resulting in a steady rate of increase in gas pressure from day 11 to 14 until steady state gas pressure was observed between day 13.89 and 14.33 (Figure 28). The gas injection rate was increased from  $2000 \mu\text{l.h}^{-1}$  to  $2300 \mu\text{l.h}^{-1}$  and led to a steady increase in gas pressure until the third breakthrough event occurred at day 16.8 at a gas pressure of 1.54 MPa. After the breakthrough event, gas pressure dropped to 0.57 MPa. In stage 5, the water-gas interface vessel was refilled with 200cc of helium gas at 0.57 MPa and the constant gas injection rate experiment was resumed at an injection rate of  $2500 \mu\text{l.h}^{-1}$ . With continued gas injection the gas pressure increased from 0.57 MPa to 1.0 MPa. The inhomogeneous evolution of the gas flow-pathways can be deciphered from the variation in slope of the gas pressure curve in Figure 28c. An obvious variation in slope was observed at day 18.6 indicating that the pathways had undergone some kind of modification which has resulted in enhanced sealing. The fourth gas breakthrough event occurred at a gas pressure of 1.0 MPa. Moreover, after the gas breakthrough event the gas pressure remained more or less steady at 1.0 MPa indicating that the breakthrough event was associated with the gradual opening of the pre-existing gas pathways. With continuous gas injection, fracture width increased from  $112.5 \mu\text{m}$  to  $113.7 \mu\text{m}$ . This increase in fracture width may be due to the minute dilation of the slip plane as a result of the formation of gas pathways and/or due to the heave

resulting from the excess gas pressure at the centre of the slip plane. Following the fourth gas breakthrough event, the flow of gas occurred at a steady rate as observed by no increase in gas pressure irrespective of a gas injection rate of  $2500 \mu\text{l.h}^{-1}$ .

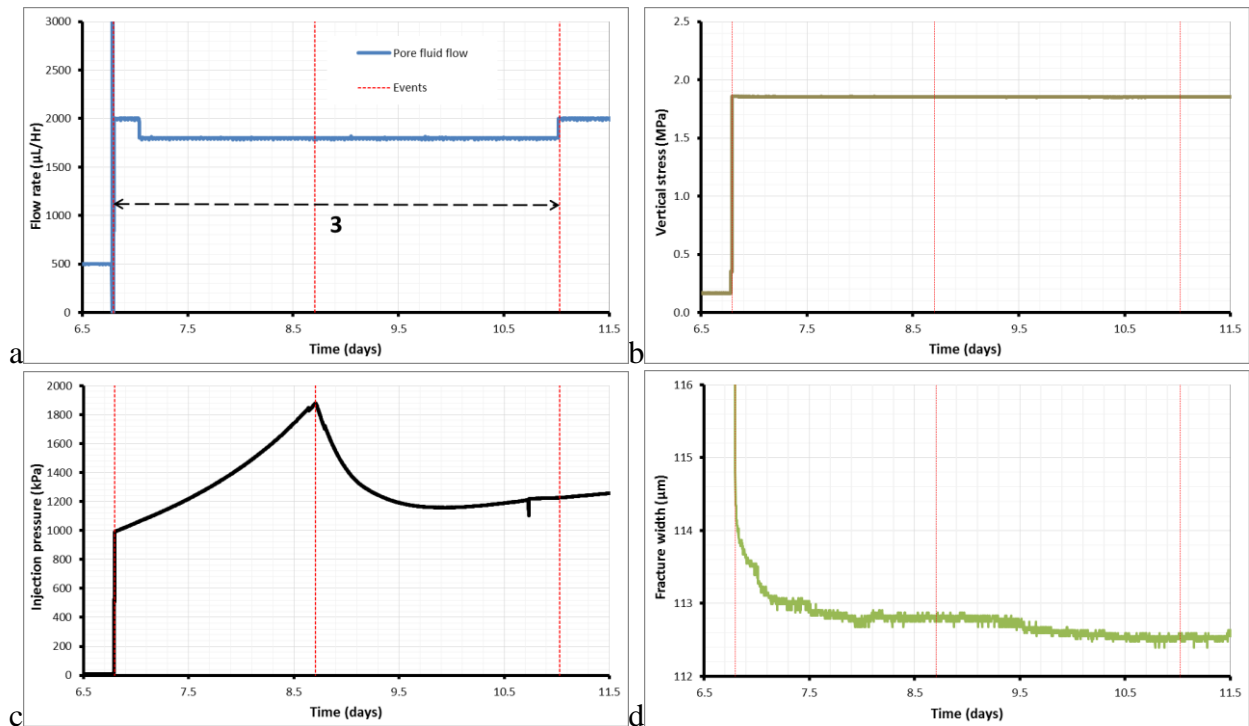


**Figure 27** – Stage 3 of the fault-valve behaviour test (ASR\_Tau06\_30gGI). a) Flow rate; b) Vertical stress. In order to facilitate sealing, the vertical stress was increased from 0.17 MPa to 1.86 MPa at the beginning of stage 3. c) Gas pressure with continuous gas injection at a rate of  $1800 \mu\text{l.h}^{-1}$ ; d) Fracture width.

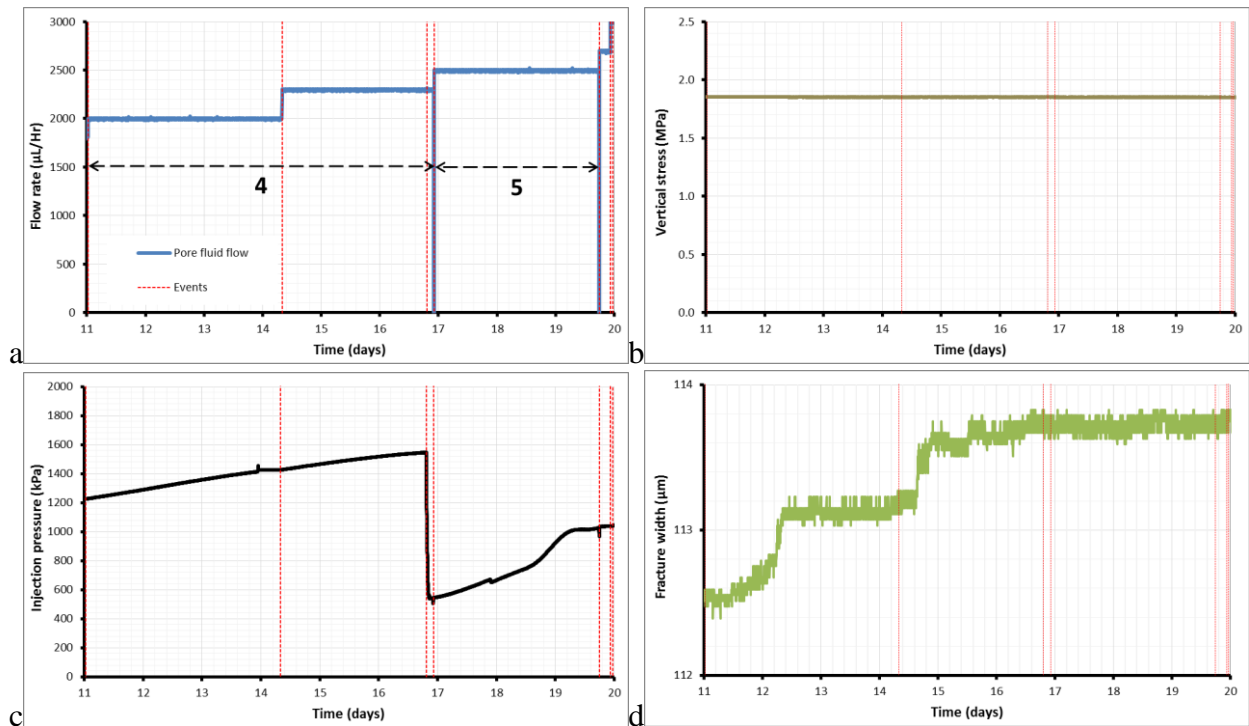


**Figure 28** - Stage 4 – 5 of the fault-valve behaviour test (ASR\_Tau06\_30gGI). a) Flow rate; b) Vertical stress; c) Gas pressure; d) Fracture width.

The gas injection rate was increased to  $4000 \mu\text{l.h}^{-1}$  in stage 6. This increase in gas injection rate resulted in only a trivial increase in gas pressure as the gas flow through the pathways remained

under steady state from day 21 to day 24 (Figure 29). An increase in fracture width from 113.6  $\mu\text{m}$  to 115  $\mu\text{m}$  was observed suggesting that the gas flow was accompanied by dilation of the gouge. In stage 7 the vertical stress was increased from 1.8 MPa to 2.2 MPa to facilitate sealing of the fractures. An abrupt decrease in fracture width from 114.6  $\mu\text{m}$  to 112.8  $\mu\text{m}$  resulted and the flow rate was reduced to 1800  $\mu\text{l}\cdot\text{h}^{-1}$ . The gas pressure increased at a steady rate until the fifth gas breakthrough event occurred at a pressure of 1.77 MPa at day 26.4.

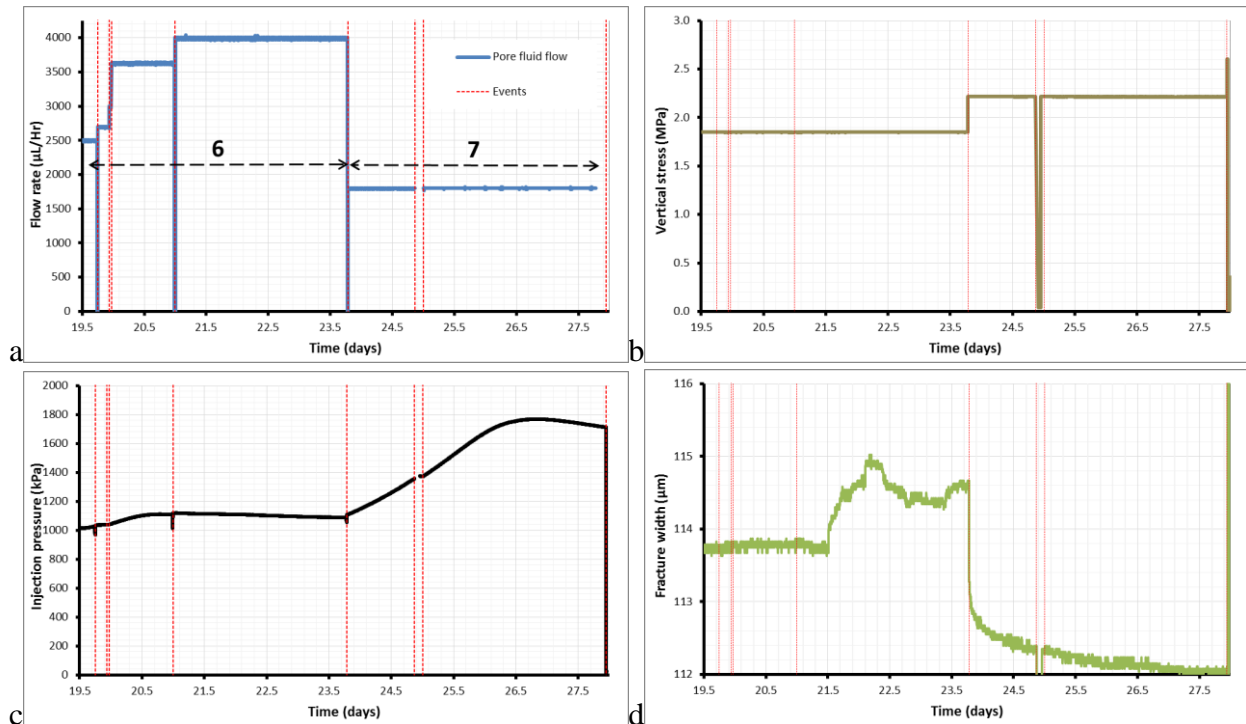


**Figure 29** – Stage 6 – 7 of the fault-valve behaviour test (ASR\_Tau06\_30gGI). a) Flow rate; b) Vertical stress; c) Gas pressure; d) Fracture width.

### 3.3.3 Conclusions

The results from the seven stages of the ASR\_Tau06\_30gGI experiment demonstrate the fault valve behaviour associated with the flow of fluids (gases and water) through fractures under natural conditions. The first gas breakthrough event was associated with the formation of the gas pathways and associated expulsion of gouge material from the experimental slip plane. No significant variations in pore pressures were observed within the slip plane throughout the full duration of the experiment (Figure 30) suggesting that the gas migration occurred via localised channels formed as a result of dilation of the kaolinite clay gouge.

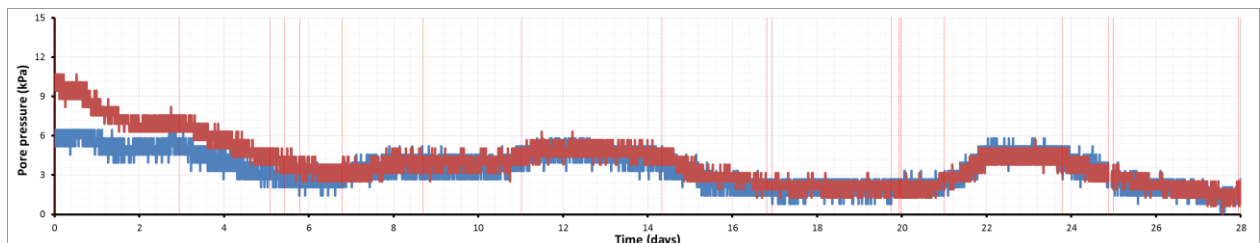


**Figure 30** – Evolution of pore pressure within the slip plane during the fault-valve behaviour test (ASR\_Tau06\_30gGI). No significant increase in pore pressure was observed.

The pressure at which gas breakthrough occurred decreased with each subsequent gas breakthrough event. This decrease in gas breakthrough pressure suggests that each gas

breakthrough event occurs via the opening and closing of the pre-existing gas pathway(s). An increase in vertical stress has been observed to facilitate the sealing of the flow pathways. The results suggests that a close relationship exists between the vertical stress acting on the slip plane, gas injection rate and the gas breakthrough pressures observed. An increase in vertical stress or an increase in gas injection rate results in higher breakthrough pressures. In exceptional circumstances, steady state flow may be achieved when the rate of gas inflow equals the rate of gas outflow from the fracture plane as observed in stage 6 following the fourth gas breakthrough event. The occurrence of natural fractures with steady state flow is likely provided constant gas generation rates can be achieved either by the maturation of kerogens in an oil reservoir or as a result of various chemical processes (corrosion, radiolysis etc.) occurring within a radioactive waste repository.

## 4 The effect of slip-plane orientations on gas flow through gouge-filled fractures.

A series of experiments were performed to understand the effect of different slip plane orientations on gas entry/breakthrough and subsequent gas flow. Gas injection experiments were performed at a constant injection rate on experimental slip planes with orientations of 0°, 15°, 30°, and 45° with respect to maximum horizontal stress  $\sigma_{Hmax}$  direction.

### 4.1 EXPERIMENTAL METHODOLOGY

Kaolinite paste was prepared following the methodology elaborated in Section 2.2. The paste was uniformly smeared on the surface of the top block and the top block was aligned over the bottom block. The axial loading system was engaged using a hydraulic jack connected to a syringe pump set at a pressure of 10 MPa. This imparted a constant vertical stress on the slip plane, the magnitude of which was determined by the orientation of the slip plane with respect to horizontal as shown in Table 7. The gas injection system was fitted with a water-gas interface vessel as mentioned in Section 2.3.2. During the gas injection experiments, the volume of gas in the interface vessel at the beginning of the experiment was maintained at a constant volume of 200 cc at 4 MPa gas pressure. The experiment was commenced by the injection of water into the interface vessel at a constant rate of 700  $\mu\text{l}\cdot\text{h}^{-1}$ . As a result, the pressure of the helium gas within the interface vessel gradually increased until gas pressure reached the gas breakthrough pressure and gas entered the gouge filled slip plane. The evolution of gas pressure with constant injection of water was predicted using the Boyles law and the number of moles of gas entering the slip plane was estimated using the ideal gas law.

Slip plane orientation (degrees)	Pressure on Hydraulic jack (MPa)	Normal stress on the slip plane (MPa)
0	10	2.13
15	10	2.06
30	10	1.84
45	10	1.50

**Table 7** – The normal stress acting on the experimental slip plane at different orientations. The normal stress decreases as the slip plane orientation increases.

A total of 22 gas-injection experiments were conducted, as shown in Table 8. Due to repeatability issues, a minimum of three tests were conducted at each angle. Due to time limitations, it was not possible to perform multiple testing at different fracture angles during active shearing.

	Experiment	Start date	Slip-plane orientation	Gas Injection test number
2	ASR_Tau09_30gGI	27-Sep-11	30°	1
4	ASR_Tau11_30gGI	11-Oct-11		2
5	ASR_Tau12_30gGI	09-Nov-11		3
6	ASR_Tau13_30gGI	18-Nov-11		4
9	ASR_Tau15_00gGI	14-Feb-12	0°	5
10	ASR_Tau16_00gGI	23-Feb-12		6
11	ASR_Tau17_00gGI	05-Mar-12		7
12	ASR_Tau18_15gGI	22-Mar-12	15°	8
13	ASR_Tau19_15gGI	03-Apr-12		9
14	ASR_Tau20_15gGI	18-Apr-12	0°	10
15	ASR_Tau21_00gGI	01-May-12		11
16	ASR_Tau22_00gGI	14-May-12		12
17	ASR_Tau23_00gGI	28-May-12		13
18	ASR_Tau24_00gGI	06-Jun-12		14
19	ASR_Tau25_45gGI	19-Jun-12	45°	15
20	ASR_Tau26_45gGI	03-Jul-12		16
40	ASR_Tau27_45gGI	13-Jul-12	0°	17
41	ASR_Tau28_00gGIS	25-Jul-12		18
42	ASR_Tau29_00gGIS	06-Aug-12		19
44	ASR_Tau30_30gGIS	29-Aug-12	30°	20
45	ASR_Tau31_45gGIS	10-Sep-12	45°	21
46	ASR_Tau32_15gGIS	25-Sep-12	15°	22

**Table 8** – List of gas-injection experiments conducted.

The following sections are discussed in terms of similar test protocols, i.e. for each fracture angle, as opposed to chronological order. As all tests were conducted as close to identical conditions as possible no influence of time was seen in the test results.

## 4.2 GAS BREAKTHROUGH EXPERIMENTS ON A SLIP PLANE ORIENTATION OF 0°

A total of five gas injection experiments were conducted on a flat slip plane, i.e. at an orientation of 0° with respect to the slip direction. As stated previously, each test was performed as identical as possible, with identical water content of gouge produced, similar vertical load, similar volumes of gas, and identical gas injection rates. The only parameter that is likely to have varied between tests was the thickness of the gouge at the start of the experiment. However, as best as could be established, this did not vary significantly between tests as the gouge became very thin in all tests.

### 4.2.1 Test ASR\_Tau15\_00gGI (Gas test 5)

Test ASR\_Tau15\_00gGI was the fifth gas injection test conducted and was performed on a fracture oriented 0° to the slip plane direction. The results of the test are summarised in Figure 31. As can be seen in Figure 31a, the gas injection experiment resulted in a maximum gas pressure of approximately 8 MPa, although peak pressure was not achieved due to limited volumes of helium. In the early stages of the test, the fracture could be seen to compress (Figure 31c). However, the capacitance sensor used to measure vertical movement of the apparatus malfunctioned at about Day 1.8. The dilation data is viewed as secondary to the main objectives of the experiment and therefore the test was continued. A secondary measurement system also gives information about the fracture thickness (Figure 31d). A pair of fracture width eddy current sensors similarly showed that the fracture compressed. At the time when the capacitance sensor failed, the fracture width sensors show that the fracture began to dilate; this corresponded with the onset of pressure deviation from the ideal gas law prediction and is likely to signify gas entry. Approximately Day 2.8, the fracture width sensors also malfunctioned.

Figure 31b shows the difference between the gas pressure observed and the predicted pressure from the ideal gas law. As seen, this data suggests that gas started to enter the fracture at around Day 2.2 when the gas pressure was 4,770 kPa. Figure 31e shows the average flow at STP into the fracture, with gas entry inferred to be approximately 5,000 kPa. Both methods used to predict gas entry gave similar results.

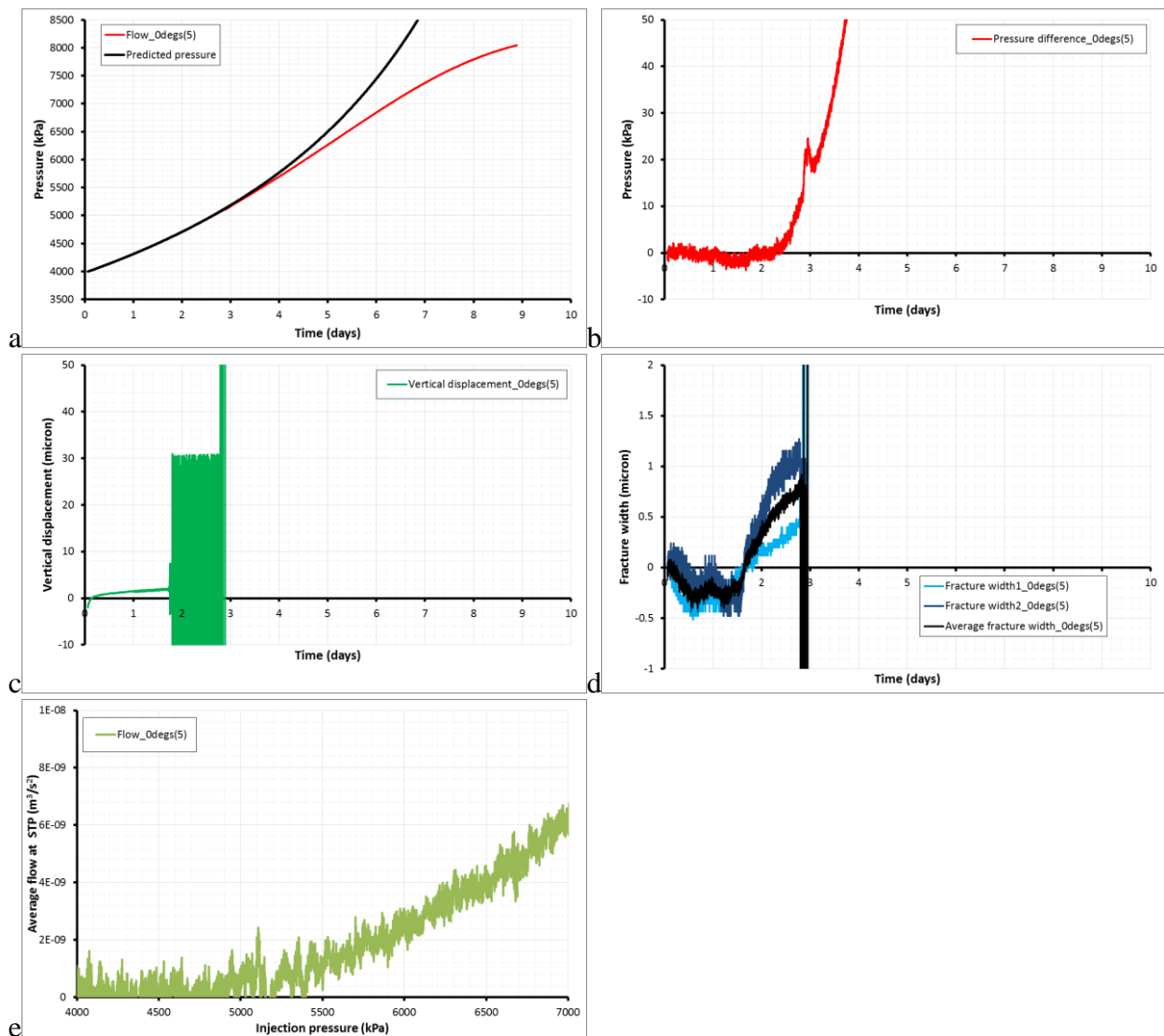


**Figure 31** – Results for gas injection test 5 / ASR\_Tau15\_00gGI. a) Gas injection pressure compared with prediction from ideal gas law; b) comparison of gas injection and ideal gas law as a way of predicting gas entry pressure; c) normal displacement [note malfunctioned]; d) fracture width [note malfunctioned]; e) flow into the slip plane as a way of predicting gas entry pressure.

#### 4.2.2 Test ASR\_Tau16\_00gGI (Gas test 6)

The second test conducted on a fracture oriented  $0^\circ$  to the slip-plane was ASR\_Tau16\_00gGI; the sixth gas injection test conducted. The results of the test are summarised in Figure 32. As can be seen in Figure 32a, the gas injection experiment resulted in a maximum gas pressure of approximately 17.5 MPa, although peak pressure was not achieved due to limited volumes of helium. This was significantly higher than the gas pressure seen in test ASR\_Tau15\_00gGI. In the early stages of the test, the fracture could be seen to compress approximately 20  $\mu\text{m}$  (Figure 32c), much more than in the previous test. The compression can be seen to be non-uniform, with minor dilational events seen at Day 1 and Day 3.5. At Day 5 the sensor showed significant dilation. The pair of eddy current fracture width sensors showed a complex history (Figure 32d). One sensor shows simple compression throughout the test history. The other showed much

greater compression, with significant dilation events; one of these clearly corresponded with the dilation seen in the normal displacement and the other corresponds with a minor normal load dilational event. One eddy current sensor was mounted either end of the top-block, therefore the data suggest that only one end of the fracture was significantly compressing or dilating.

Figure 32b shows the difference between the gas pressure observed and the predicted pressure from the ideal gas law. As seen, this data suggests that gas started to enter the fracture at around Day 1.8 when the gas pressure was 4,600 kPa. Figure 32e shows the average flow at STP into the fracture, with gas entry inferred to be approximately 7,000 kPa. In contrast to test ASR\_Tau15\_00gGI, the methods used to predict gas entry gave dissimilar results.

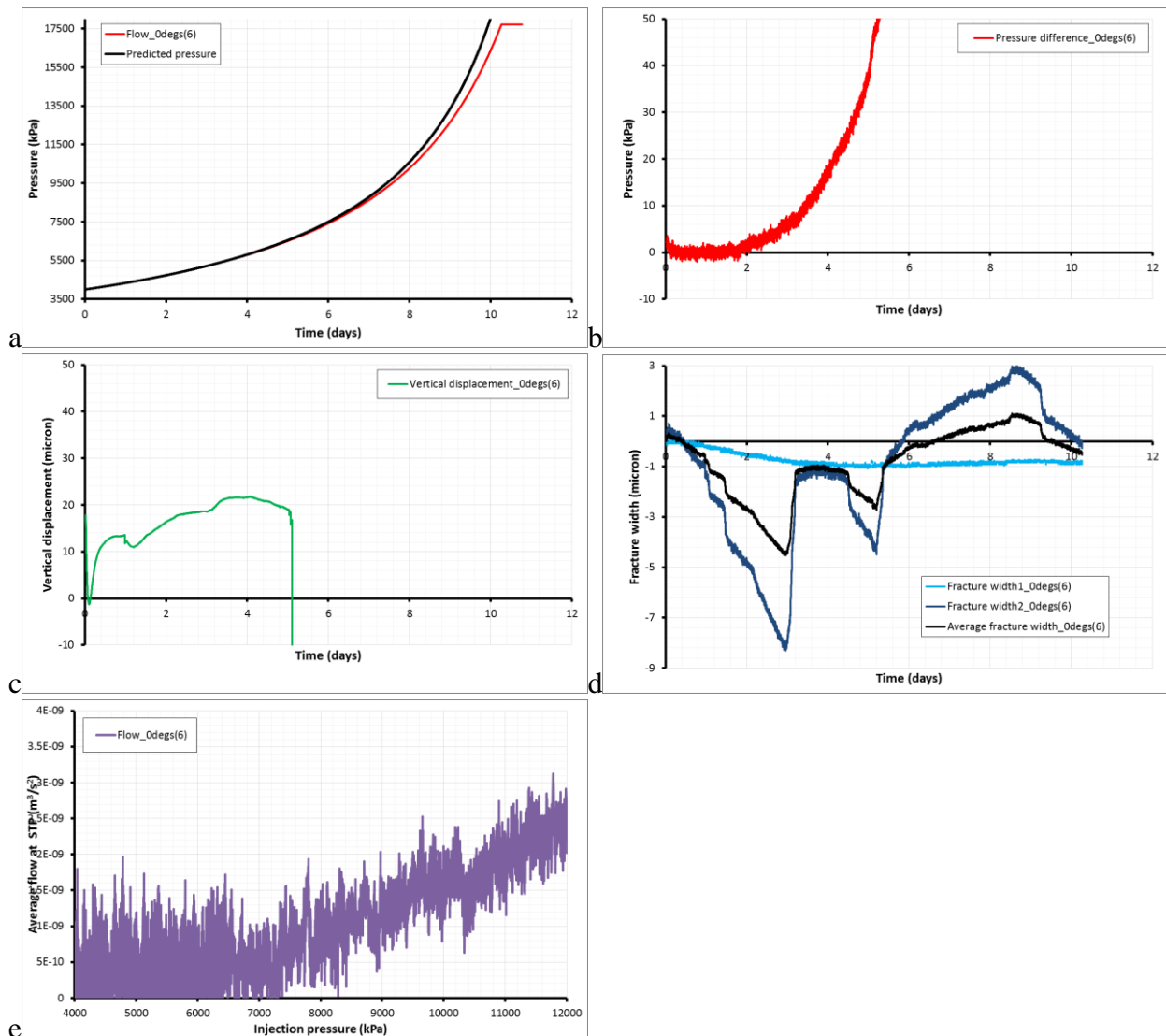


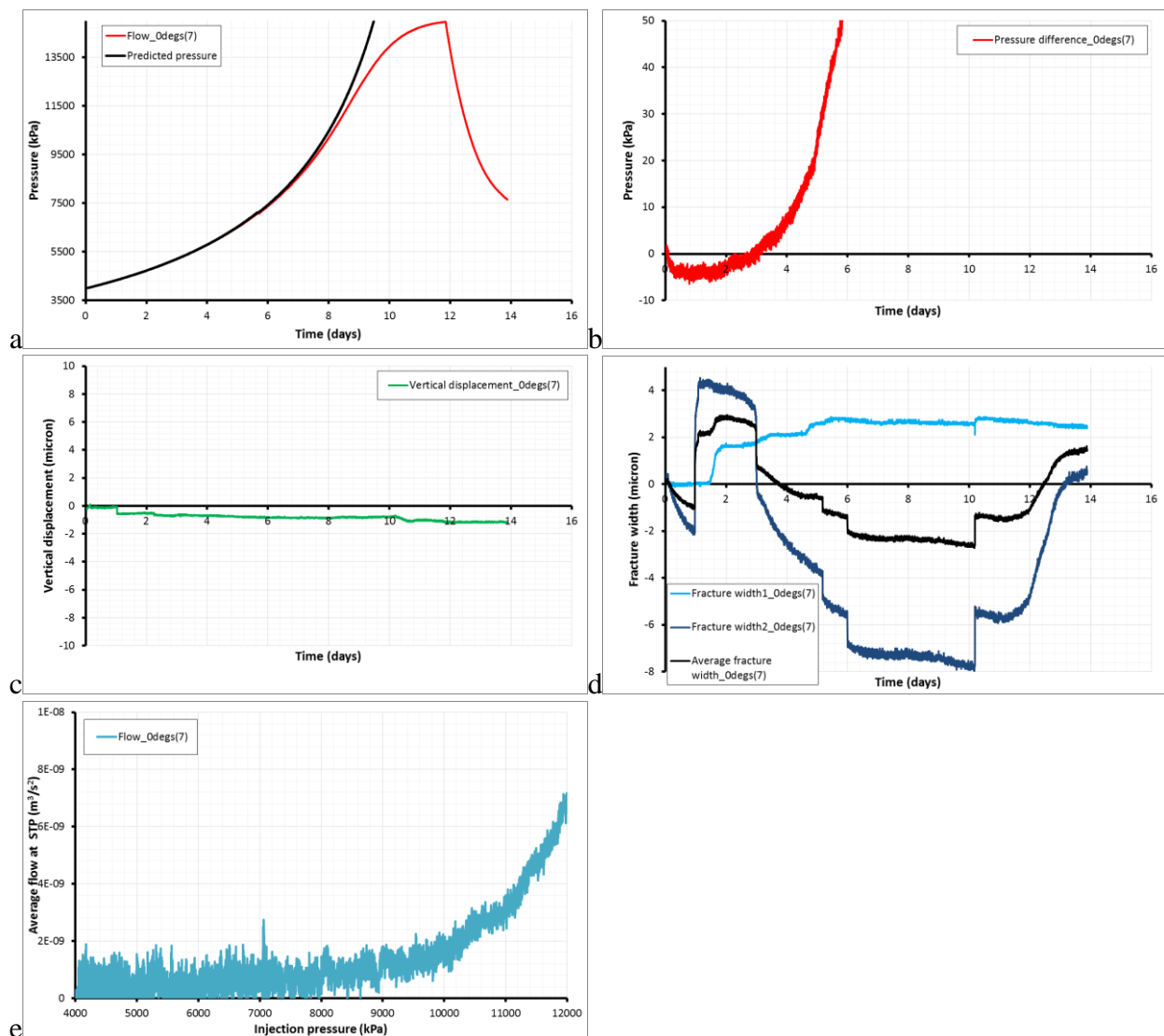
**Figure 32** – Results for gas injection test 6 / ASR\_Tau16\_00gGI. a) Gas injection pressure compared with prediction from ideal gas law; b) comparison of gas injection and ideal gas law as a way of predicting gas entry pressure; c) normal displacement; d) fracture width; e) flow into the slip plane as a way of predicting gas entry pressure.

#### 4.2.3 Test ASR\_Tau17\_00gGI (Gas test 7)

The third test conducted on a fracture oriented  $0^\circ$  to the slip-plane was test ASR\_Tau17\_00gGI; the seventh gas injection test conducted. The results of the test are summarised in Figure 33. As can be seen in Figure 33a, the gas injection experiment resulted in a maximum gas pressure of approximately 14.5 MPa, with peak pressure nearly achieved. Following the cessation of gas injection on Day 12, a gas shut-in stage was conducted for two days. An asymptote of pressure

would have taken a significant amount of time and so the experiment was halted. Throughout the test history the fracture could be seen to dilate by only 1  $\mu\text{m}$  (Figure 33c). The eddy current sensors showed a complex history (Figure 33d). One sensor showed no change for 1.5 days, followed by dilation throughout the remaining test history. The other showed much greater changes in fracture width, with significant compression and dilation events. One eddy current sensor was mounted either end of the top-block, therefore the data suggest that the fracture width was not constant throughout the test history. It should be noted that the same sensor was showing complex behaviour as in test ASR\_Tau16\_00gGI. This may suggest that the sensor was behaving in a non-ideal way.

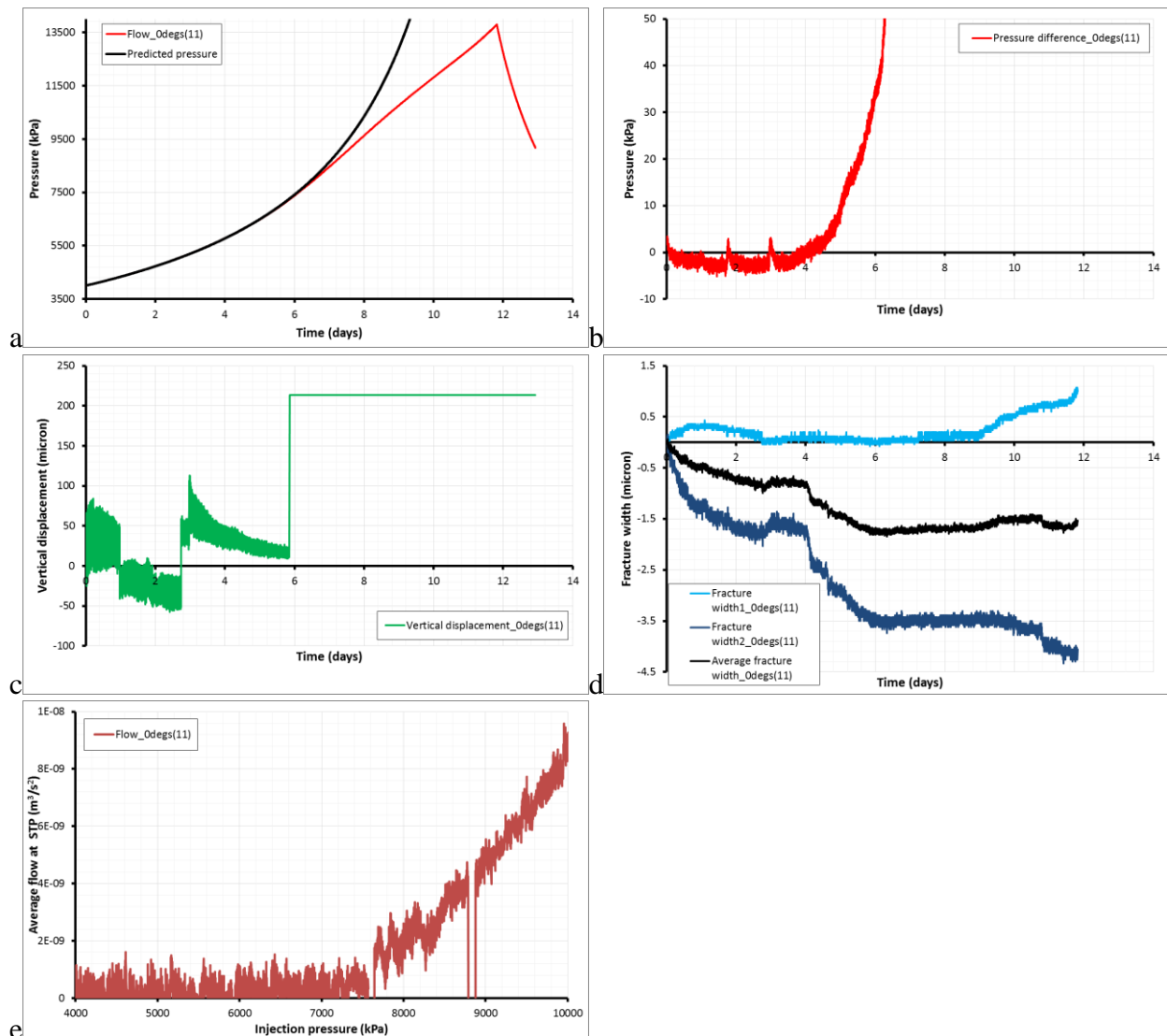
Figure 33b shows the difference between the gas pressure observed and the predicted pressure from the ideal gas law. As seen, this data suggested that gas started to enter the fracture at around Day 2 when the gas pressure was 4,590 kPa. Figure 33e shows the average flow at STP into the fracture, with gas entry inferred to be approximately 8,000 kPa. In contrast to test ASR\_Tau15\_00gGI, the methods used to predict gas entry gave significantly dissimilar results.



**Figure 33** – Results for gas injection test 7 / ASR\_Tau17\_00gGI. a) Gas injection pressure compared with prediction from ideal gas law; b) comparison of gas injection and ideal gas law as a way of predicting gas entry pressure; c) normal displacement; d) fracture width; e) flow into the slip plane as a way of predicting gas entry pressure.

#### 4.2.4 Test ASR\_Tau21\_00gGI (Gas test 11)

The fourth test conducted on a fracture oriented  $0^\circ$  to the slip-plane was test ASR\_Tau21\_00gGI; the eleventh gas injection test conducted. The results of the test are summarised in Figure 34. As can be seen in Figure 34a, the gas injection experiment resulted in a maximum gas pressure of approximately 12.5 MPa, with peak pressure not achieved. Following the cessation of gas injection on Day 12, a gas shut-in stage was conducted for one day. An asymptote of pressure would have taken a significant amount of time and so the experiment was halted. The normal displacement data (Figure 34c) suggested that the induction sensor malfunctioned. The eddy current sensors showed a complex history (Figure 34d). One sensor shows minor dilation of approximately  $1 \mu\text{m}$ , whilst the other shows compression of  $1 \mu\text{m}$ . It can be seen that a compressional event corresponds with the onset of gas flow inferred from the ideal gas law (Figure 34b). The data suggest that the top-block was “rocking” about the central loading point.



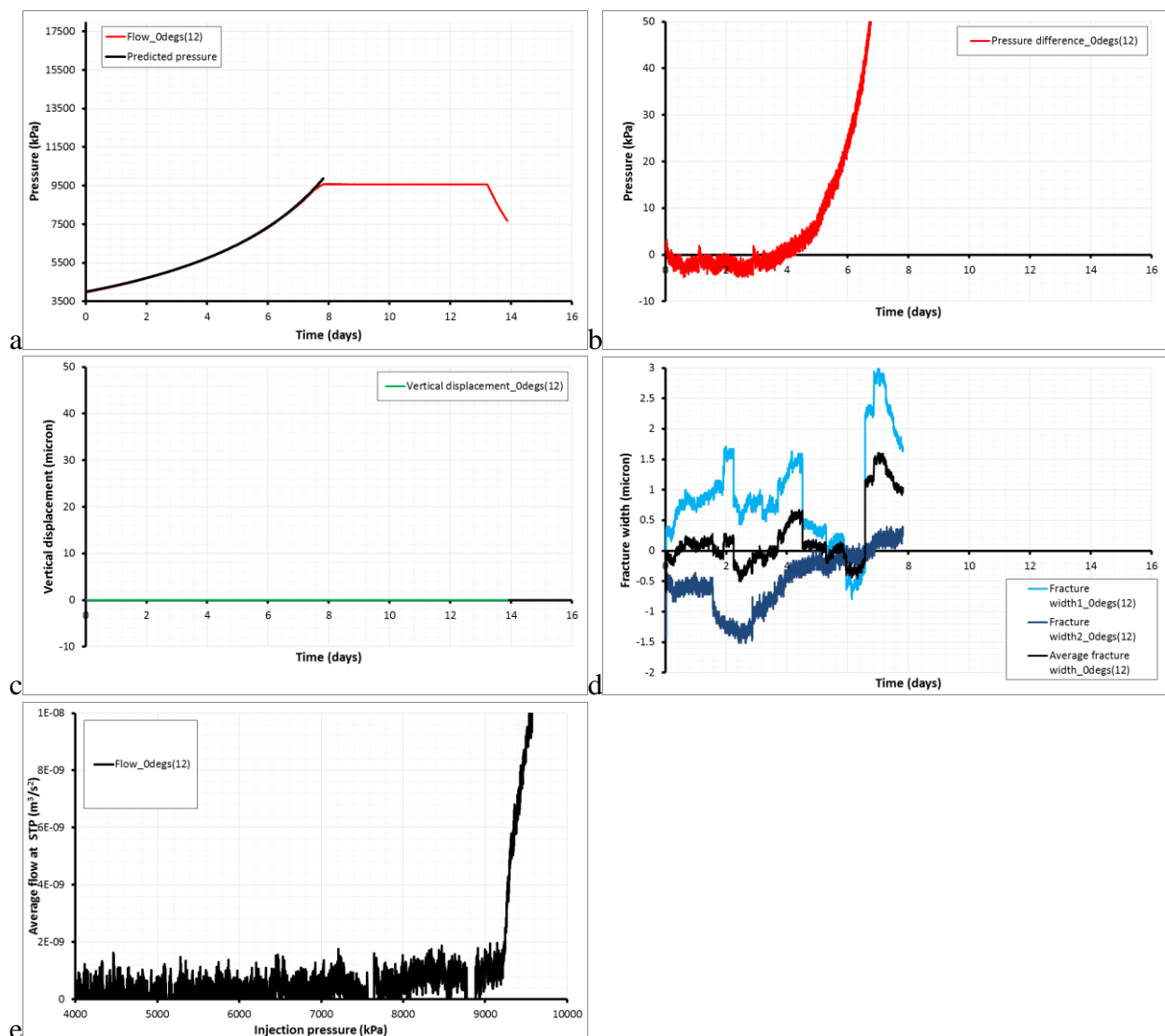
**Figure 34** – Results for gas injection test 11 / ASR\_Tau21\_00gGI. a) Gas injection pressure compared with prediction from ideal gas law; b) comparison of gas injection and ideal gas law as a way of predicting gas entry pressure; c) normal displacement [note malfunctioned]; d) fracture width; e) flow into the slip plane as a way of predicting gas entry pressure.

Figure 34b shows the difference between the gas pressure observed and the predicted pressure from the ideal gas law. As seen, this data suggested that gas started to enter the fracture at around Day 3.5 when the gas pressure was 5,475 kPa. Figure 34e shows the average flow at STP into the

fracture, with gas entry inferred to be approximately 7,500 kPa. In contrast to test ASR\_Tau15\_00gGI, the methods used to predict gas entry gave dissimilar results.

#### 4.2.5 Test ASR\_Tau22\_00gGI (Gas test 12)

The fifth test conducted on a fracture oriented  $0^\circ$  to the slip-plane was test ASR\_Tau22\_00gGI; the twelfth gas injection test conducted. The results of the test are summarised in Figure 35. As can be seen in Figure 35a, a logging error occurred between Day 7.5 and Day 13.5. This means that it is unclear what maximum pressure was achieved and only data for gas entry can be achieved from this experiment. Throughout the test history the induction sensor measuring normal displacement was not registering any data; therefore this sensor had malfunctioned. The eddy current sensors showed a complex history (Figure 35d). One sensor showed compression, whilst the other showed dilation. However, the sensor showing dilation had considerable numbers of steps within the data, suggesting that some form of malfunction had occurred. It can be seen that the sensor that initially showed compression had a dilational event that corresponded with the onset of gas entry as predicted from the ideal gas law.



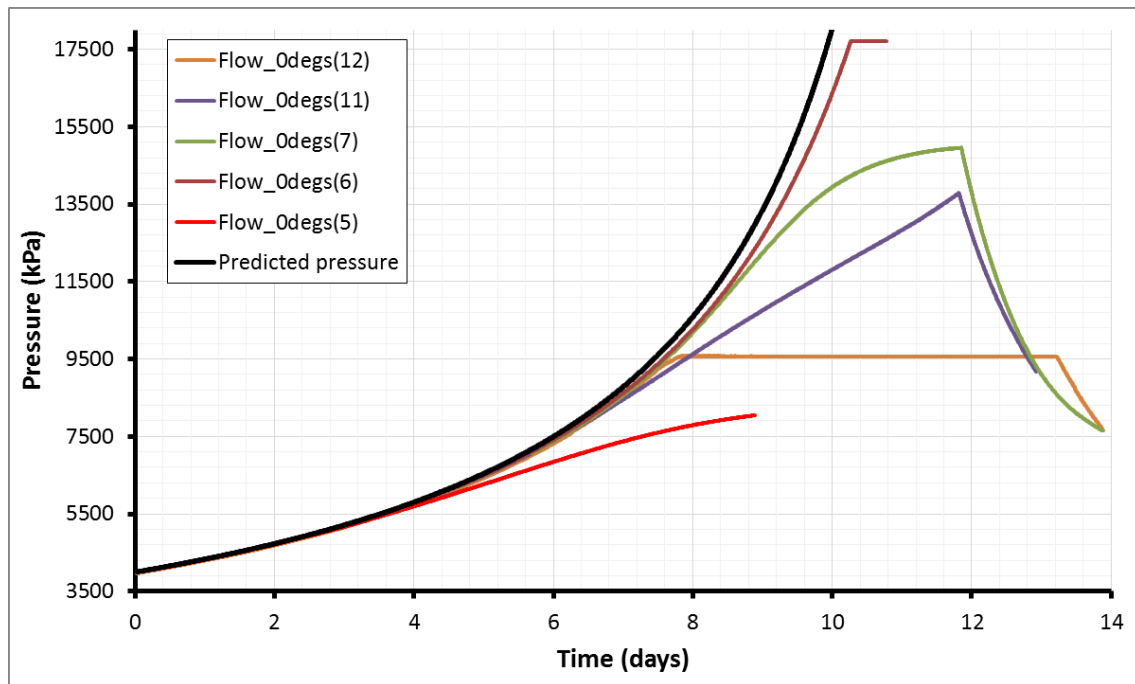
**Figure 35** – Results for gas injection test 12 / ASR\_Tau22\_00gGI. a) Gas injection pressure compared with prediction from ideal gas law; b) comparison of gas injection and ideal gas law as a way of predicting gas entry pressure; c) normal displacement [note malfunctioned]; d) fracture width; e) flow into the slip plane as a way of predicting gas entry pressure.

Figure 35b shows the difference between the gas pressure observed and the predicted pressure from the ideal gas law. As seen, this data suggested that gas started to enter the fracture at around Day 3 when the gas pressure was 5,170 kPa. Figure 35e shows the average flow at STP into the fracture, with gas entry inferred to be approximately 9,250 kPa. In contrast to test ASR\_Tau15\_00gGI, the methods used to predict gas entry gave significantly dissimilar results.

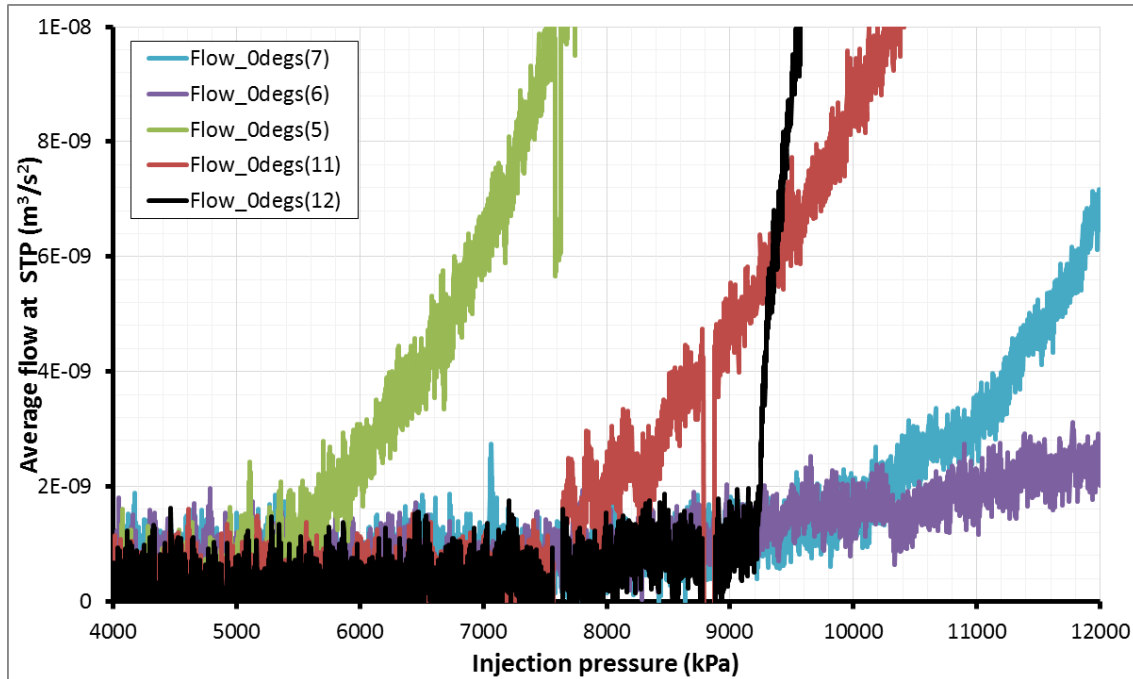
#### 4.2.6 Results for tests conducted in a slip plane orientation of 0°

Figure 36 shows the gas pressure for all five of the gas injection tests conducted on a fracture oriented 0° to the slip-direction. As clearly seen, there is little repeatability in the gas pressures achieved with pressures between 8 and 18 MPa achieved. However, close examination of the data showed that gas entry pressure had a much better repeatability. As described above, two methods were employed for estimating the gas entry pressure; the first compared the gas pressure result with the predicted pressure from the ideal gas law and the second calculated average flow at STP into the fracture. All results are summarised in Table 9, with the results from flow into the fracture shown in Figure 37. As seen in Figure 37, four tests showed similar gas entry pressures of between 7.5 and 9 MPa, whilst one test had an anomalously low gas entry pressure of 5 MPa.

The repeatability seen in gas entry pressure and not peak pressure suggests that the physics governing the onset of flow was maintained for all tests; however, once gas started to be mobile the permeability of the kaolinite filled fracture plane was inconsistent, resulting in variations of behaviour post gas entry. This may be due to differences in the number of pathways formed.



**Figure 36** – Results for five gas injection tests conducted on a fracture oriented 0° to the slip plane. As can be seen, considerable differences are seen in peak pressure and form of the curve indicating that fracture transmissivity is not repeatable.



**Figure 37** – Gas entry pressure predicted from the average flow at STP for five gas injection tests conducted on a fracture oriented 0° to the slip plane. As can be seen, repeatable gas entry pressure is seen for four of the five tests, with one test (5) showing a considerably lower gas entry pressure.

Test	Fracture angle	+/-	Method 1			Method 2		
			Gas entry pressure (kPa)	Average entry pressure	+/-	Gas entry pressure (kPa)	Average entry pressure	+/-
0degs(5)	0°	0.5°	5000	8440	413	4772	4920	193
0degs(6)			8000			4610		
0degs(7)			9000			4590		
0degs(11)			7500			5475		
0degs(12)			9250			5170		

**Table 9** – Results for gas entry pressure for the five gas injection experiments conducted on a fracture oriented 0° to the slip-plane. Method 1 = gas entry determined from STP gas flow into the fracture; Method 2 = entry pressure inferred from comparing pressure curve with ideal gas law.

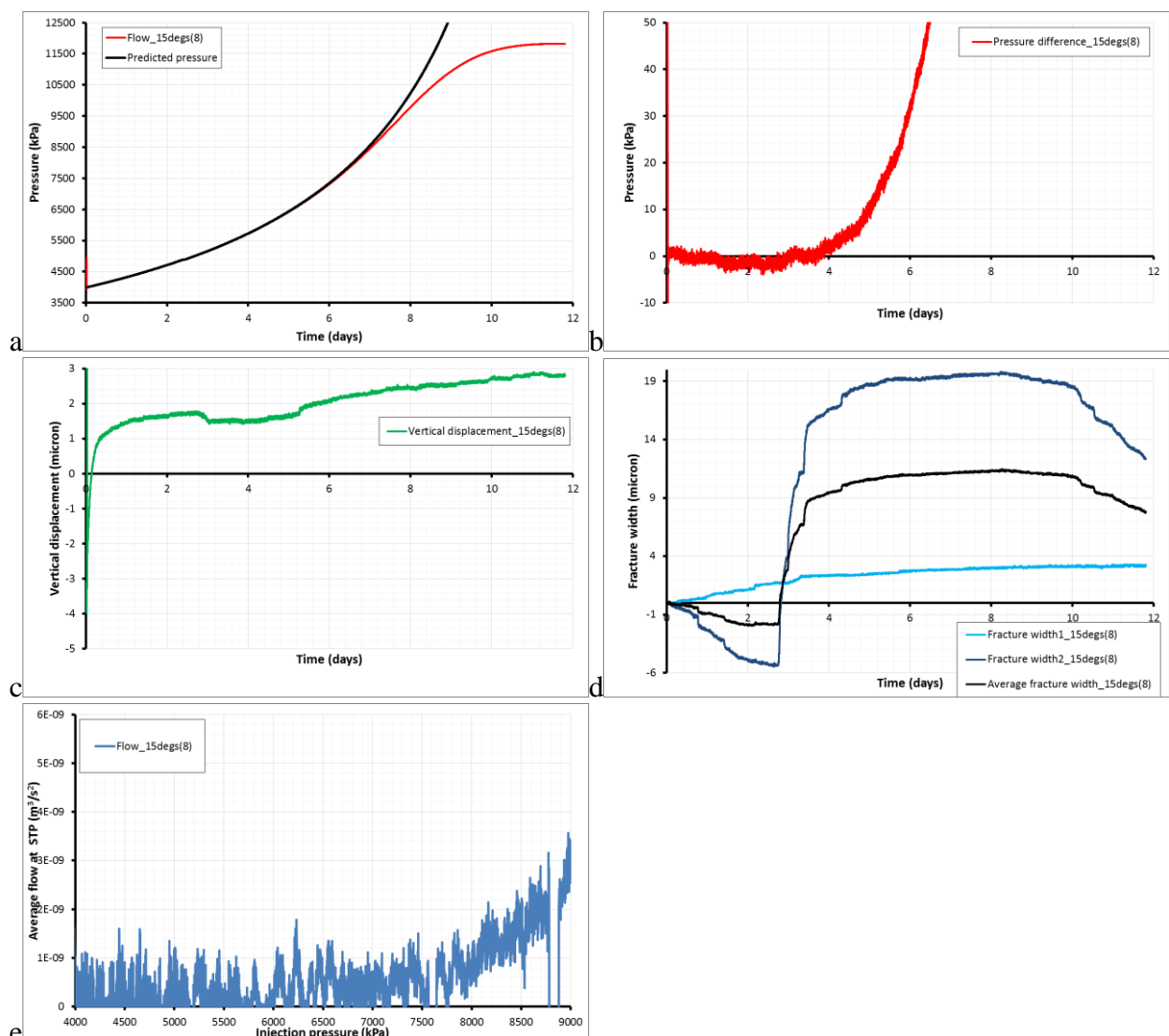
### 4.3 GAS BREAKTHROUGH EXPERIMENTS ON A SLIP PLANE ORIENTATION OF 15°

A total of three gas injection experiments were conducted on a fracture oriented 15° with respect to the slip direction. As stated previously, each test was performed as identical as possible, with identical water content of gouge produced, similar normal load, similar volumes of gas, and identical gas injection rates. The only parameter that was likely to have varied between tests was the thickness of the gouge at the start of the experiment. However, as best as could be established, this did not vary significantly between tests as the gouge became very thin in all tests.

### 4.3.1 Test ASR\_Tau18\_15gGI (Gas test 8)

The first test conducted on a fracture oriented  $15^\circ$  to the slip-plane was test ASR\_Tau18\_15gGI; the eighth gas injection test conducted. The results of the test are summarised in Figure 38. As can be seen in Figure 38a, the gas injection experiment resulted in a maximum gas pressure of approximately 12 MPa, with peak pressure achieved. The normal displacement data (Figure 38c) suggested that the gouge compressed a few micron throughout the test history. The eddy current sensors showed a complex history (Figure 38d). One sensor showed minor dilation of approximately  $2\ \mu\text{m}$ , whilst the other showed compression of  $5\ \mu\text{m}$ , followed by dilation of approximately  $25\ \mu\text{m}$ . It can be seen that the dilational event at approximately Day 3 corresponded with the onset of gas flow inferred from the ideal gas law (Figure 38b).

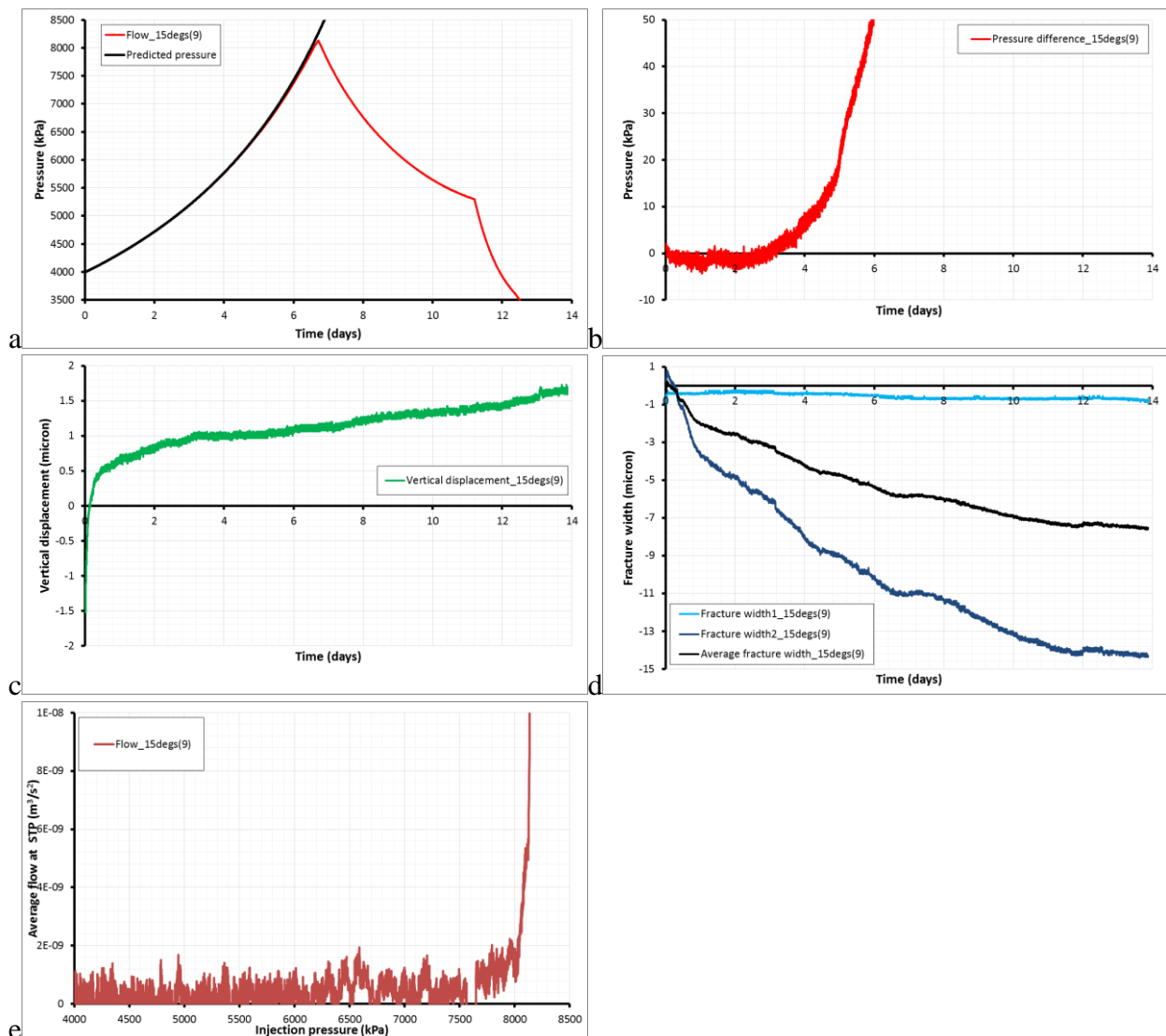
Figure 38b shows the difference between the gas pressure observed and the predicted pressure from the ideal gas law. As seen, this data suggested that gas started to enter the fracture at around Day 3.5 when the gas pressure was 4,850 kPa. Figure 38e shows the average flow at STP into the fracture, with gas entry inferred to be approximately 7,500 kPa. The two methods used for determining gas entry therefore gave significantly dissimilar results.



**Figure 38** – Results for gas injection test 8 / ASR\_Tau18\_15gGI. a) Gas injection pressure compared with prediction from ideal gas law; b) comparison of gas injection and ideal gas law as a way of predicting gas entry pressure; c) normal displacement; d) fracture width; e) flow into the slip plane as a way of predicting gas entry pressure.

### 4.3.2 Test ASR\_Tau19\_15gGI (Gas test 9)

The second test conducted on a fracture oriented  $15^\circ$  to the slip-plane was test ASR\_Tau19\_15gGI; the ninth gas injection test conducted. The results of the test are summarised in Figure 39. As can be seen in Figure 39a, the gas injection experiment resulted in a maximum gas pressure of approximately 8 MPa, with peak pressure achieved and significant decrease in gas pressure post peak. Following the cessation of gas injection on Day 11, a gas shut-in stage was conducted for one day. An asymptote of pressure would have taken a significant amount of time and so the experiment was halted. The normal displacement data (Figure 39c) suggests that fracture compressed throughout the entire test history. Both eddy current sensors showed the fracture was compressing, although one sensor showed a small amount of compression of less than  $1\ \mu\text{m}$  (Figure 39d). The other sensor showed greater compression of  $14\ \mu\text{m}$ . Little correlation is seen between normal displacement or fracture width with the onset of gas entry. No significant change is seen at the peak pressure.



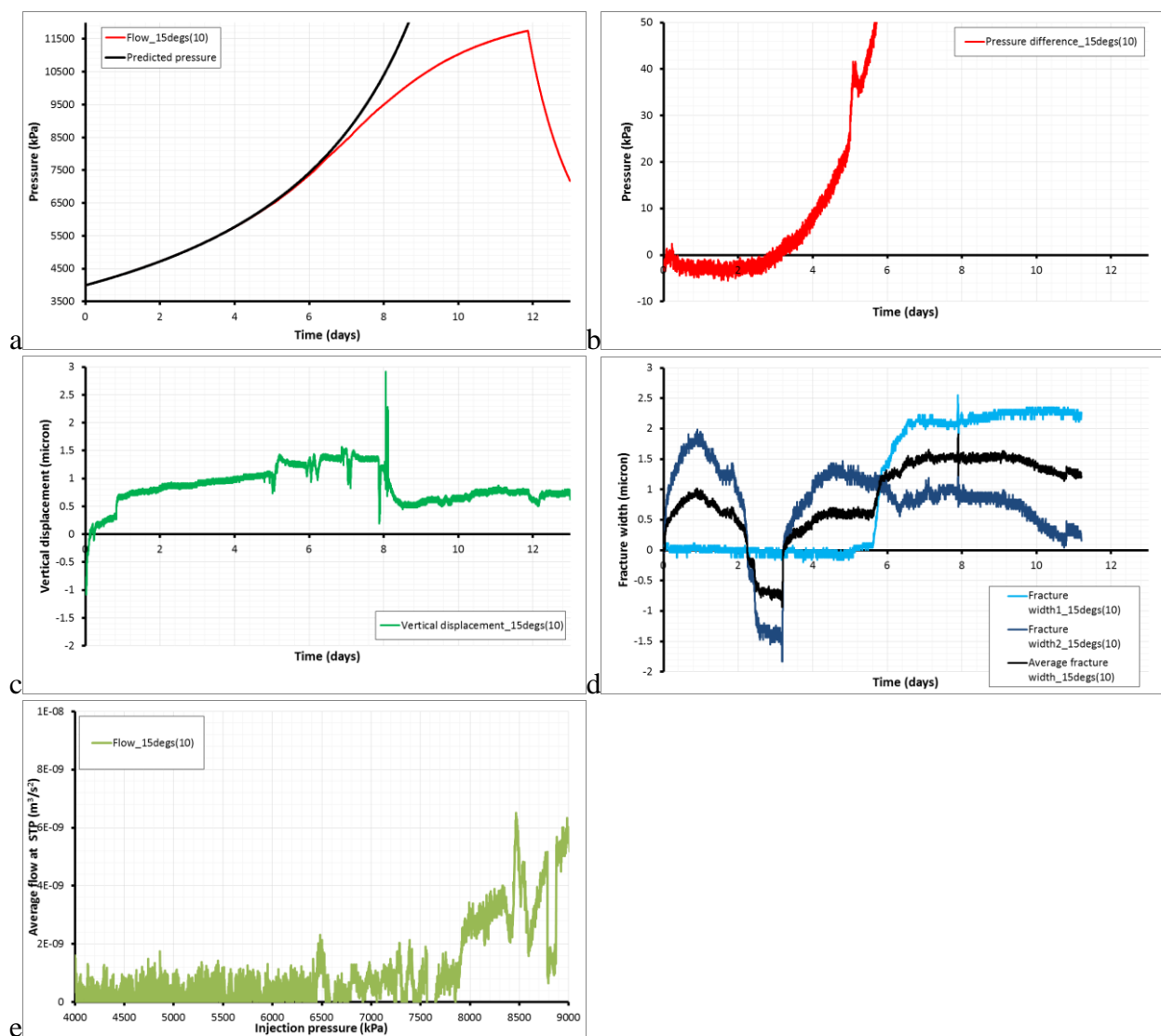
**Figure 39** – Results for gas injection test 9 / ASR\_Tau19\_15gGI. a) Gas injection pressure compared with prediction from ideal gas law; b) comparison of gas injection and ideal gas law as a way of predicting gas entry pressure; c) normal displacement; d) fracture width; e) flow into the slip plane as a way of predicting gas entry pressure.

Figure 39b shows the difference between the gas pressure observed and the predicted pressure from the ideal gas law. As seen, this data suggests that gas started to enter the fracture at around Day 3 when the gas pressure was 4,750 kPa. Figure 39e shows the average flow at STP into the

fracture, with gas entry inferred to be approximately 7,500 kPa. The two methods used for determining gas entry therefore gave significantly dissimilar results.

### 4.3.3 Test ASR\_Tau20\_15gGI (Gas test 10)

The third test conducted on a fracture oriented  $15^\circ$  to the slip-plane was test ASR\_Tau20\_15gGI; the tenth gas injection test conducted. The results of the test are summarised in Figure 40. As can be seen in Figure 40a, the gas injection experiment resulted in a maximum gas pressure of approximately 13 MPa, with peak pressure not achieved. Following the cessation of gas injection on Day 12, a gas shut-in stage was conducted for one day. An asymptote of pressure would have taken a significant amount of time and so the experiment was halted. The normal displacement data (Figure 40c) showed that the fracture compressed throughout the entire test history; although on Day 8 there was evidence for small amounts of dilation. The eddy current sensors showed a complex history (Figure 40d). One sensor showed no variation for over 5 days and then showed dilation of  $2.5 \mu\text{m}$ , whilst the other sensor showed dilation and compression in a complex way. It can be seen that a dilational event corresponds with the onset of gas flow inferred from the ideal gas law (Figure 40b).



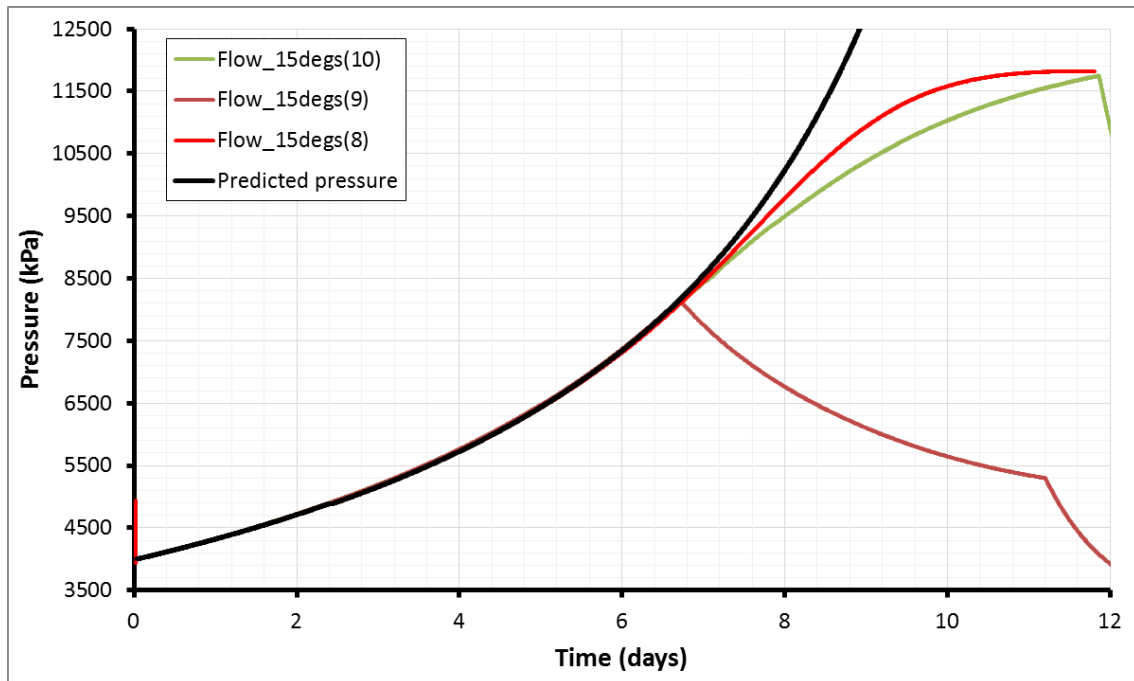
**Figure 40** – Results for gas injection test 10 / ASR\_Tau20\_15gGI. a) Gas injection pressure compared with prediction from ideal gas law; b) comparison of gas injection and ideal gas law as a way of predicting gas entry pressure; c) normal displacement; d) fracture width; e) flow into the slip plane as a way of predicting gas entry pressure.

Figure 40b shows the difference between the gas pressure observed and the predicted pressure from the ideal gas law. As seen, this data suggests that gas started to enter the fracture at around Day 3 when the gas pressure was 4,925 kPa. Figure 40e shows the average flow at STP into the fracture, with gas entry inferred to be approximately 7,750 kPa. The two methods used for determining gas entry therefore gave significantly dissimilar results.

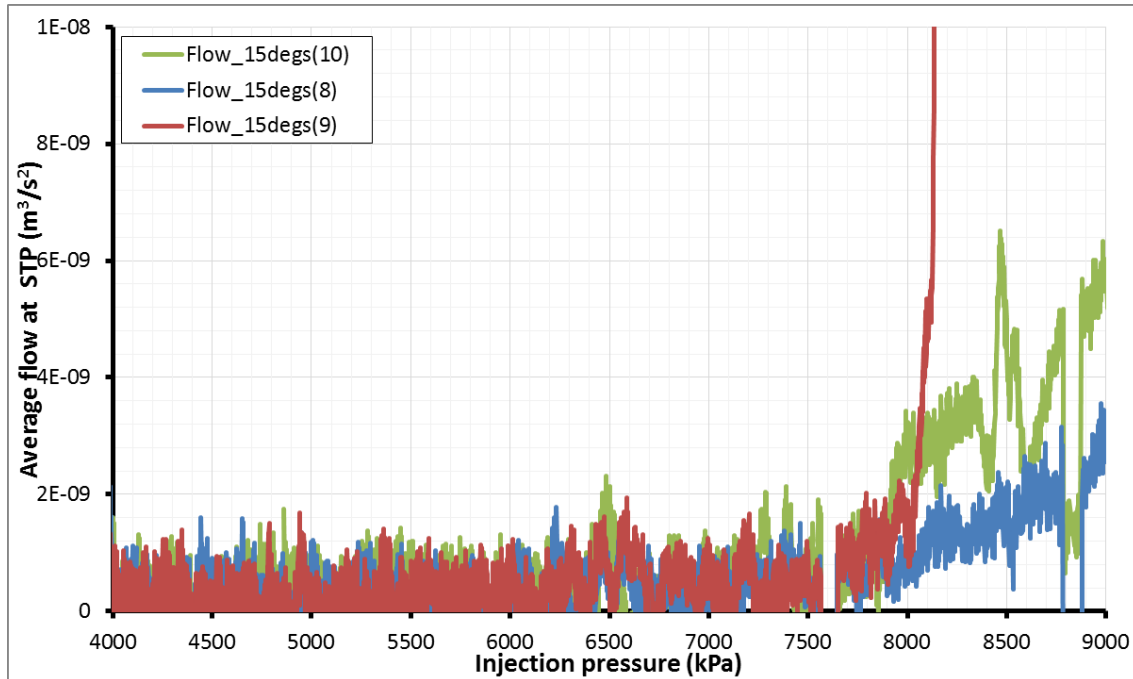
#### 4.3.4 Results for tests conducted in a slip plane orientation of 15°

Figure 41 shows the gas pressure for all three of the gas injection tests conducted on a fracture oriented 15° to the slip-direction. As clearly seen, there is little repeatability in the gas pressures achieved with pressures between 8 and 12 MPa achieved. However, close examination of the data showed that gas entry pressure had a much better repeatability. As described above, two methods were employed for estimating the gas entry pressure; the first compared the gas pressure result with the predicted pressure from the ideal gas law and the second calculated average flow at STP into the fracture. All results are summarised in Table 10, with the results from flow into the fracture shown in Figure 42. As seen in Figure 42, all three tests had gas entry between 7,500 and 7,750 kPa.

As stated previously, the repeatability seen in gas entry pressure and not peak pressure suggests that the physics governing the onset of flow was maintained for all tests; however, once gas started to be mobile the permeability of the kaolinite filled fracture plane was inconsistent, resulting in variations of behaviour post gas entry.



**Figure 41** –Results for three gas injection tests conducted on a fracture oriented 15° to the slip plane. As can be seen, considerable differences are seen in peak pressure and form of the curve indicating that fracture transmissivity is not repeatable.



**Figure 42** –Gas entry pressure predicted from the average flow at STP for three gas injection tests conducted on a fracture oriented 15° to the slip plane. As can be seen, repeatable gas entry pressure is seen for all three tests.

Test	Fracture angle	+/-	Method 1			Method 2		
			Gas entry pressure (kPa)	Average entry pressure	+/-	Gas entry pressure (kPa)	Average entry pressure	+/-
15degs(8)	15°	0.5°	7500	7580	72	4850	4840	48
15degs(9)			7500			4732		
15degs(10)			7750			4922		

**Table 10** – Results for gas entry pressure for three gas injection experiments conducted at an angle of 15°. Method 1 = gas entry determined from STP gas flow into the fracture; Method 2 = entry pressure inferred from comparing pressure curve with ideal gas law

#### 4.4 GAS BREAKTHROUGH EXPERIMENTS ON A SLIP PLANE ORIENTATION OF 30°

A total of four gas injection experiments were conducted on a fracture oriented 30° with respect to the slip direction. As stated previously, each test was performed as identical as possible, with identical water content of gouge produced, similar normal load, similar volumes of gas, and identical gas injection rates. The only parameter that is likely to have varied between tests was the thickness of the gouge at the start of the experiment. However, as best as could be established, this did not vary significantly between tests as the gouge became very thin in all tests.

##### 4.4.1 Test ASR\_Tau09\_30gGI (Gas test 1)

The first test conducted on a fracture oriented 30° to the slip-plane was test ASR\_Tau09\_30gGI; the first gas injection test conducted. The results of the test are summarised in Figure 43. As can be seen in Figure 43a, the gas injection experiment resulted in a maximum gas pressure of approximately 8 MPa, with peak pressure achieved. The normal displacement data (Figure 43c) showed that the fracture compressed through-out the test history. The step in the data at Day 8

does not correlate with any other response and therefore this is inferred to be a system error. The angled shear rig (ASR) was originally designed with only a single eddy current sensor and this showed a complex history (Figure 43d). Compression was generally seen, with dilation beginning at Day 7. This may correspond with a change in slope of the gas pressure curve and indicate enhanced flow into the fracture.

Figure 43b shows the difference between the gas pressure observed and the predicted pressure from the ideal gas law. As seen, this data suggests that gas started to enter the fracture at around Day 1 when the gas pressure was 4,375 kPa. Figure 43e shows the average flow at STP into the fracture, with gas entry inferred to be approximately 5,200 kPa.

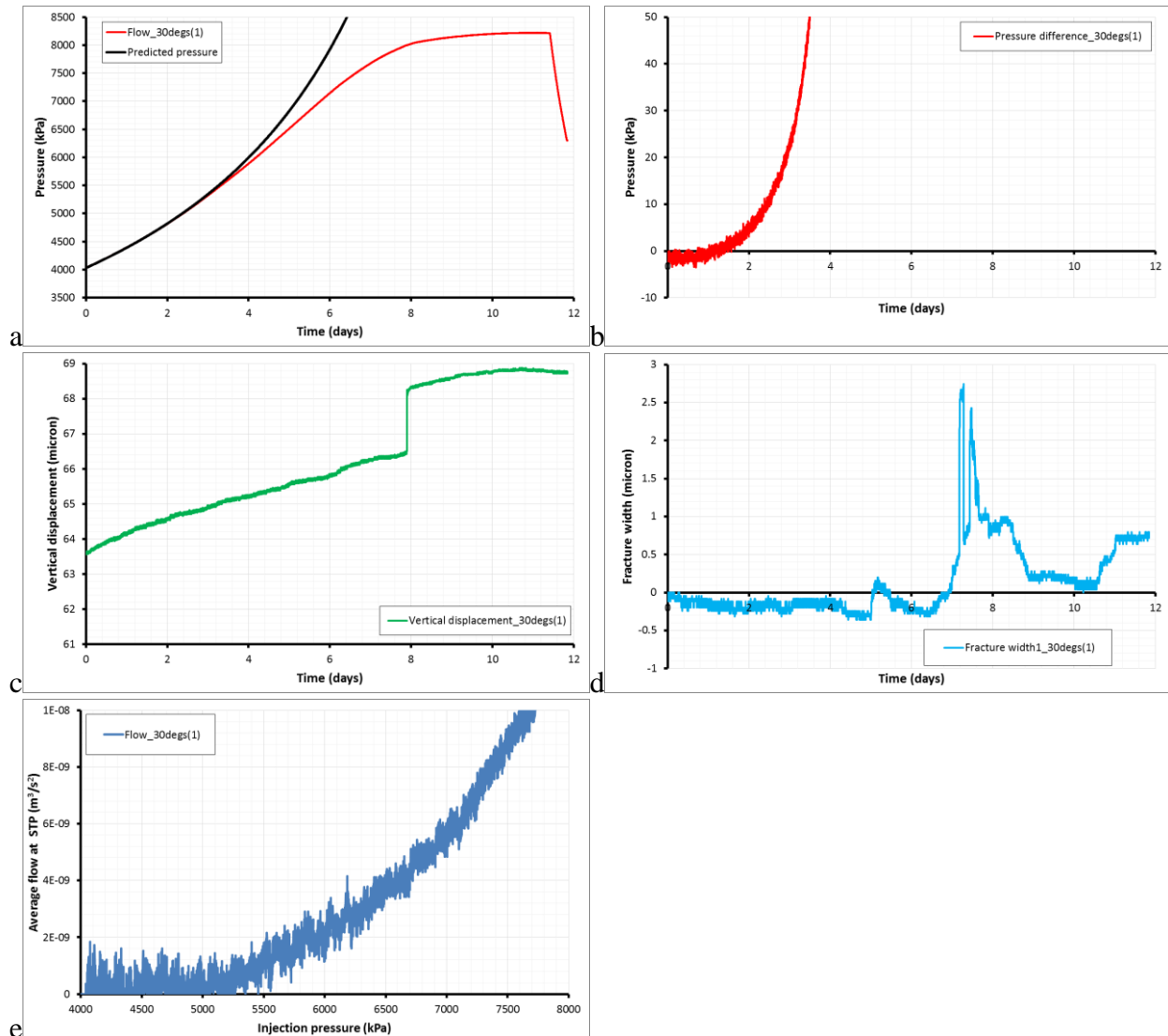


**Figure 43** – Results for gas injection test 1 / ASR\_Tau09\_30gGI. a) Gas injection pressure compared with prediction from ideal gas law; b) comparison of gas injection and ideal gas law as a way of predicting gas entry pressure; c) normal displacement; d) fracture width; e) flow into the slip plane as a way of predicting gas entry pressure.

#### 4.4.2 Test ASR\_Tau11\_30gGI (Gas test 2)

The second test conducted on a fracture oriented 30° to the slip-plane was test ASR\_Tau11\_30gGI; the second gas injection test conducted. The results of the test are summarised in Figure 44. As can be seen in Figure 44a, the gas injection experiment resulted in a maximum gas pressure of approximately 15.5 MPa, with peak pressure not achieved. Following the cessation of gas injection on Day 12, a gas shut-in stage was conducted for three days. The

normal displacement data (Figure 44c) showed that the fracture compressed through-out the test history. The angled shear rig (ASR) was originally designed with only a single eddy current sensor and this showed a complex history (Figure 44d). Compression was initially seen, with dilation events that may be system errors. The dilation initiated approximately Day 6 corresponded with the onset of gas flow inferred from the ideal gas law (Figure 40b).

Figure 44b shows the difference between the gas pressure observed and the predicted pressure from the ideal gas law. As seen, this data suggests that gas started to enter the fracture at around Day 6 when the gas pressure was 7,380 kPa. Figure 43e shows the average flow at STP into the fracture, with gas entry inferred to be approximately 8,000 kPa.

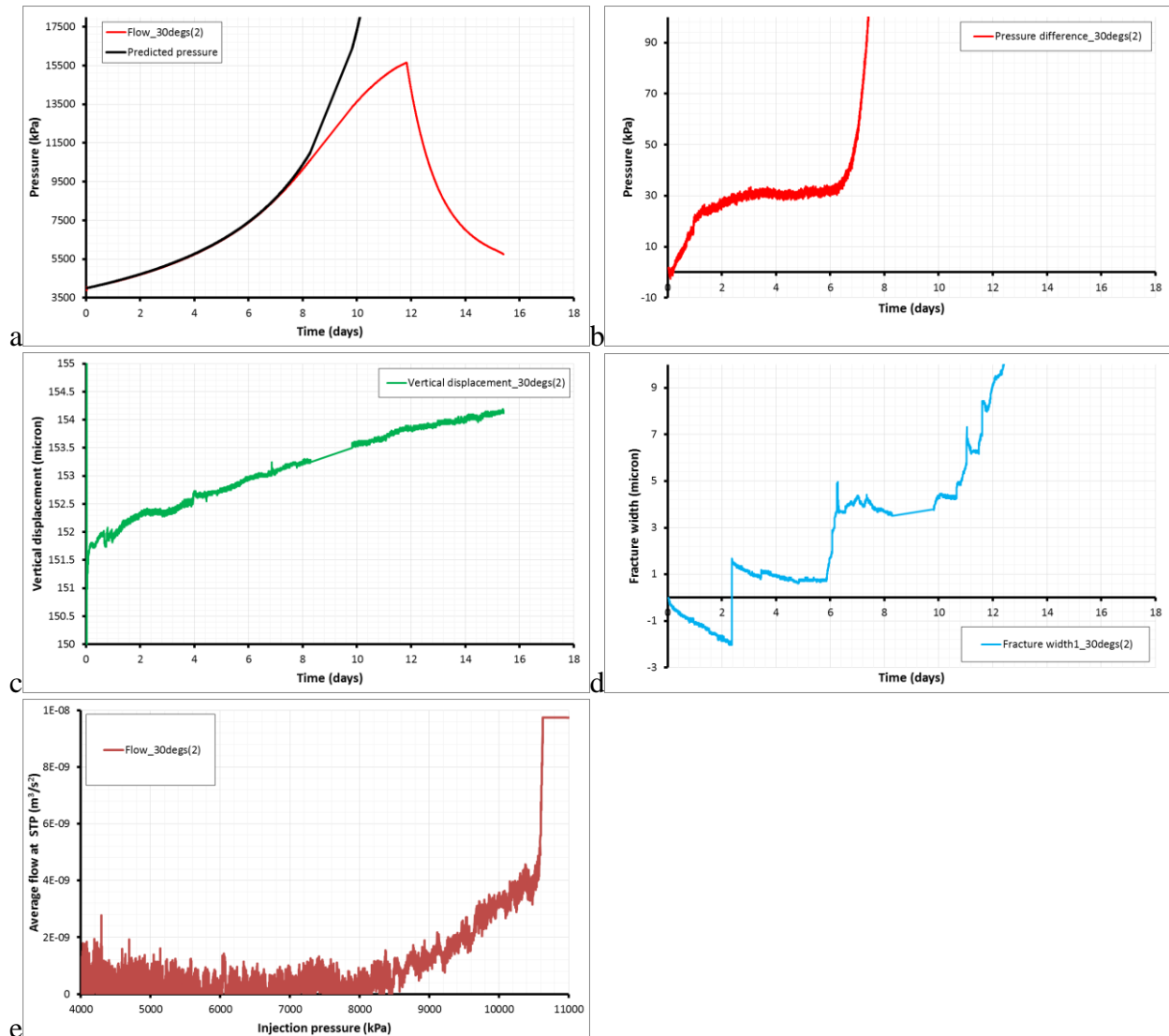


**Figure 44** – Results for gas injection test 2 / ASR\_Tau11\_30gGI. a) Gas injection pressure compared with prediction from ideal gas law; b) comparison of gas injection and ideal gas law as a way of predicting gas entry pressure; c) normal displacement; d) fracture width; e) flow into the slip plane as a way of predicting gas entry pressure.

#### 4.4.3 Test ASR\_Tau12\_30gGI (Gas test 3)

The third test conducted on a fracture oriented 30° to the slip-plane was test ASR\_Tau12\_30gGI; the third gas injection test conducted. The results of the test are summarised in Figure 45. As can be seen in Figure 45a, the gas injection experiment resulted in a maximum gas pressure of approximately 11 MPa, with peak pressure achieved and a loss of gas pressure as the fracture became highly conductive. The normal displacement data (Figure 45c) showed that the fracture

dilated initially and following this compressed through-out the rest of the test history. As can be seen, a significant dilation event is seen at the time of the gas breakthrough. The angled shear rig (ASR) was originally designed with only a single eddy current sensor and this showed a complex history (Figure 45d). Dilation was initially seen, followed by compression, with dilatant episodes beginning around Day 5.

Figure 45b shows the difference between the gas pressure observed and the predicted pressure from the ideal gas law. As seen, this data suggests that gas started to enter the fracture at around Day 1.5 when the gas pressure was 4,700 kPa. Figure 45e shows the average flow at STP into the fracture, with gas entry inferred to be approximately 7,000 kPa.

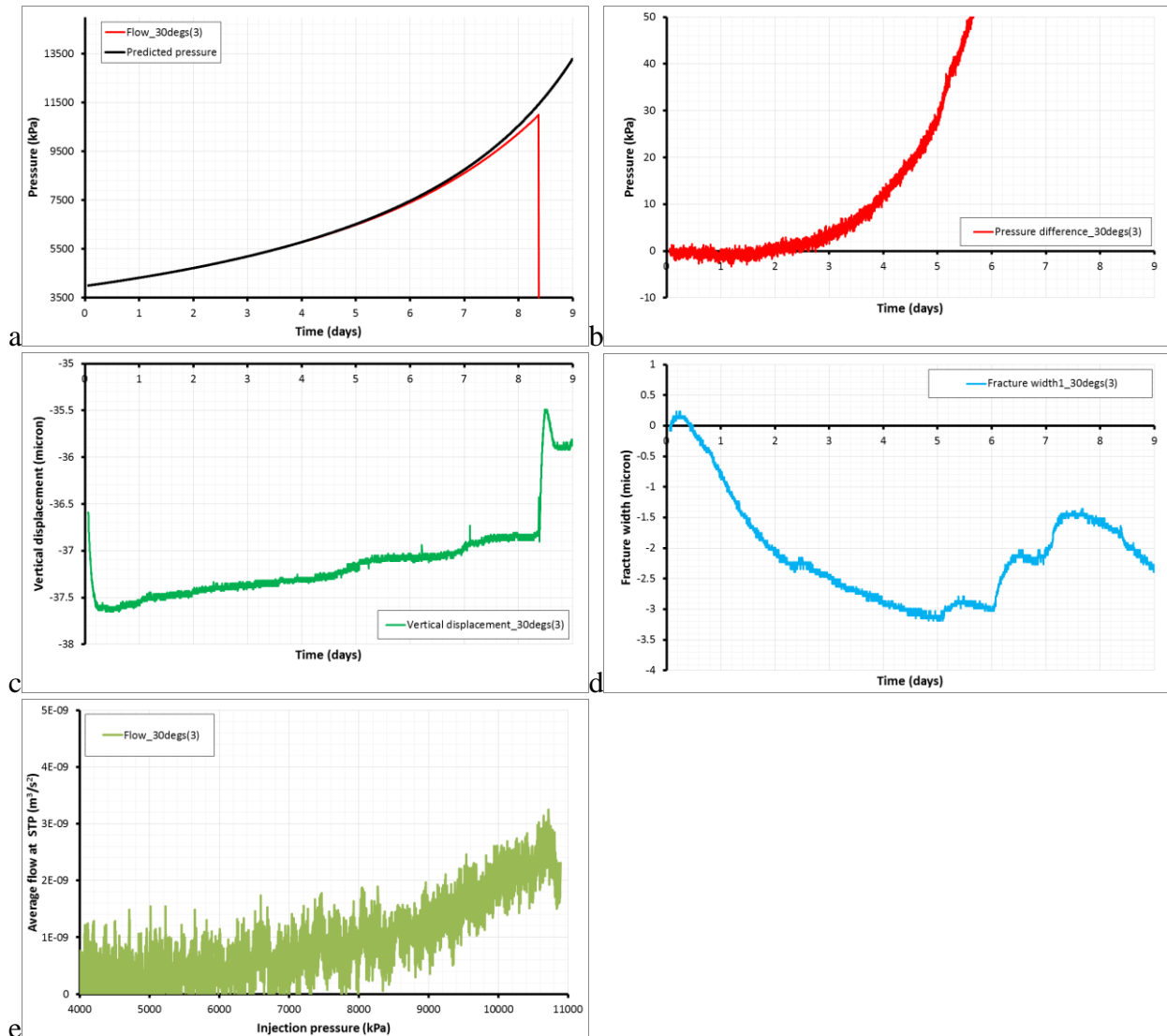


**Figure 45** – Results for gas injection test 3 / ASR\_Tau12\_30gGI. a) Gas injection pressure compared with prediction from ideal gas law; b) comparison of gas injection and ideal gas law as a way of predicting gas entry pressure; c) normal displacement; d) fracture width; e) flow into the slip plane as a way of predicting gas entry pressure.

#### 4.4.4 Test ASR\_Tau13\_30gGI (Gas test 4)

The fourth test conducted on a fracture oriented 30° to the slip-plane was test ASR\_Tau13\_30gGI; the fourth gas injection test conducted. The results of the test are summarised in Figure 46. As can be seen in Figure 46a, the gas injection experiment resulted in a maximum gas pressure of approximately 14 MPa, with peak pressure not achieved and a loss of gas pressure as the fracture became highly conductive. The normal displacement data (Figure

46c) showed that the fracture dilated initially and following this dilated through-out the rest of the test history. Dissimilar to test ASR\_Tau12\_30gGI, no dilation was seen at the time of gas pressure loss. The single eddy current sensor showed a complex history (Figure 46d). Dilation was initially seen, followed by compression, with dilatant episodes beginning about Day 6. At the time of gas pressure loss, the eddy current sensor was showing that the fracture was compressing.

Figure 46b shows the difference between the gas pressure observed and the predicted pressure from the ideal gas law. As seen, this data suggests that gas started to enter the fracture at around Day 4 when the gas pressure was 4,840 kPa. Figure 46e shows the average flow at STP into the fracture, with gas entry inferred to be approximately 8,000 kPa.

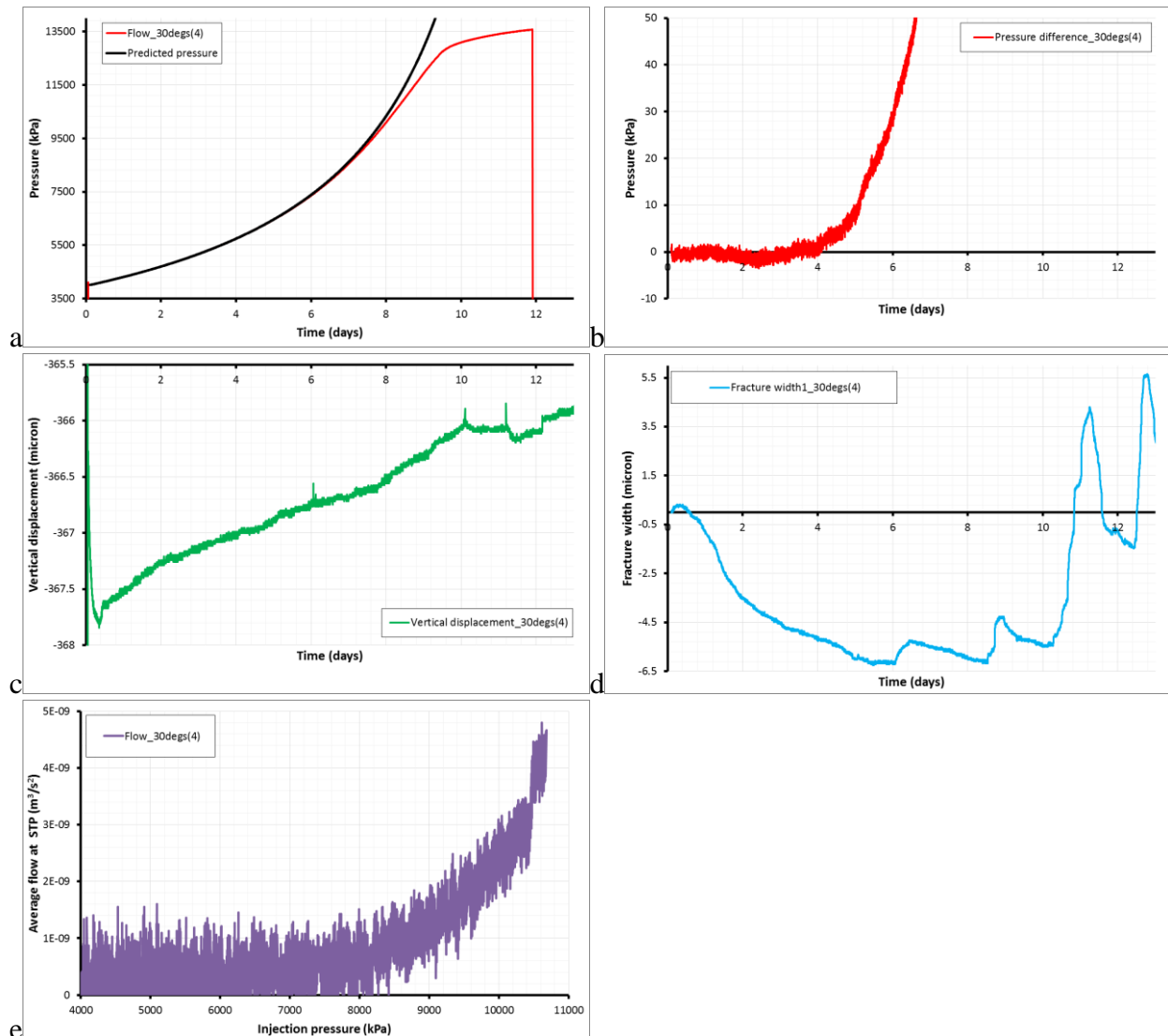
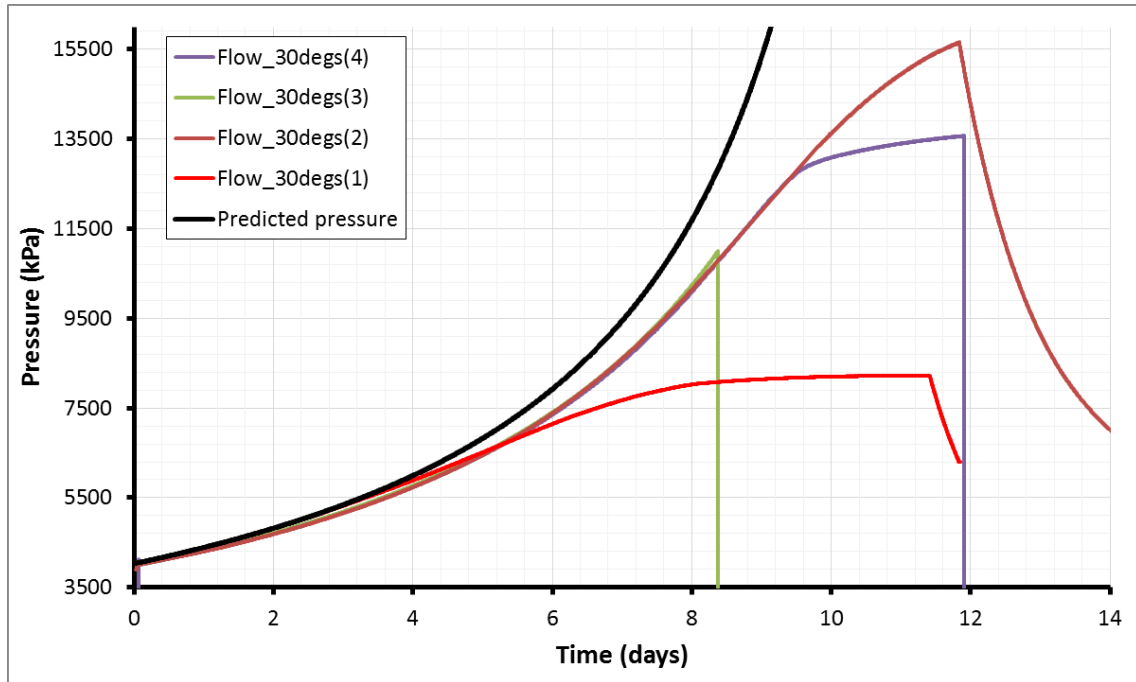


**Figure 46** – Results for gas injection test 4 / ASR\_Tau13\_30gGI. a) Gas injection pressure compared with prediction from ideal gas law; b) comparison of gas injection and ideal gas law as a way of predicting gas entry pressure; c) normal displacement; d) fracture width; e) flow into the slip plane as a way of predicting gas entry pressure.

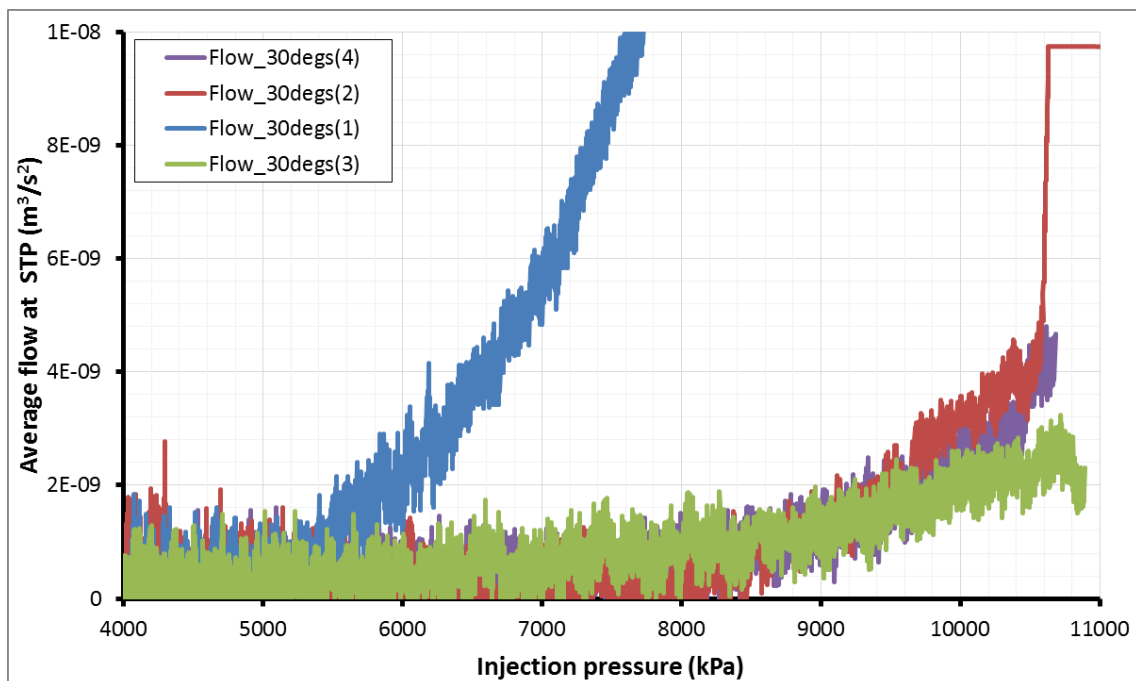
#### 4.4.5 Results for tests conducted in a slip plane orientation of 30°

Figure 47 shows the gas pressure for all five of the gas injection tests conducted on a fracture oriented 30° to the slip-direction. As clearly seen, there is little repeatability in the gas pressures achieved with pressures between 8 and 16 MPa achieved. However, close examination of the data showed that gas entry pressure had a much better repeatability. As described above, two

methods were employed for estimating the gas entry pressure; the first compared the gas pressure result with the predicted pressure from the ideal gas law and the second calculated average flow at STP into the fracture. All results are summarised in Table 11, with the results from flow into the fracture shown in Figure 48. As seen in Figure 48, three tests showed similar gas entry pressures of between 7 and 8 MPa, whilst one test had an anomalously low gas entry pressure of 5.2 MPa.



**Figure 47** –Results for four gas injection tests conducted on a fracture oriented 30° to the slip plane. As can be seen, considerable differences are seen in peak pressure and form of the curve indicating that fracture transmissivity is not repeatable.



**Figure 48** – Gas entry pressure predicted from the average flow at STP for four gas injection tests conducted on a fracture oriented 30° to the slip plane. As can be seen, repeatable gas entry pressure is seen for three of the four tests, with one test (1) showing a considerably lower gas entry pressure.

Test	Fracture angle	+/-	Method 1			Method 2		
			Gas entry pressure (kPa)	Average entry pressure	+/-	Gas entry pressure (kPa)	Average entry pressure	+/-
30degs(1)	30°	0.5°	5200	7670	289	4373	4640	120
30degs(2)			8000			7380		
30degs(3)			7000			4700		
30degs(4)			8000			4839		

**Table 11** – Results for gas entry pressure for four gas injection experiments conducted at an angle of 30°. Method 1 = gas entry determined from STP gas flow into the fracture; Method 2 = entry pressure inferred from comparing pressure curve with ideal gas law

#### 4.5 GAS BREAKTHROUGH EXPERIMENTS ON A SLIP PLANE ORIENTATION OF 45°

A total of three gas injection experiments were conducted on a fracture oriented 45° with respect to the slip direction. As stated previously, each test was performed as identical as possible, with identical water content of gouge produced, similar normal load, similar volumes of gas, and identical gas injection rates. The only parameter that is likely to have varied between tests was the thickness of the gouge at the start of the experiment. However, as best as could be established, this did not vary significantly between tests as the gouge became very thin in all tests.

##### 4.5.1 Test ASR\_Tau25\_45gGI (Gas test 15)

The first test conducted on a fracture oriented 45° to the slip-plane was test ASR\_Tau25\_45gGI; the fifteenth gas injection test conducted. The results of the test are summarised in Figure 49. As can be seen in Figure 49a, the gas injection experiment resulted in a maximum gas pressure of approximately 15 MPa, with peak pressure not achieved. Following the cessation of gas injection on Day 12, a gas shut-in stage was conducted for two days. An asymptote of pressure would have taken a significant amount of time and so the experiment was halted. The normal displacement data (Figure 49c) showed that the fracture compressed throughout the entire test history. The eddy current sensors showed a complex history (Figure 49d). Initially one sensor showed compression, whilst the other showed dilation. At the onset of gas flow inferred from the ideal gas law (Figure 49b), the fracture was seen to dilate. The complexity of the fracture width data suggest that the top-block was “rocking” about the central loading point and did move when gas became mobile.

Figure 49b shows the difference between the gas pressure observed and the predicted pressure from the ideal gas law. As seen, this data suggests that gas started to enter the fracture at around Day 3.5 when the gas pressure was 5,050 kPa. Figure 49e shows the average flow at STP into the fracture, with gas entry inferred to be approximately 8,500 kPa. Considerable difference was therefore seen in gas entry pressure predicted from the two employed methods.

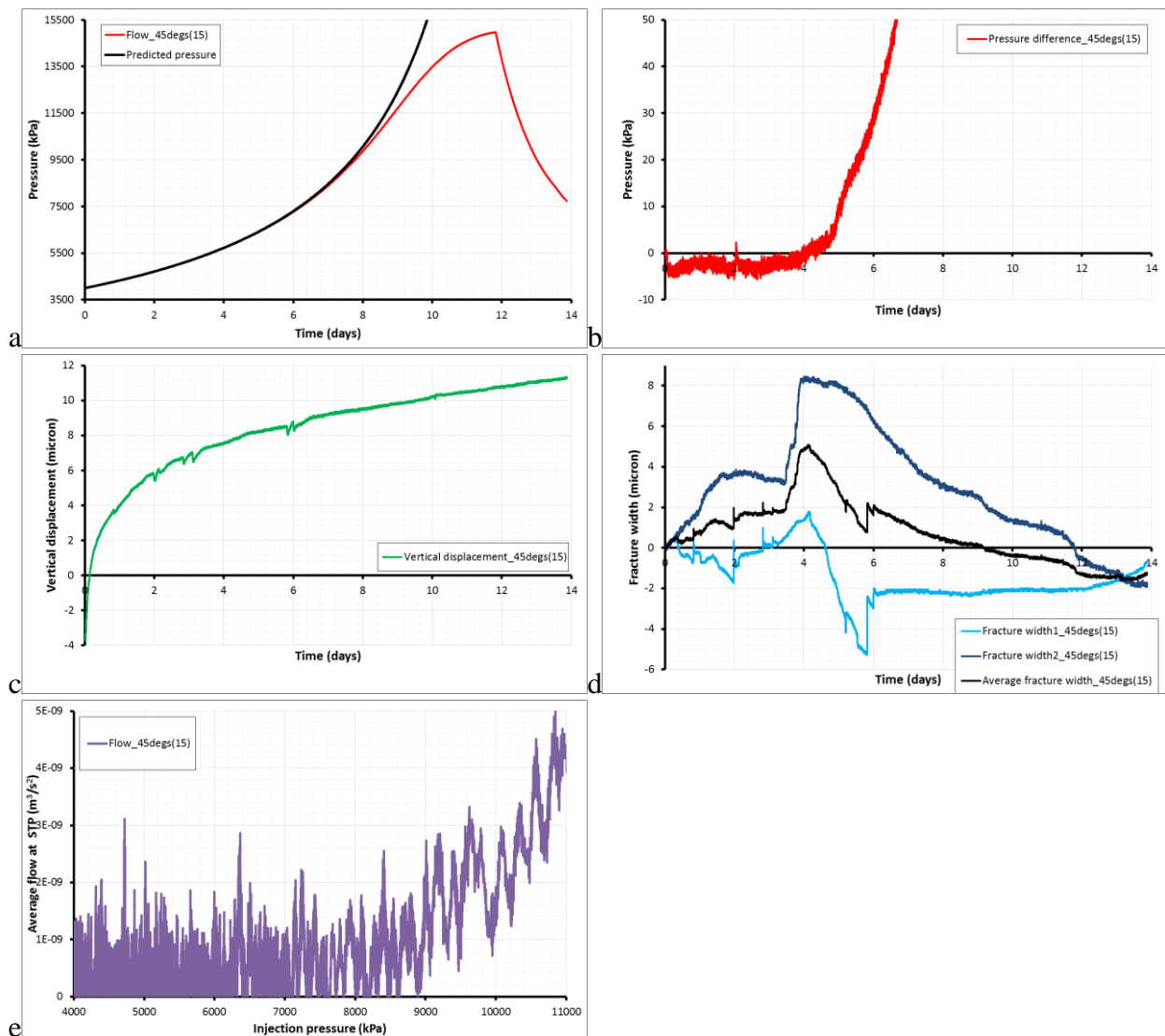


**Figure 49** – Results for gas injection test 15 / ASR\_Tau25\_45gGI. a) Gas injection pressure compared with prediction from ideal gas law; b) comparison of gas injection and ideal gas law as a way of predicting gas entry pressure; c) normal displacement; d) fracture width; e) flow into the slip plane as a way of predicting gas entry pressure.

#### 4.5.2 Test ASR\_Tau26\_45gGI (Gas test 16)

The second test conducted on a fracture oriented  $45^\circ$  to the slip-plane was test ASR\_Tau26\_45gGI; the sixteenth gas injection test conducted. The results of the test are summarised in Figure 50. As can be seen in Figure 50a, the gas injection experiment resulted in a maximum gas pressure of approximately 9.5 MPa, with peak pressure not achieved. The normal displacement data (Figure 50c) showed that the fracture compressed throughout the entire test history. The eddy current sensors showed a complex history (Figure 50d). Initially one sensor showed compression, whilst the other showed dilation. Unlike in the previous test (ASR\_Tau25\_45gGI), at the onset of gas flow inferred from the ideal gas law (Figure 49b), no dilation or compression was seen of the fracture. A later dilation was seen at Day 6 in one sensor, which could signify the onset of enhanced gas flow.

Figure 50b shows the difference between the gas pressure observed and the predicted pressure from the ideal gas law. As seen, this data suggests that gas started to enter the fracture at around Day 3.5 when the gas pressure was 5,375 kPa. Figure 50e shows the average flow at STP into the fracture, with gas entry inferred to be approximately 7,500 kPa. Considerable difference was therefore seen in gas entry pressure predicted from the two employed methods.

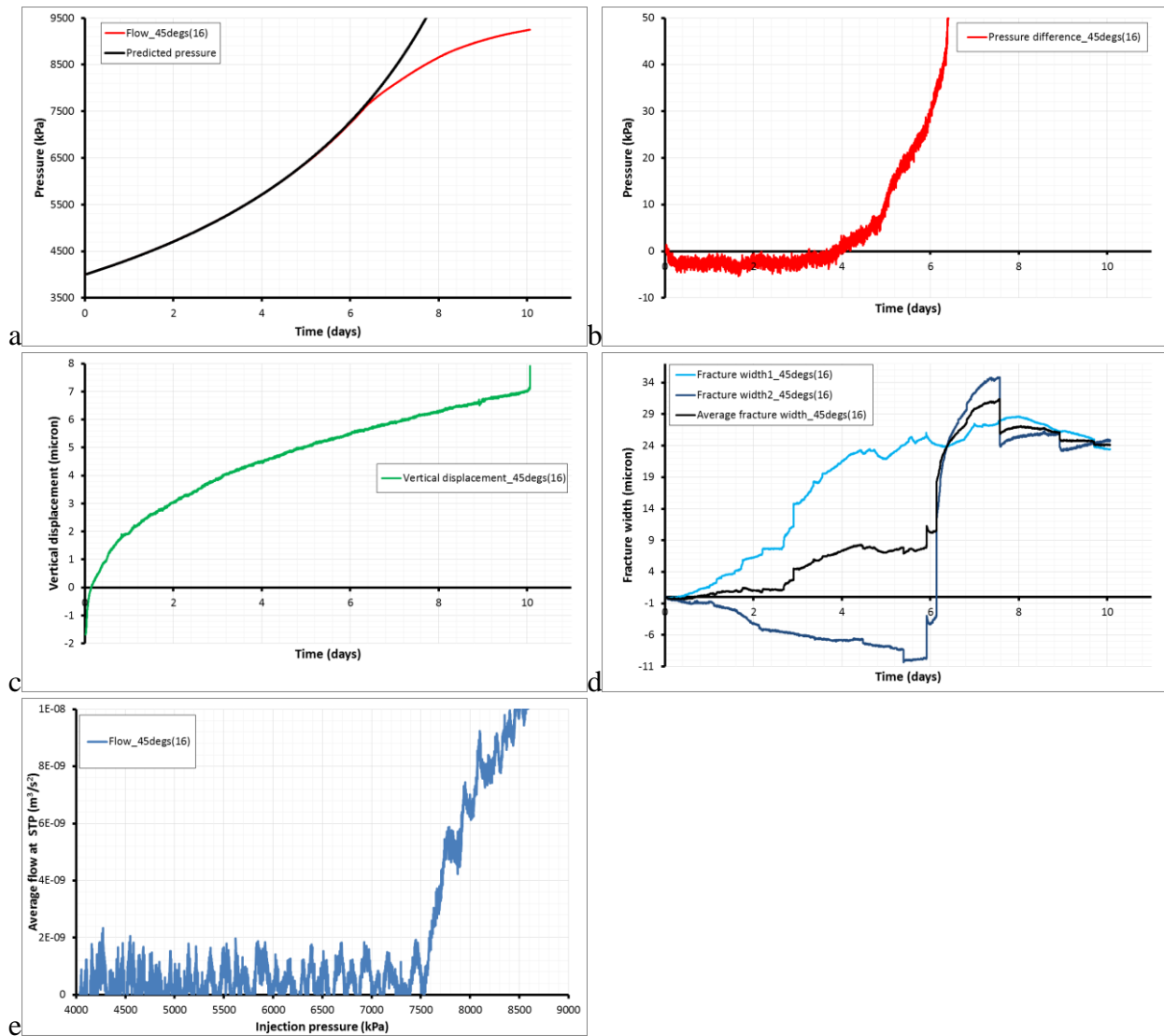


**Figure 50** – Results for gas injection test 16 / ASR\_Tau26\_45gGI. a) Gas injection pressure compared with prediction from ideal gas law; b) comparison of gas injection and ideal gas law as a way of predicting gas entry pressure; c) normal displacement; d) fracture width; e) flow into the slip plane as a way of predicting gas entry pressure.

#### 4.5.3 Test ASR\_Tau27\_45gGI (Gas test 17)

The third test conducted on a fracture oriented  $45^\circ$  to the slip-plane was test ASR\_Tau27\_45gGI; the seventeenth gas injection test conducted. The results of the test are summarised in Figure 51. As can be seen in Figure 51a, the gas injection experiment resulted in a maximum gas pressure of approximately 8.2 MPa, with peak pressure not achieved. The normal displacement data (Figure 51c) showed that the fracture compressed throughout the entire test history. The eddy current sensors showed a complex history (Figure 51d). Both sensors initially showed dilation, quickly followed after Day 1 by compression. The complexity of the fracture width data suggest that the top-block was “rocking” about the central loading point, but did not move when gas became mobile.

Figure 51b shows the difference between the gas pressure observed and the predicted pressure from the ideal gas law. As seen, this data suggests that gas started to enter the fracture at around Day 1.8 when the gas pressure was 4,550 kPa. Figure 51e shows the average flow at STP into the fracture, with gas entry inferred to be approximately 5,000 kPa. For test ASR\_Tau27\_45gGI there is agreement in the prediction of gas entry pressure from the two methods employed.

However, the estimate from STP flow into the fracture is considerably lower when compared with the other two tests conducted on the same orientation of fracture.

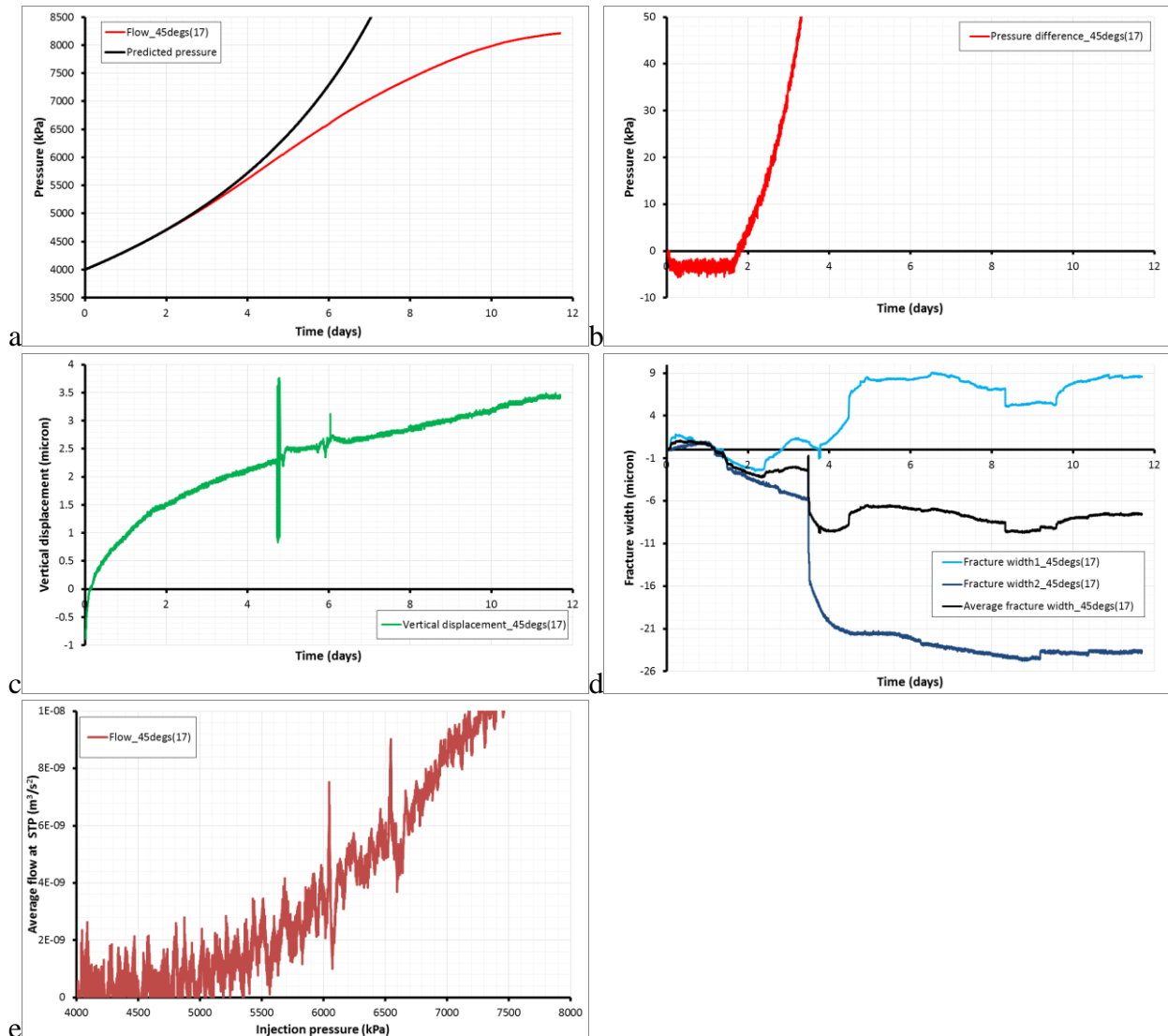


**Figure 51** – Results for gas injection test 17 / ASR\_Tau27\_45gGI. a) Gas injection pressure compared with prediction from ideal gas law; b) comparison of gas injection and ideal gas law as a way of predicting gas entry pressure; c) normal displacement; d) fracture width; e) flow into the slip plane as a way of predicting gas entry pressure.

#### 4.5.4 Results for tests conducted on a slip plane orientation of 45°

Figure 52 shows the gas pressure for all three of the gas injection tests conducted on a fracture oriented 45° to the slip-direction. As clearly seen, there is little repeatability in the gas pressures achieved with pressures between 8 and 15 MPa achieved. However, close examination of the data showed that gas entry pressure had a much better repeatability. As described above, two methods were employed for estimating the gas entry pressure; the first compared the gas pressure result with the predicted pressure from the ideal gas law and the second calculated average flow at STP into the fracture. All results are summarised in Table 12, with the results from flow into the fracture shown in Figure 53. As seen in Figure 53, two tests showed similar gas entry pressures of between 7.5 and 8.5 MPa, whilst one test had an anomalously low gas entry pressure of 5 MPa.

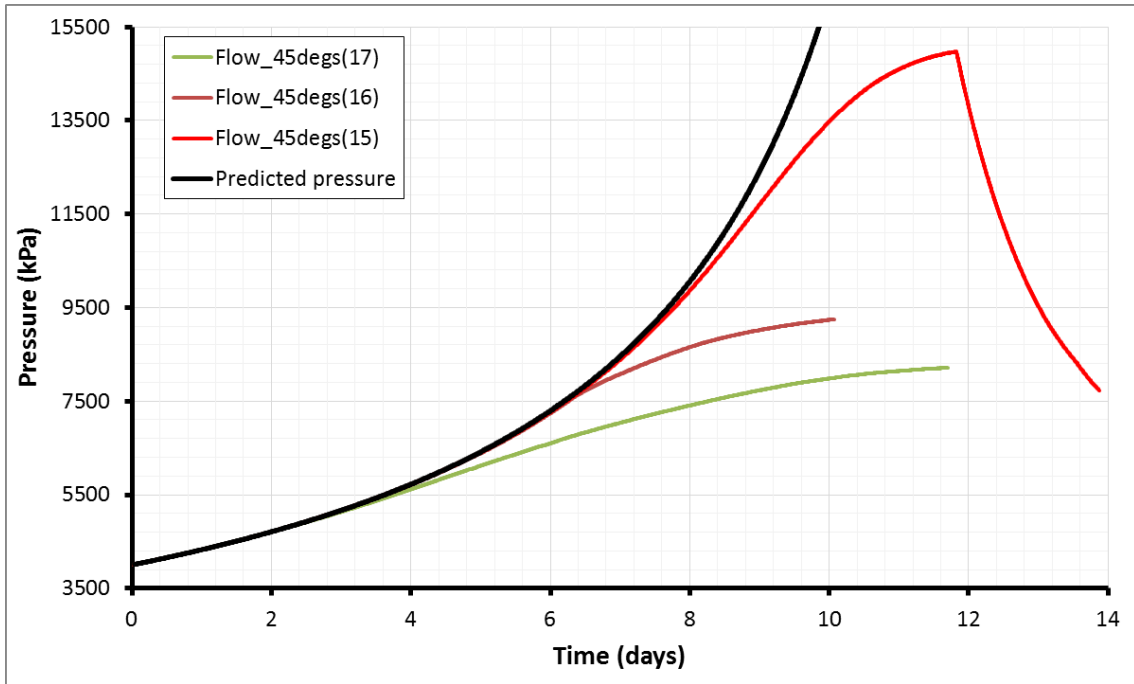


**Figure 52** –Results for three gas injection tests conducted on a fracture oriented 45° to the slip plane. As can be seen, considerable differences are seen in peak pressure and form of the curve indicating that fracture transmissivity is not repeatable.

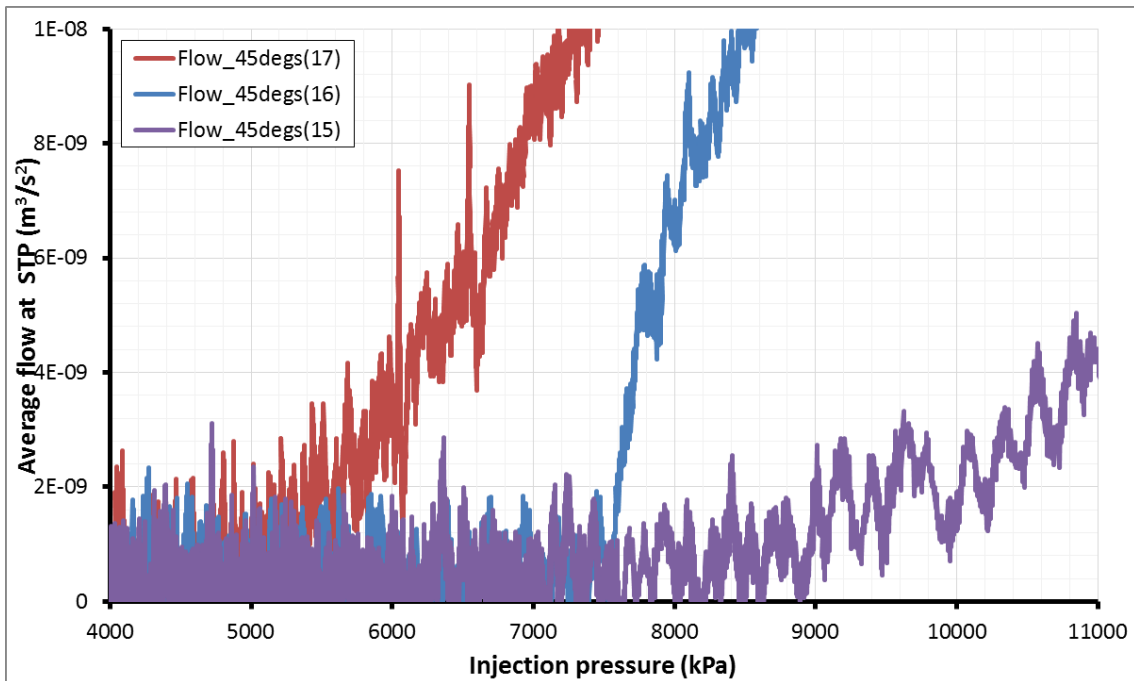


**Figure 53** – Gas entry pressure predicted from the average flow at STP for three gas injection tests conducted on a fracture oriented 45° to the slip plane. As can be seen, repeatable gas entry pressure is seen for two of the three tests, with one test (17) showing a considerably lower gas entry pressure.

Test	Fracture angle	+/-	Method 1			Method 2		
			Gas entry pressure (kPa)	Average entry pressure	+/-	Gas entry pressure (kPa)	Average entry pressure	+/-
45degs(15)	45°	0.5°	8500	8000	354	5046	4980	212
45degs(16)			7500			5373		
45degs(17)			5000			4531		

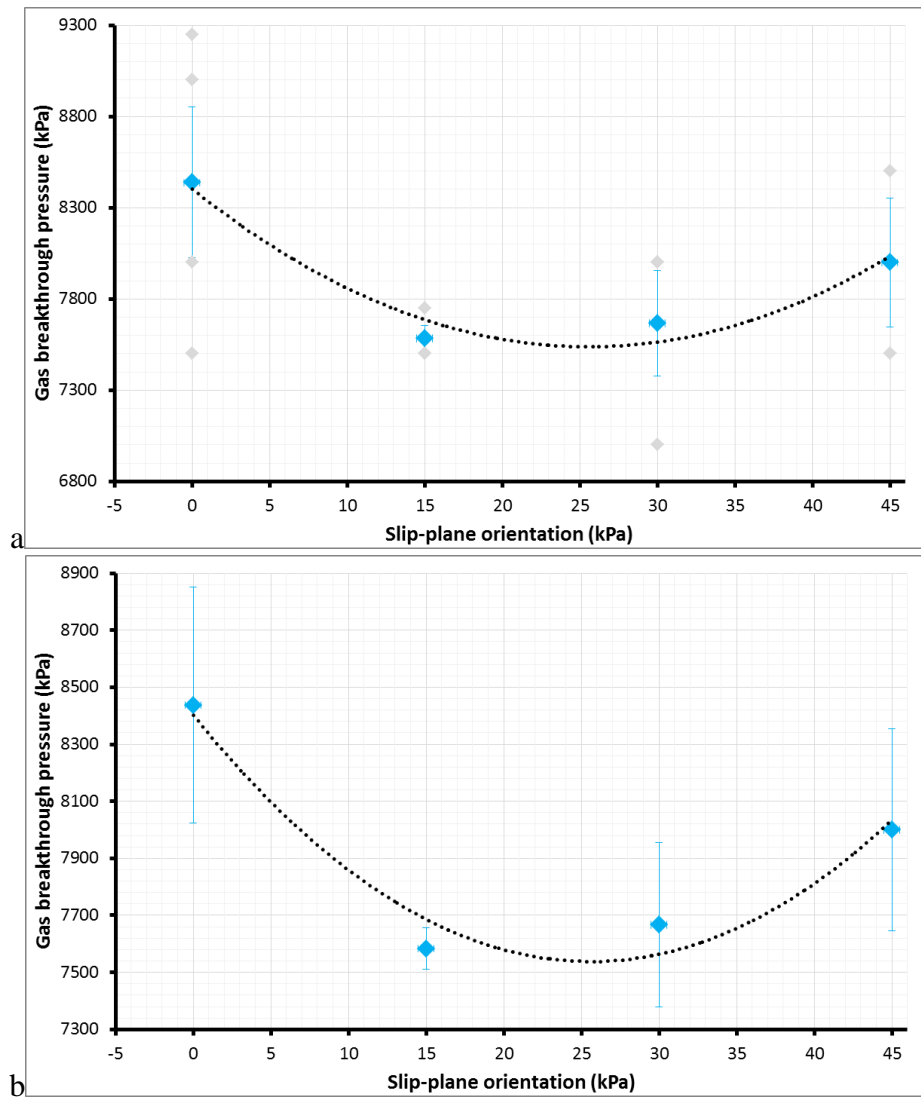
**Table 12** – Results for gas entry pressure for three gas injection experiments conducted at an angle of 45°. Method 1 = gas entry determined from STP gas flow into the fracture; Method 2 = entry pressure inferred from comparing pressure curve with ideal gas law

#### 4.6 RESULTS AND DISCUSSION FOR TESTS CONDUCTED AT DIFFERENT ORIENTATIONS

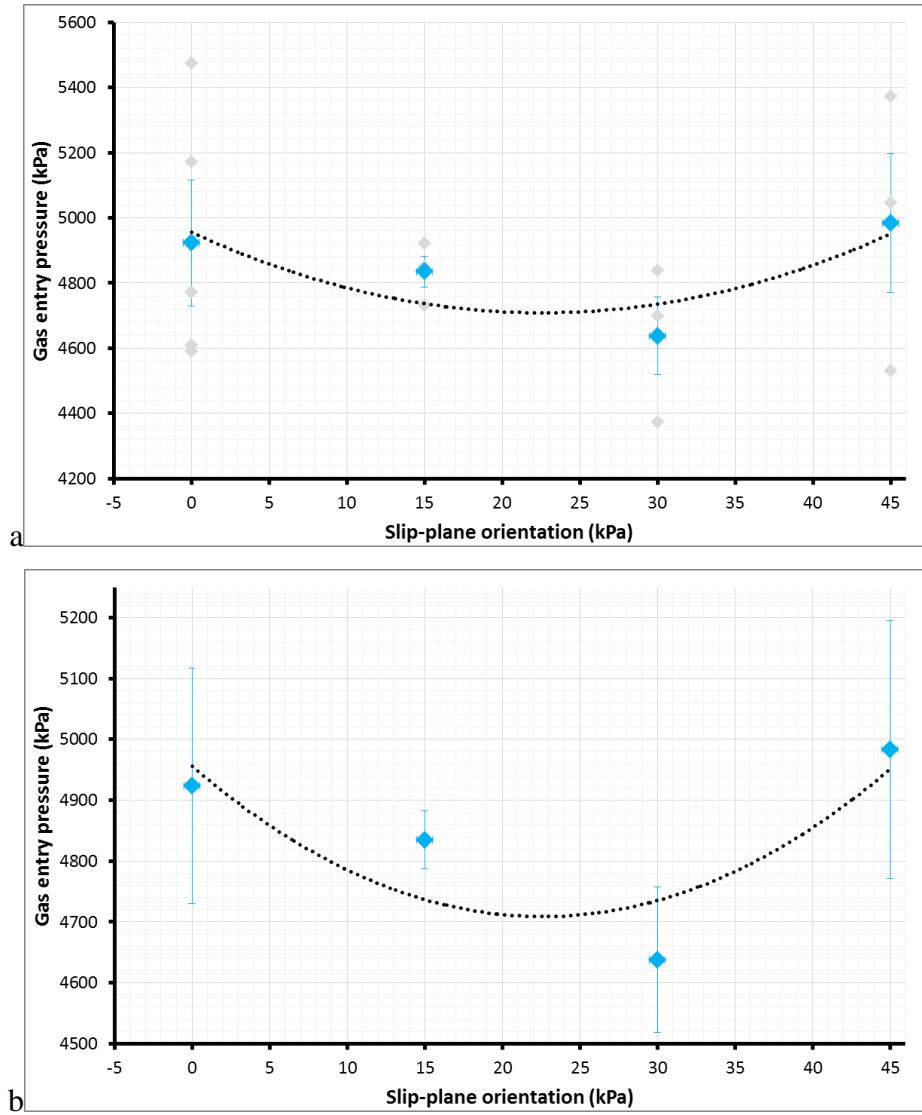
All test results are summarised in Table 13. Figure 54 and Figure 55 show the gas entry pressure for all fifteen of the gas injection tests conducted on fractures oriented 0°, 15°, 30°, and 45° to the slip-direction. The data in Figure 54 was determined from average flow at STP into the fracture. The data in Figure 55 was determined from the ideal gas law. As can be clearly seen, both methods of determining gas entry pressure showed variation with respect to fracture orientation. It has to be noted that Figure 54a and Figure 55a both show considerable spread in the data achieved at each of the four fracture orientations. However, even taking into account this spread in result it is clear that a relationship exists between gas entry pressure and fracture orientation. Both methods suggest that the minimum gas entry pressure occurs when the fracture orientation is approximately 25° to the shear direction. Kaolinite has a reported friction angle of 15° (Waltham, 1994), therefore the prediction from the parabolic fit of the data is not related to friction angle. However, STP flow predicts a gas entry pressure minimum on a fracture oriented at 15°; therefore gas entry pressure may to be related to friction angle.

Figure 56 shows the average data for gas entry pressure at the different fracture orientations for both methods of predicting gas entry pressure. As can be seen, a similar relationship of variation of gas entry pressure with fracture orientation was seen. However, greater variability is seen in the prediction from STP flow, which also predicts an entry pressure approximately 3 MPa greater than the prediction from the ideal gas flow.

The repeatability seen in gas entry pressure and not peak pressure suggests that the physics governing the onset of flow was maintained for all tests; however, once gas started to be mobile the permeability of the kaolinite filled fracture plane was inconsistent, resulting in variations of behaviour post gas entry. This may relate to the number of pathways that form.



**Figure 54** – Relationship of gas entry pressure determined from STP gas flow into the fracture for all tests. a) all test data and average results; b) average data.



**Figure 55** – Relationship of gas entry pressure determined from the ideal gas law for all tests. a) all test data and average results; b) average data.

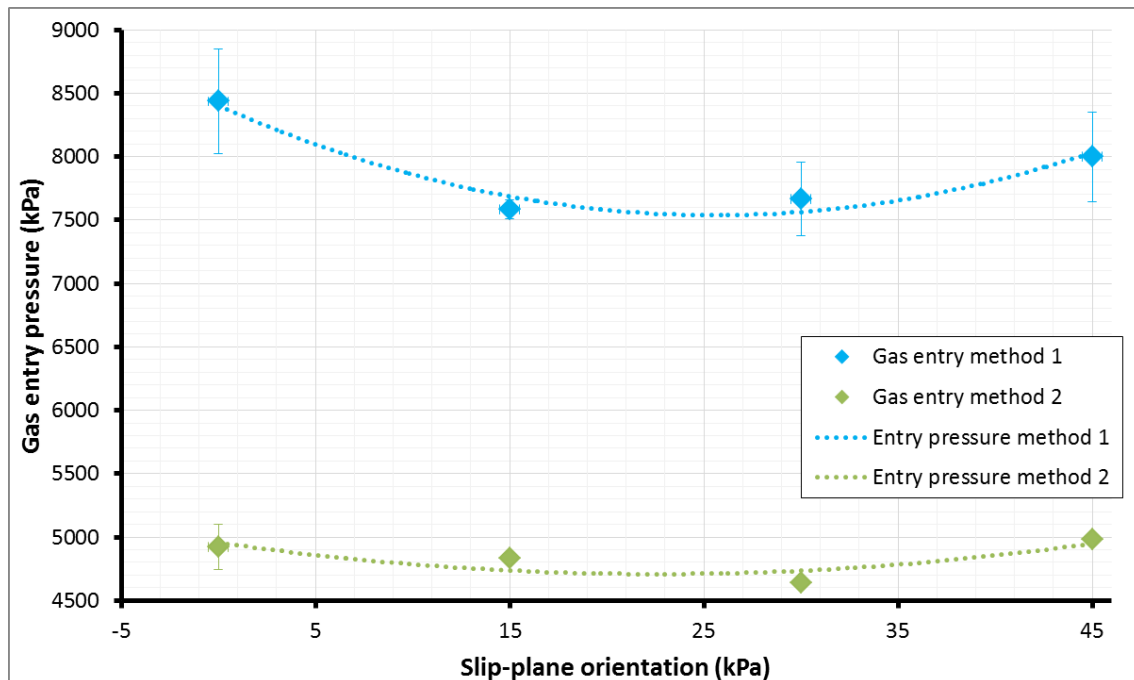


**Figure 56** – Comparison of results from the two methods used to determine gas entry pressure. Both methods show that gas entry pressure alters with fracture orientation, with entry pressure determined from STP flow into the fracture predicting higher pressures.

Test	Fracture angle	+/-	Method 1			Method 2		
			Gas entry pressure (kPa)	Average entry pressure	+/-	Gas entry pressure (kPa)	Average entry pressure	+/-
0degs(5)	0°	0.5°	5000	8440	413	4772	4920	193
0degs(6)			8000			4610		
0degs(7)			9000			4590		
0degs(11)			7500			5475		
0degs(12)			9250			5170		
15degs(8)	15°	0.5°	7500	7580	72	4850	4840	48
15degs(9)			7500			4732		
15degs(10)			7750			4922		
30degs(1)	30°	0.5°	5200	7670	289	4373	4640	120
30degs(2)			8000			7380		
30degs(3)			7000			4700		
30degs(4)			8000			4839		
45degs(15)	45°	0.5°	8500	8000	354	5046	4980	212
45degs(16)			7500			5373		
45degs(17)			5000			4531		

**Table 13** – Results for gas entry pressure for all gas injection experiments. Method 1 = gas entry determined from STP gas flow into the fracture; Method 2 = entry pressure inferred from comparing pressure curve with ideal gas law

## 4.7 THE EFFECT OF SHEAR DISPLACEMENT ON GAS ENTRY AND SUBSEQUENT GAS FLOW

A total of five gas injection experiments were conducted with the addition of active shear. Two tests were conducted on a flat slip plane, i.e. at an orientation of  $0^\circ$  with respect to the slip direction in order to look at repeatability. A further three tests were conducted at orientations of  $15^\circ$ ,  $30^\circ$  and  $45^\circ$  in order to investigate the relationship between active shear and gas entry pressure at different angles. As stated previously, each test was performed as identical as possible, with identical water content of gouge produced, similar normal load, similar volumes of gas, and identical gas injection rates. The only parameter that is likely to have varied between tests was the thickness of the gouge at the start of the experiment. However, as best as could be established, this did not vary significantly between tests as the gouge became very thin in all tests. In all shear tests the sample began shear at the same time as the constant flow pressure ramp was started.

### 4.7.1 Test ASR\_Tau28\_00gGIS (Gas test 18)

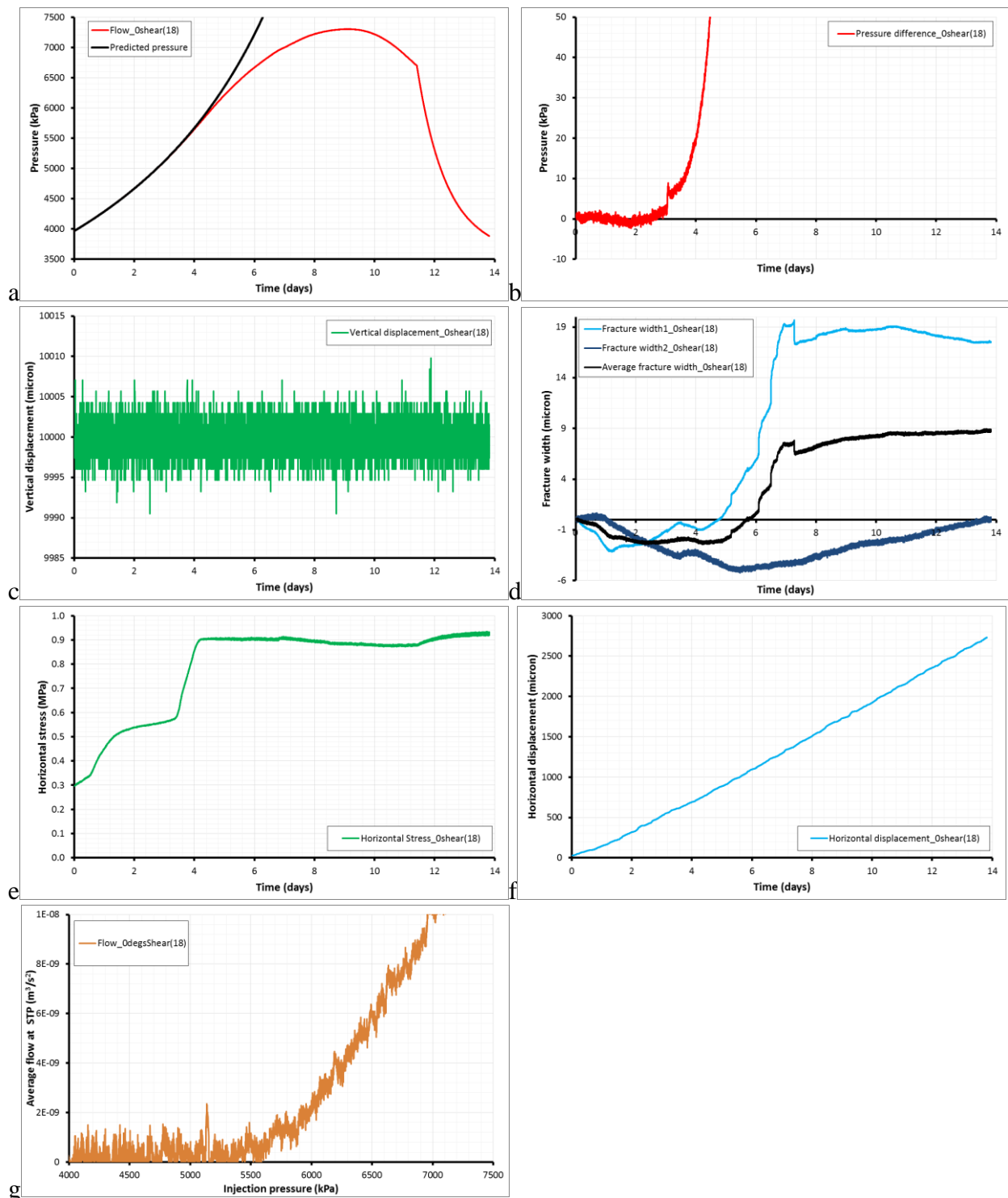
The first test conducted with active shear was performed on a fracture oriented  $0^\circ$  to the slip-plane was ASR\_Tau28\_00gGIS; the eighteenth gas injection test conducted. The results of the test are summarised in Figure 57. As can be seen in Figure 57a and Figure 57f, the sample was started to shear at the same time as the constant flow pressure ramp. The gas injection experiment resulted in a maximum gas pressure of approximately 7.3 MPa, with peak pressure achieved. Following the cessation of gas injection on Day 12, a gas shut-in stage was conducted for two days. An asymptote of pressure would have taken a significant amount of time and so the experiment was halted. The normal displacement data (Figure 57c) suggest that the induction sensor malfunctioned. The eddy current sensors showed a complex history (Figure 57d). One sensor showed minor dilation of approximately  $1\ \mu\text{m}$  followed by compression of  $6\ \mu\text{m}$ , whilst the other showed compression of  $3\ \mu\text{m}$  followed by dilation of over  $20\ \mu\text{m}$ . No correlation was seen between the fracture width sensor and gas flow inferred from the ideal gas law (Figure 57b). The data suggest that the top-block was “rocking” about the central loading point. Figure 57e shows the horizontal stress data; this indicated that peak and residual strength correspond and was achieved about Day 4 with a magnitude of 0.9 MPa.

Figure 57b shows the difference between the gas pressure observed and the predicted pressure from the ideal gas law. As seen, this data suggests that gas started to enter the fracture at around Day 2 when the gas pressure was 4,620 kPa. Figure 57g shows the average flow at STP into the fracture, with gas entry inferred to be approximately 5,500 kPa. The two estimates are approximately in agreement.

### 4.7.2 Test ASR\_Tau29\_00gGIS (Gas test 19)

The second test conducted with active shear was conducted on a fracture oriented  $0^\circ$  to the slip-plane was ASR\_Tau29\_00gGIS; the nineteenth gas injection test conducted. The results of the test are summarised in Figure 58. As can be seen in Figure 58a, the gas injection experiment resulted in a maximum gas pressure of approximately 8.25 MPa. Peak pressure was achieved and considerable pressure drop was experienced by the time that gas entry was halted; over 2.5 MPa pressure drop. This degree of pressure drop had not previously been observed and indicated that the slip-plane had become highly conductive. Following the cessation of gas injection on Day 11, a gas shut-in stage was conducted for half a day. An asymptote of pressure would have taken a significant amount of time and so the experiment was halted. The normal displacement data (Figure 58c) suggested that the induction sensor malfunctioned. The eddy current sensors showed a complex history (Figure 58d). Both sensors showed general dilation, with episodes of compression. It is possible that the onset of gas flow inferred from the ideal gas law (Figure 58b) was showing as enhanced dilation in one sensor and compression in the other, suggesting that the top-block “rocked” about the central loading point as gas started to move. Figure 57e shows the

horizontal stress data; this indicated that peak and residual strength correspond and was achieved about Day 3 with a magnitude of 0.9 MPa. However, at peak stress the horizontal stress started to increase until the end of the experiment.



**Figure 57** – Results for gas injection test 18 / ASR\_Tau28\_00gGIS. a) Gas injection pressure compared with prediction from ideal gas law; b) comparison of gas injection and ideal gas law as a way of predicting gas entry pressure; c) normal displacement; d) fracture width; e) horizontal stress; f) shear displacement; g) flow into the slip plane as a way of predicting gas entry pressure.

Figure 58b shows the difference between the gas pressure observed and the predicted pressure from the ideal gas law. As seen, this data suggests that gas started to enter the fracture at around Day 2 when the gas pressure was 4,700 kPa. Figure 58e shows the average flow at STP into the

fracture, with gas entry inferred to be approximately 6,000 kPa. In contrast to test ASR\_Tau28\_00gGIS, the methods used to predict gas entry gave dissimilar results.

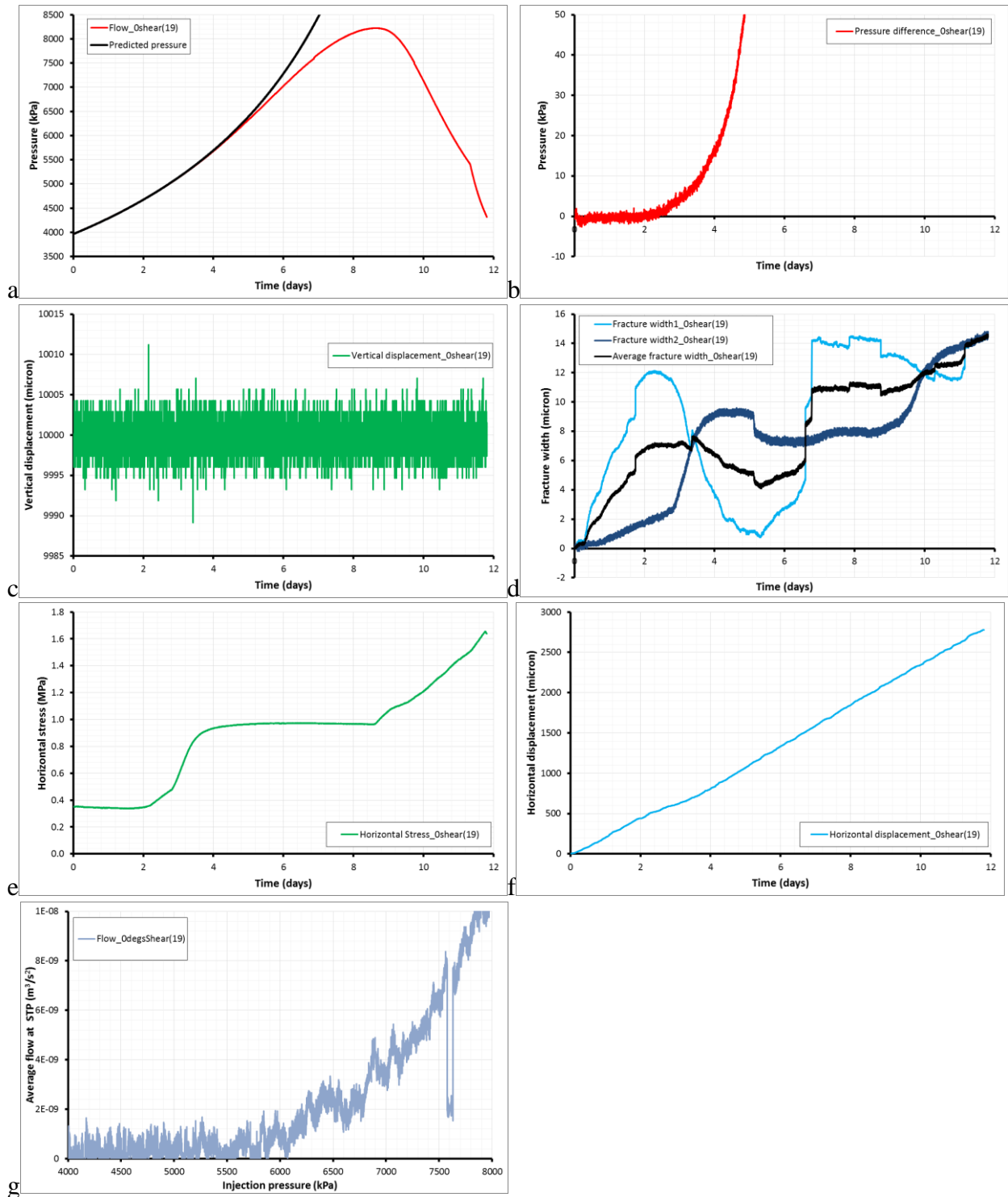


**Figure 58** – Results for gas injection test 19 / ASR\_Tau29\_00gGIS. a) Gas injection pressure compared with prediction from ideal gas law; b) comparison of gas injection and ideal gas law as a way of predicting gas entry pressure; c) normal displacement; d) fracture width; e) horizontal stress; f) shear displacement; g) flow into the slip plane as a way of predicting gas entry pressure.

#### 4.8 COMPARING RESULTS FOR TESTS CONDUCTED ON A SLIP PLANE ORIENTATION OF 0° WITH AND WITHOUT ACTIVE SHEAR

A total of seven gas injection experiments were conducted on a flat slip plane, with two of these being conducted with active shear. As stated previously, each test was performed as identical as possible, with identical water content of gouge produced, similar normal load, similar volumes of gas, and identical gas injection rates. The only parameter that is likely to have varied between tests was the thickness of the gouge at the start of the experiment. However, as best as could be established, this did not vary significantly between tests as the gouge became very thin in all tests.

The results conducted on a slip plane oriented 0° to the shear direction are shown in Figure 59, Figure 60 and Table 14. As seen in Figure 59, horizontal movement had a strong influence on gas transport along the gouge. Both tests conducted during shear reach peak pressure conditions at relatively low pressures compared with non-sheared tests. This suggests that the process of shear enhances transmissivity of the slip-plane. Both tests reached peak pressure and decayed, whereas without shear no pressure decay was observed. Figure 60 and Table 14 show that horizontal movement also reduced the gas entry pressure on average over 2.5 MPa from the estimate determined from STP flow. However, a lesser reduction in gas entry pressure of 0.3 MPa was seen from the estimate of gas entry pressure determined from the ideal gas law. In both methods for determining gas entry pressure a reduction was seen. It was expected that active shear would result in self-sealing. This would result in a raised gas entry pressure and a reduced transmissivity along the slip-plane. The current test results show the opposite with a reduced gas entry pressure and enhanced fracture transmissivity. This suggests that shear is not an effective self-sealing mechanism to gas in kaolinite fault gouges.

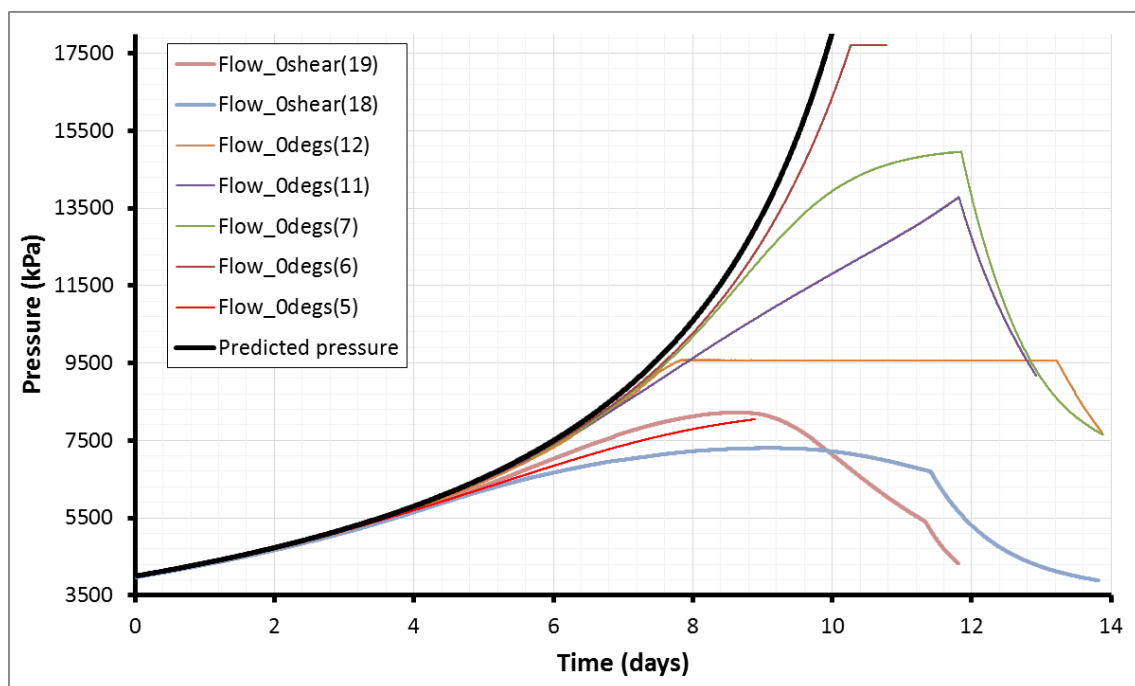


**Figure 59** – Comparing results for gas injection tests conducted on a fracture oriented 0° to the slip plane with and without active shear. Due to the variability seen in gas fracture transmissivity, it is unclear if shear has significantly altered behaviour. It can be seen that the peak pressure appears to be lower.

Test	Fracture angle	+/-	Method 1			Method 2		
			Gas entry pressure (kPa)	Average entry pressure	+/-	Gas entry pressure (kPa)	Average entry pressure	+/-
0degs(5)	0°	0.5°	5000	8440	413	4772	4920	193
0degs(6)			8000			4610		
0degs(7)			9000			4590		
0degs(11)			7500			5475		
0degs(12)			9250			5170		
0Shear(18)	0°@	0.5°	5500	5750	177	4620	4660	28
0Shear(19)			6000			4700		

**Table 14** – Results for gas entry pressure for all gas injection experiments conducted at 0°. @ with shear; Method 1 = gas entry determined from STP gas flow into the fracture; Method 2 = entry pressure inferred from comparing pressure curve with ideal gas law.

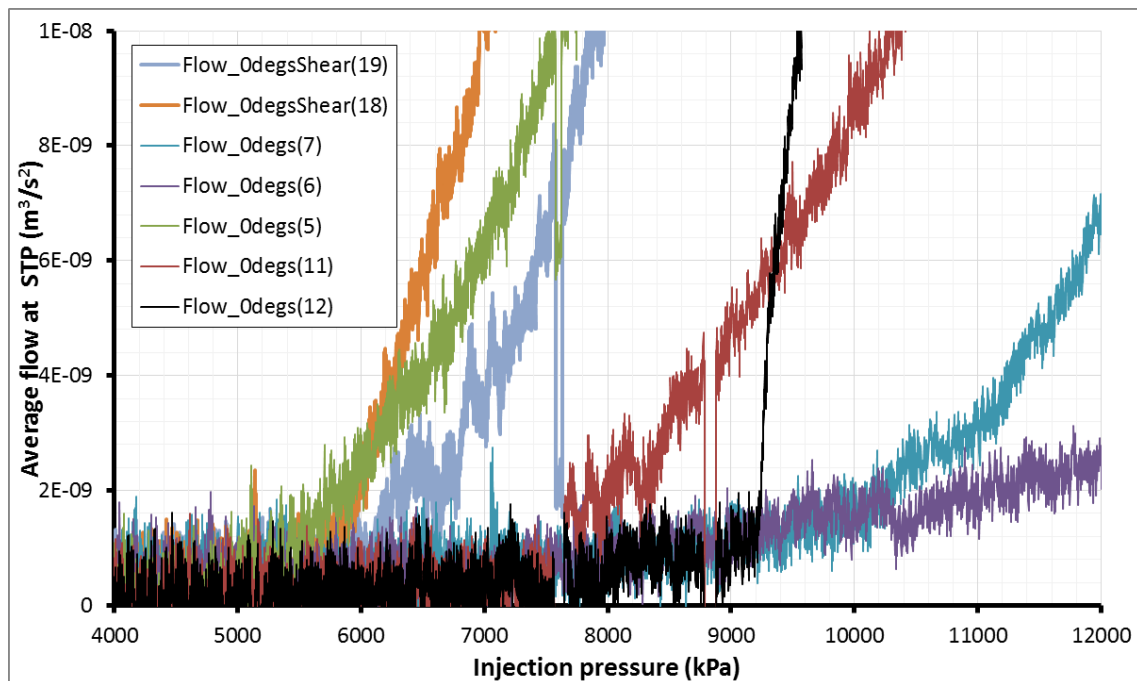


**Figure 60** – Comparing results for gas entry pressure predicted from the average flow at STP for gas injection tests conducted on a fracture oriented 0° to the slip plane with and without active shear. It can be seen that shear has reduced the gas entry pressure, although this is similar in magnitude to the anomalously low entry pressure test (5).

#### 4.8.1 Test ASR\_Tau30\_30gGIS (Gas test 20)

One test was conducted on a fracture oriented 30° to the slip-plane with the addition of shear, namely test ASR\_Tau30\_30gGI; the twentieth gas injection test conducted. The results of the test are summarised in Figure 61. As can be seen in Figure 61a, the gas injection experiment resulted in a maximum gas pressure of approximately 13.5 MPa, with peak pressure not achieved. Following the cessation of gas injection on Day 11, a gas shut-in stage was conducted for one day. An asymptote of pressure would have taken a significant amount of time and so the experiment was halted. The normal displacement data (Figure 61c) suggest that the induction sensor malfunctioned. The eddy current sensors showed a complex history (Figure 61d). Both sensors initially showed dilation, although by day 1 one sensor compressed to about -5  $\mu\text{m}$  and did not change for over 8 days. The other sensor showed continued dilation throughout the test

history. Figure 61e shows the horizontal stress data; this indicated that peak and residual strength correspond and was achieved about Day 3 with a magnitude of 3.5 MPa.

Figure 61b shows the difference between the gas pressure observed and the predicted pressure from the ideal gas law. As seen, this data suggests that gas started to enter the fracture at around Day 3 when the gas pressure was 4,700 kPa. Figure 61e shows the average flow at STP into the fracture, with gas entry inferred to be approximately 7,000 kPa.

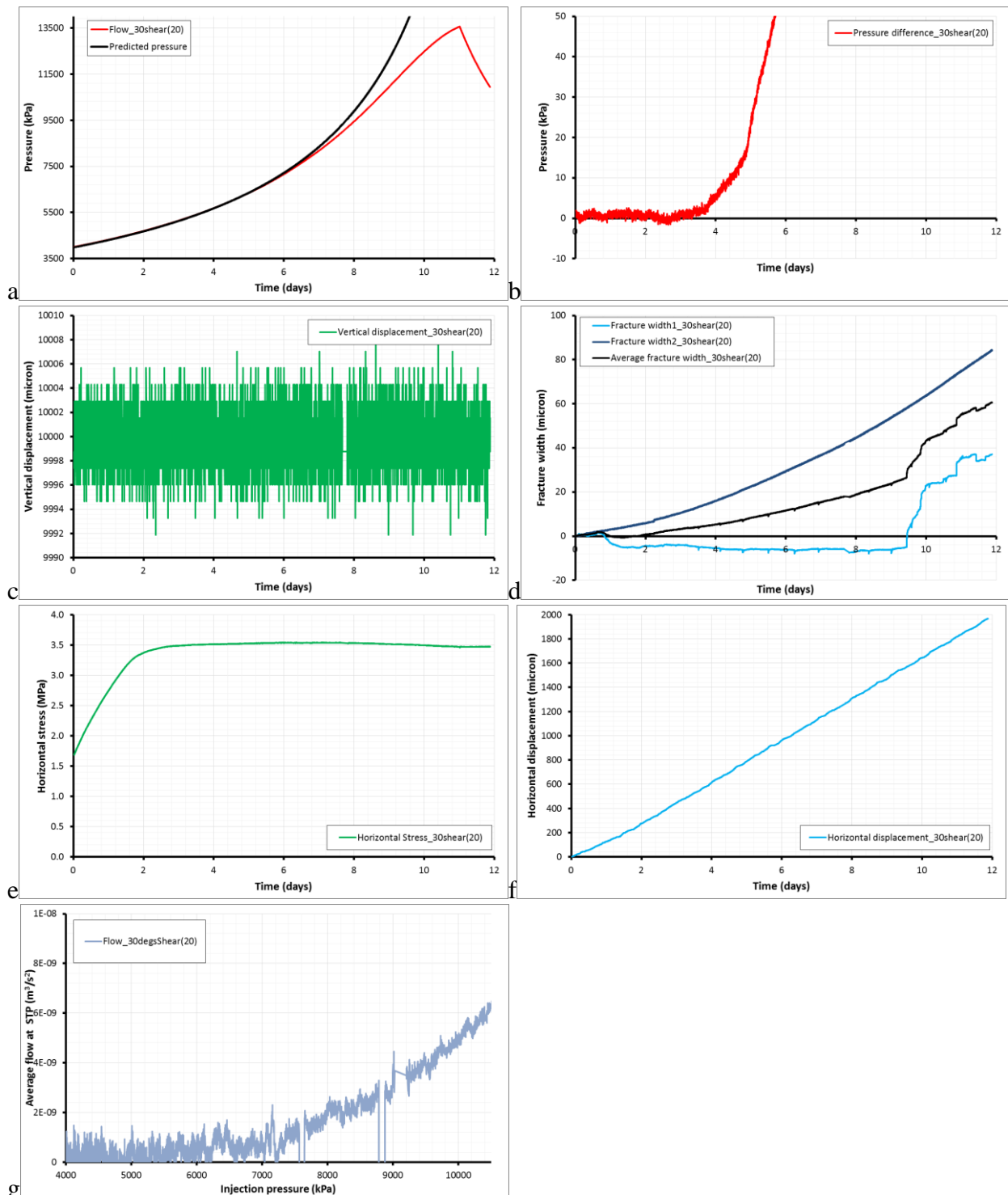


**Figure 61** – Results for gas injection test 20 / ASR\_Tau30\_30gGIS. a) Gas injection pressure compared with prediction from ideal gas law; b) comparison of gas injection and ideal gas law as a way of predicting gas entry pressure; c) normal displacement; d) fracture width; e) horizontal stress; f) shear displacement; g) flow into the slip plane as a way of predicting gas entry pressure.

#### 4.8.2 Test ASR\_Tau31\_45gGIS (Gas test 21)

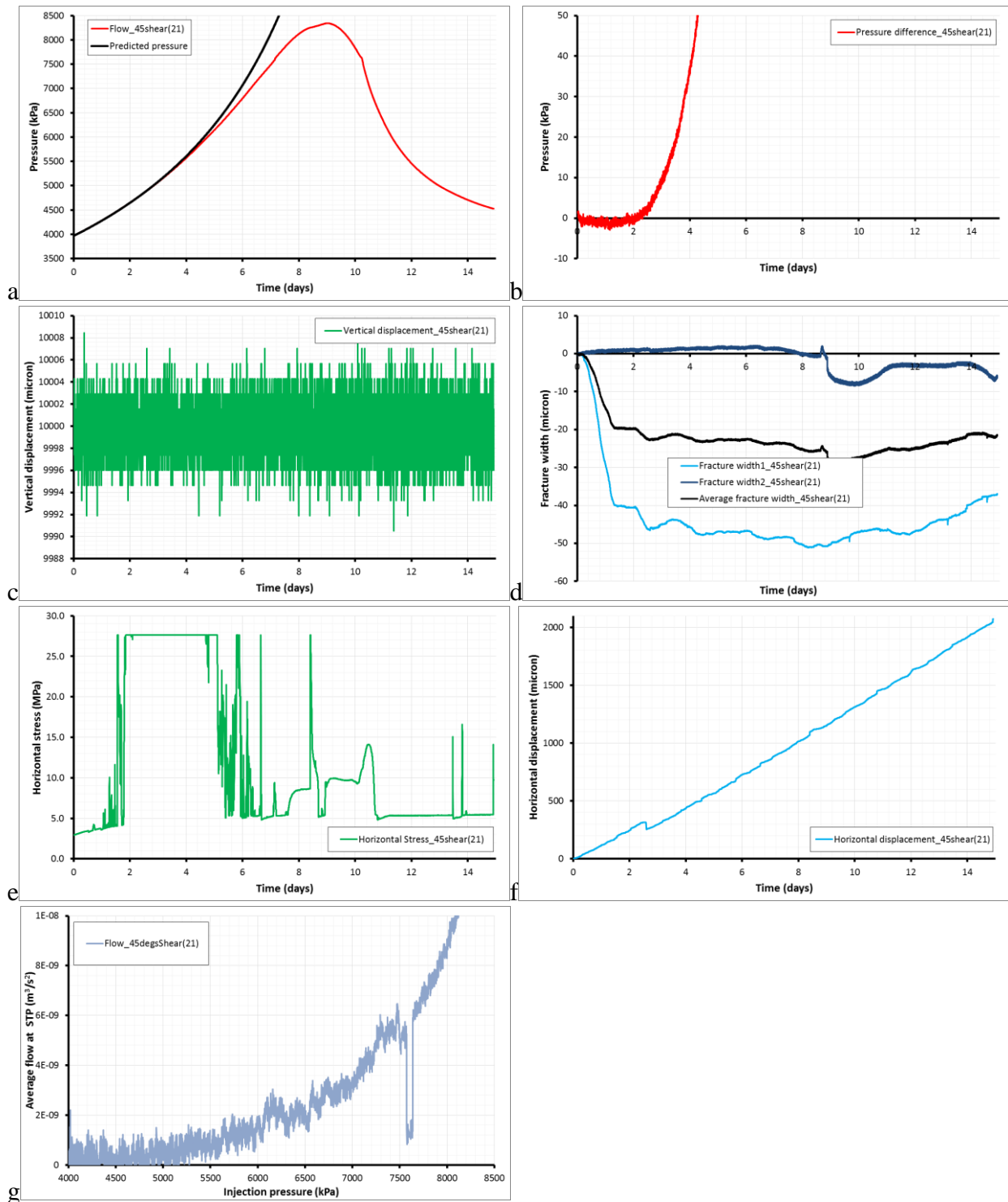
One test was conducted on a fracture oriented  $45^\circ$  to the slip-plane with the addition of shear, namely test ASR\_Tau31\_45gGI; the twenty-first gas injection test conducted. The results of the test are summarised in Figure 62. As can be seen in Figure 62a, the gas injection experiment resulted in a maximum gas pressure of approximately 8.5 MPa, with peak pressure achieved and a drop of approximately 1 MPa by the time shear was stopped on Day 10. Following the cessation of gas injection the pressure was allowed to decay and suggests that pressure would asymptote at approximately 4 MPa. The normal displacement data (Figure 62c) suggest that the induction sensor malfunctioned. The eddy current sensors showed a complex history (Figure 62d). One sensor showed small ( $< 2 \mu\text{m}$ ) dilation, with compression occurring approximately day 9 when peak pressure was achieved. The other sensor showed considerable compression of about  $50 \mu\text{m}$  with dilation occurring the time of peak pressure. Therefore at peak gas pressure the top block “rocked” and gas migrated along the slip-plane. Figure 62e shows the horizontal stress data and indicates that something was faulty with the shear load cell.

Figure 62b shows the difference between the gas pressure observed and the predicted pressure from the ideal gas law. As seen, this data suggests that gas started to enter the fracture at around Day 2 when the gas pressure was 4,450 kPa. Figure 62e shows the average flow at STP into the fracture, with gas entry inferred to be approximately 5,000 kPa.

#### 4.8.3 Test ASR\_Tau32\_15gGIS (Gas test 22)

One test was conducted on a fracture oriented  $15^\circ$  to the slip-plane with the addition of shear, namely test ASR\_Tau32\_15gGI; the twenty-second gas injection test conducted. The results of the test are summarised in Figure 63. As can be seen in Figure 63a, the gas injection experiment resulted in a maximum gas pressure of approximately 11 MPa. Shear was stopped on Day 12 soon after peak pressure had been achieved and a drop of about 0.5 MPa to a residual pressure of approximately 10 MPa occurred. However, approximately Day 14 all gas pressure was lost in an instantaneous enhanced gas breakthrough event. The normal displacement data (Figure 63c) suggests that the induction sensor malfunctioned. The eddy current sensors showed a complex history (Figure 63d). One sensor initially showed dilation, followed on Day 1 by compression of approximately  $5 \mu\text{m}$ . The other sensor showed much greater compression of about  $27 \mu\text{m}$ . No correlation is seen in the flow data and the eddy current sensor data. Figure 63e shows the horizontal stress data and indicates that the shear load cell was faulty.

Figure 63b shows the difference between the gas pressure observed and the predicted pressure from the ideal gas law. As seen, this data suggests that gas started to enter the fracture at around Day 2.5 when the gas pressure was 4,830 kPa. Figure 63e shows the average flow at STP into the fracture, with gas entry inferred to be approximately 5,250 kPa.



**Figure 62** – Results for gas injection test 21 / ASR\_Tau31\_45gGIS. a) Gas injection pressure compared with prediction from ideal gas law; b) comparison of gas injection and ideal gas law as a way of predicting gas entry pressure; c) normal displacement; d) fracture width; e) horizontal stress [note malfunction]; f) shear displacement; g) flow into the slip plane as a way of predicting gas entry pressure.

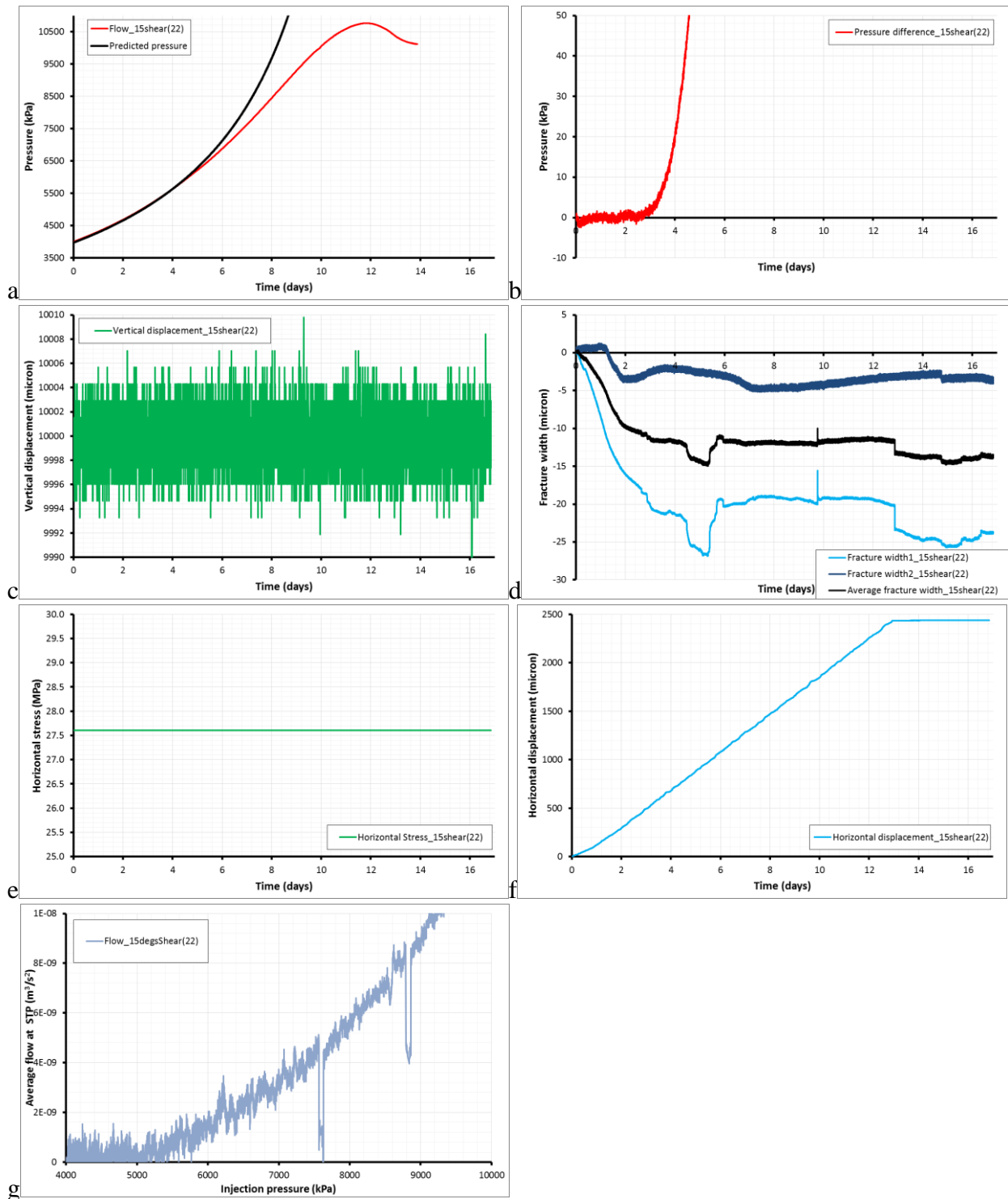


**Figure 63** – Results for gas injection test 22 / ASR\_Tau32\_15gGIS. a) Gas injection pressure compared with prediction from ideal gas law; b) comparison of gas injection and ideal gas law as a way of predicting gas entry pressure; c) normal displacement; d) fracture width; e) horizontal stress [note malfunction]; f) shear displacement; g) flow into the slip plane as a way of predicting gas entry pressure.

#### 4.8.4 Results for tests conducted with active shear

A total of five gas injection experiments were conducted at different angles with active shear. As stated previously, each test was performed as identical as possible, with identical water content of gouge produced, similar normal load, similar volumes of gas, and identical gas injection rates. The only parameter that is likely to have varied between tests was the thickness of the gouge at

the start of the experiment. However, as best as could be established, this did not vary significantly between tests as the gouge became very thin in all tests.

The results conducted on a slip planes oriented between 0° and 45° to the shear direction are shown in Figure 64, Figure 65 and Table 15. As seen in Figure 64, horizontal movement has resulted in all bar one test to achieve gas peak pressure. Figure 65 shows the influence of shear on the gas entry pressure at different fracture angles. As can be seen in Figure 65a, gas entry pressure ranges from 5 to 5.8 MPa. The polynomial fit achieved by the data suggest that a minimum in gas entry pressure occurred at approximately 37°; therefore shear has resulted in the minimum gas pressure orientation increasing. Figure 65b shows the influence of shear on the gas entry pressure. As can be seen, shear has generally resulted in a 2.5 MPa reduction in gas entry pressure. It was expected that shear would have been an effective self-sealing mechanism and that gas entry pressure would increase. However, the data show that gas finds it easier to enter a slip-plane that is shearing and is more mobile. Figure 65c shows the data for gas entry pressure determined from the ideal gas law. This has a dissimilar form with a maximum gas entry pressure at 15° and a minimum at 45°. This may reflect the difficulty in determining gas entry pressure from this method.

Test	Fracture angle	+/-	Method 1			Method 2		
			Gas entry pressure (kPa)	Average entry pressure	+/-	Gas entry pressure (kPa)	Average entry pressure	+/-
0Shear(18)	0°@	0.5°	5500	5750	177	4620	4660	28
0Shear(19)			6000			4700		
30Shear(20)	30°@	0.5°	7000	7000	100	4700	4700	100
45Shear(21)	45°@	0.5°	5000	5000	100	4450	4450	100
15Shear(22)	15°@	0.5°	5250	5200	100	4830	4830	100

**Table 15** – Results for gas entry pressure for all gas injection experiments. # high pressurisation rate; @ with shear; Method 1 = gas entry determined from STP gas flow into the fracture; Method 2 = entry pressure inferred from comparing pressure curve with ideal gas law.

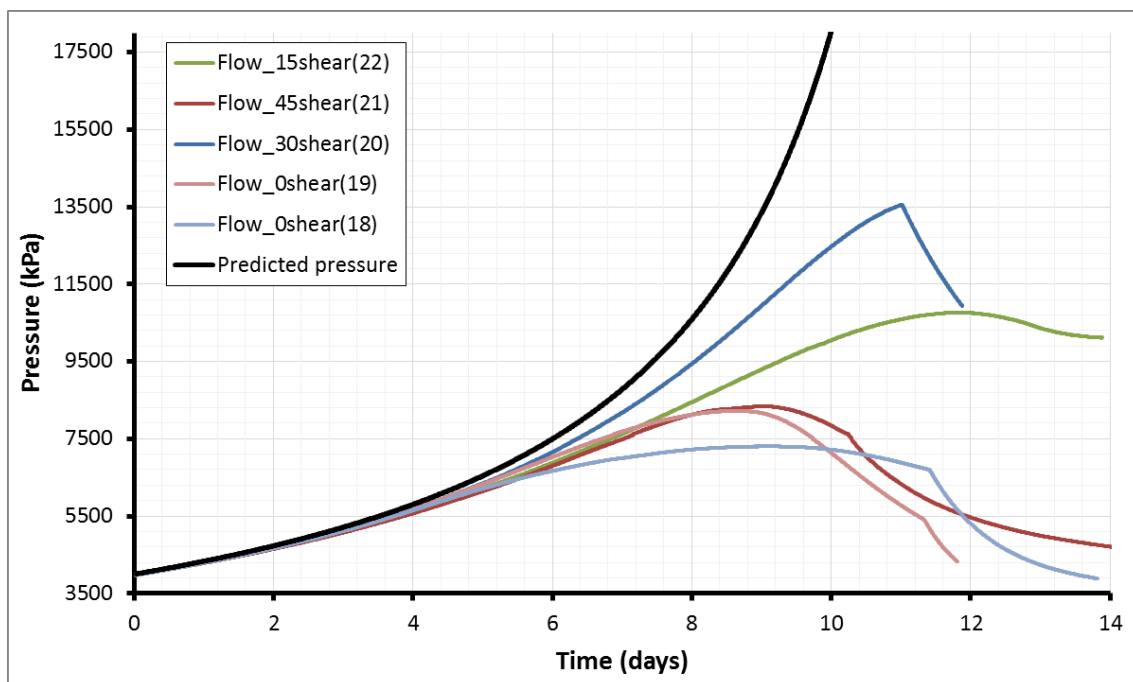


**Figure 64** –Results for five gas injection tests conducted with active shear. As can be seen, considerable differences are seen in peak pressure and form of the curve indicating that fracture transmissivity is not repeatable.

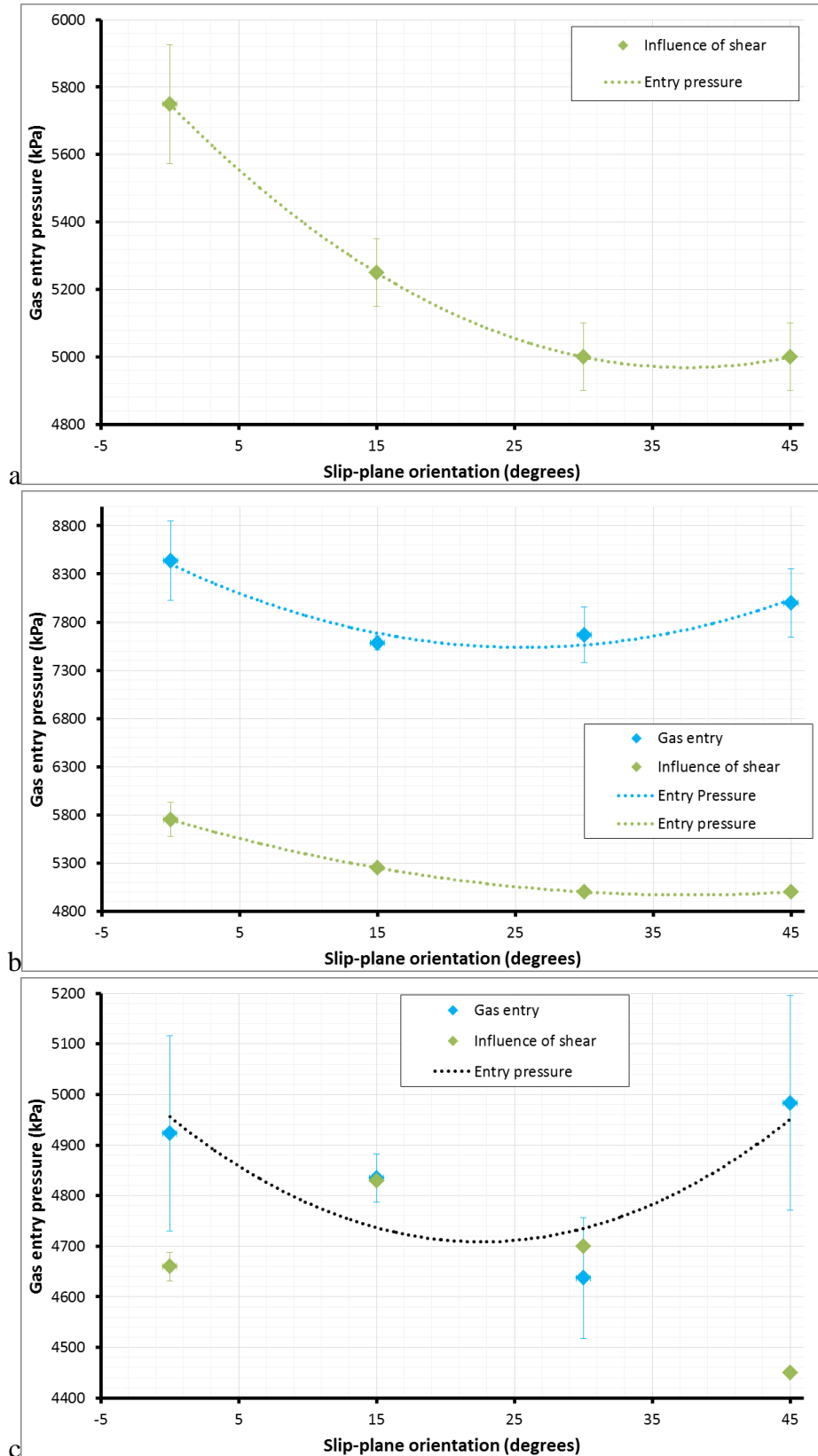


**Figure 65** – Gas entry pressure for all tests showing the influence of shear. a) gas entry determined from the STP gas flow into the fracture. This shows that shear greatly reduces entry pressure; b) gas entry determined from comparing pressure response with ideal gas law. This suggests that shear does not significantly alter entry pressure.

## 4.9 THE EFFECT OF RATE OF PRESSURISATION ON GAS ENTRY AND SUBSEQUENT GAS FLOW

Two gas injection experiments were conducted with an increased rate of pressurisation in order to investigate whether gas entry pressure and gas peak pressure are rate dependent. As stated previously, each test was performed as identical as possible, with identical water content of gouge produced, similar normal load, and similar volumes of gas. The only parameter that is likely to have varied between tests was the thickness of the gouge at the start of the experiment. However, as best as could be established, this did not vary significantly between tests as the gouge became very thin in all tests. Therefore the two experiments conducted only varied by their pressurisation rate.

### 4.9.1 Test ASR\_Tau23\_00gGI (Gas test 13)

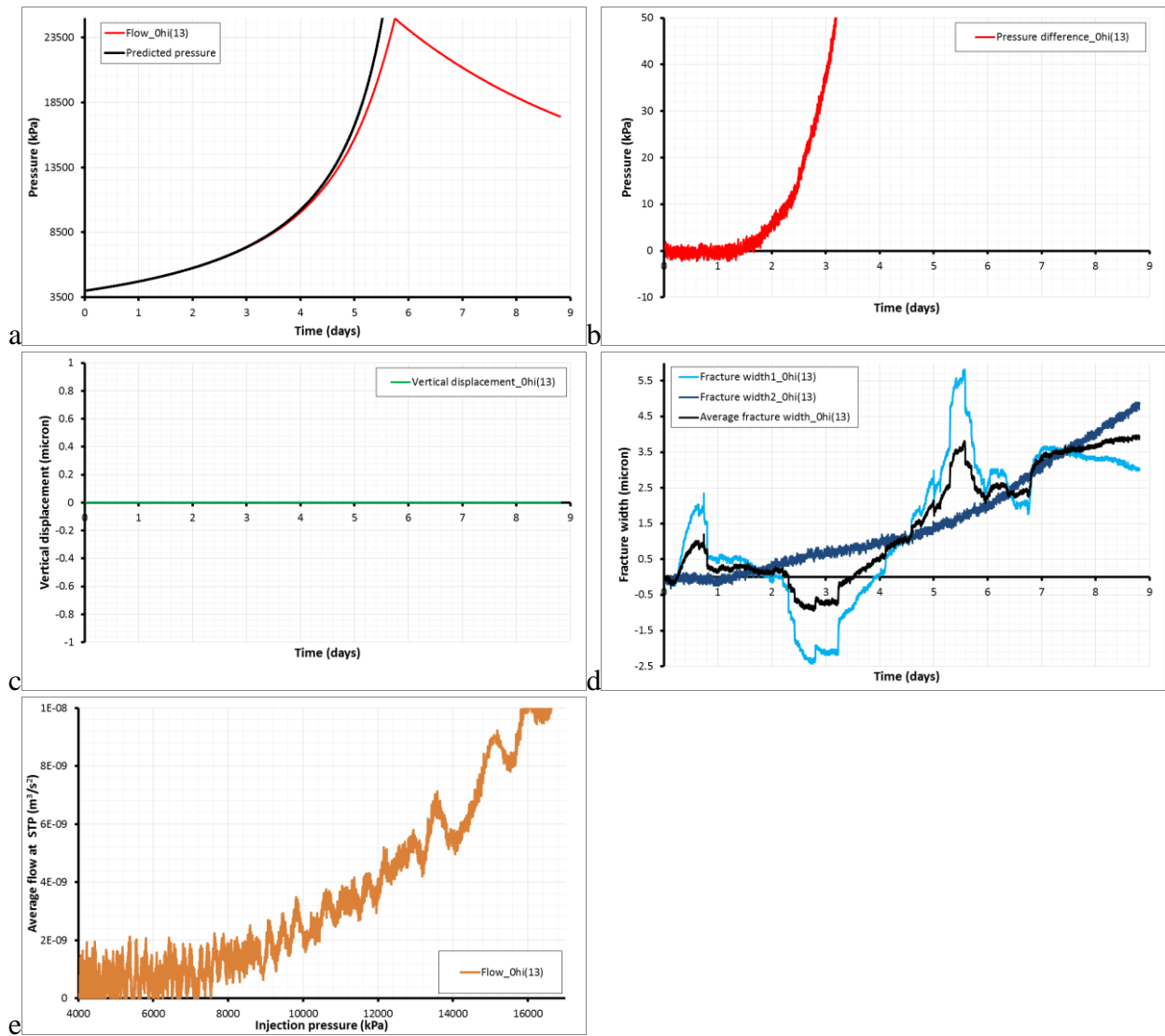
The first gas injection test conducted at an increased gas injection rate was test ASR\_Tau23\_00gGI; the thirteenth gas injection test conducted. The results of the test are summarised in Figure 66. As can be seen in Figure 66a, the gas injection experiment resulted in a maximum gas pressure in excess of 24 MPa, the limit of the gas injection ISCO syringe pumps. Following the cessation of gas injection on Day 5, a gas shut-in stage was conducted for three days. An asymptote of pressure would have taken a significant amount of time and so the experiment was halted. The normal displacement data (Figure 66c) suggest that the induction sensor malfunctioned. The eddy current sensors showed a complex history (Figure 66d). One sensor showed no variation for one day, followed by slow dilation that reached a maximum of 4.8  $\mu\text{m}$  by Day 9. It has to be noted that no change was seen to the change in dilation when gas injection was stopped. The other eddy-current sensor showed an initial dilation of 2  $\mu\text{m}$ , followed by a contraction between Day 2 and 3, followed by dilation. No correlation could be seen between the eddy current sensor data and the onset of gas flow inferred from the ideal gas law (Figure 66b).

Figure 66b shows the difference between the gas pressure observed and the predicted pressure from the ideal gas law. As seen, these data suggests that gas started to enter the fracture at around Day 1.5 when the gas pressure was 4,845 kPa. Figure 66e shows the average flow at STP into the fracture, with gas entry inferred to be approximately 7,000 kPa.

### 4.9.2 Test ASR\_Tau24\_00gGI (Gas test 14)

The second gas injection test conducted at an increased gas injection rate was test ASR\_Tau24\_00gGI; the fourteenth gas injection test conducted. The results of the test are summarised in Figure 67. As can be seen in Figure 67a, the gas injection experiment resulted in a maximum gas pressure in excess of 24 MPa, the limit of the gas injection ISCO syringe pumps. Following the cessation of gas injection on Day 5, a gas shut-in stage was conducted for six days. An asymptote of pressure was nearly achieved and suggests an asymptote at 4 MPa. The normal displacement data (Figure 67c) suggest that the induction sensor malfunctioned. The eddy current sensors showed a complex history (Figure 67d). Both sensors generally showed dilation with episodes of contraction. No correlation could be seen between the eddy current sensor data and the onset of gas flow inferred from the ideal gas law (Figure 67b).

Figure 67b shows the difference between the gas pressure observed and the predicted pressure from the ideal gas law. As seen, these data suggests that gas started to enter the fracture at around Day 2.5 when the gas pressure was 6,000 kPa. Figure 67e shows the average flow at STP into the fracture, with gas entry inferred to be approximately 8,000 kPa.



**Figure 66** – Results for gas injection test 13 / ASR\_Tau23\_00gGI. a) Gas injection pressure compared with prediction from ideal gas law; b) comparison of gas injection and ideal gas law as a way of predicting gas entry pressure; c) normal displacement [note malfunction]; d) fracture width; e) flow into the slip plane as a way of predicting gas entry pressure.

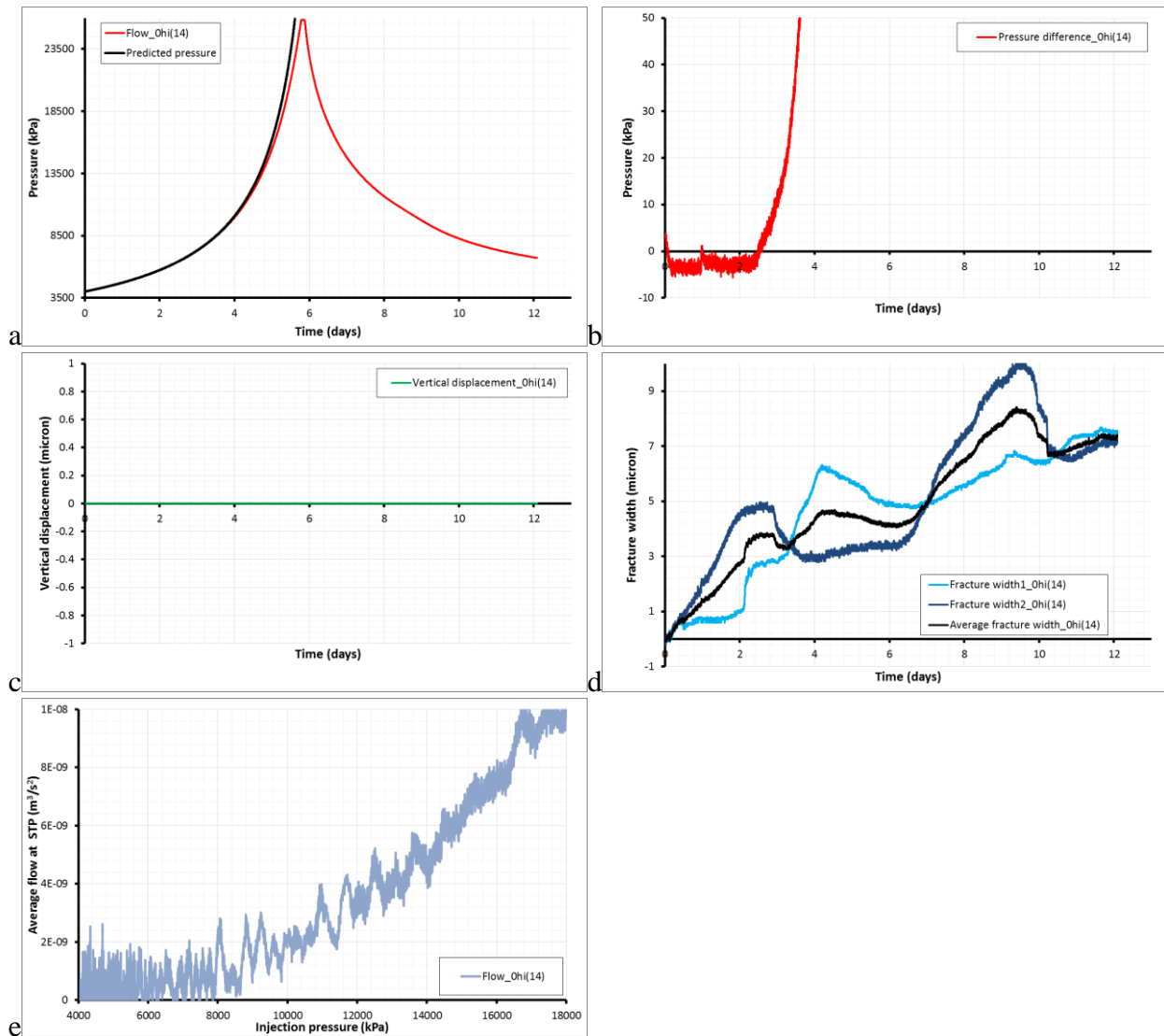


**Figure 67** – Results for gas injection test 14 / ASR\_Tau24\_00gGI. a) Gas injection pressure compared with prediction from ideal gas law; b) comparison of gas injection and ideal gas law as a way of predicting gas entry pressure; c) normal displacement [note malfunction]; d) fracture width; e) flow into the slip plane as a way of predicting gas entry pressure.

#### 4.10 RESULTS FOR TESTS CONDUCTED AT INCREASED INJECTION RATE

Only two tests were conducted with an increased gas injection rate and both tests showed similar general results. As stated previously, each test was performed as identical as possible, with identical water content of gouge produced, similar normal load, and similar volumes of gas. The only parameters that were likely to have varied between tests were the thickness of the gouge at the start of the experiment and the change in gas injection rate. However, as best as could be established, gouge thickness did not vary significantly between tests as the gouge became very thin in all tests.

The results conducted on a slip planes oriented at  $0^\circ$  with an increased gas injection rate are shown in Figure 68, Figure 69, and Table 16. As seen in Figure 68, an increased gas injection rate significantly altered the gas response of the gouge; with significantly higher gas pressure achieved in excess of 24 MPa. Neither test showed signs of reaching peak pressure behaviour.

Figure 69 and Table 16 show that both tests had similar gas entry pressure when determined from STP flow, which also corresponded with the gas entry pressure for all other tests conducted. This suggests that the rate of pressurisation was not influencing gas entry pressure.

However, the entry pressure determined from the ideal gas law for one test suggests that gas entry pressure was slightly raised. Given the significant change in peak pressure achieved, no significant change in gas entry pressure occurred. Figure 70 and Table 16 show the influence of increased gas pressurisation on the gas entry pressure. As can be seen in Figure 70a, gas entry pressure results in a minor reduction in gas entry pressure from 8.4 to 7.5 MPa when estimated from STP gas flow into the fracture. However, as seen in Figure 70b, determining gas entry pressure from the ideal gas law showed an increase in gas entry pressure from 4.9 to 5.4 MPa. Therefore it is concluded that gas entry pressure is not a rate dependent variable.

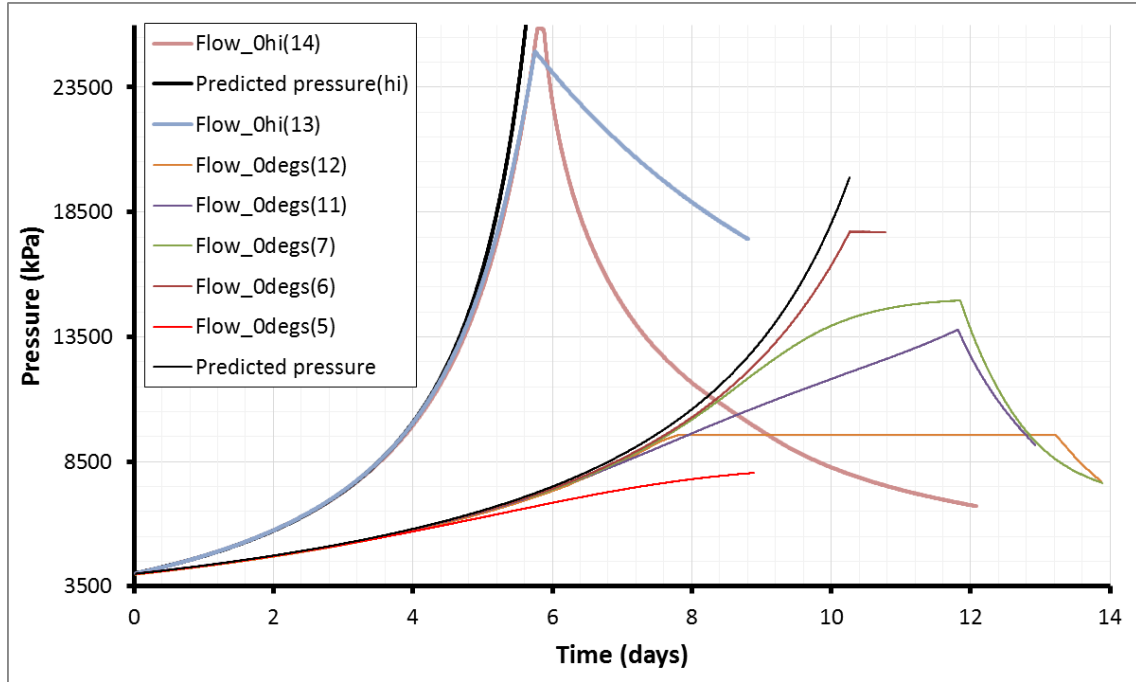


**Figure 68** – Results for two gas injection tests conducted at higher gas injection rates, compared with five tests conducted on a fracture oriented 0° to the slip plane. As can be seen, considerable higher gas pressures were achieved.

Test	Fracture angle	+/-	Method 1			Method 2		
			Gas entry pressure (kPa)	Average entry pressure	+/-	Gas entry pressure (kPa)	Average entry pressure	+/-
0degs(5)	0°	0.5°	5000	8440	413	4772	4920	193
0degs(6)			8000			4610		
0degs(7)			9000			4590		
0degs(11)			7500			5475		
0degs(12)			9250			5170		
0hi(13)	0°#	0.5°	7000	7500	354	4845	5420	408
0hi(14)			8000			6000		

**Table 16** – Results for gas entry pressure for all gas injection experiments. # high pressurisation rate; @ with shear; Method 1 = gas entry determined from STP gas flow into the fracture; Method 2 = entry pressure inferred from comparing pressure curve with ideal gas law.

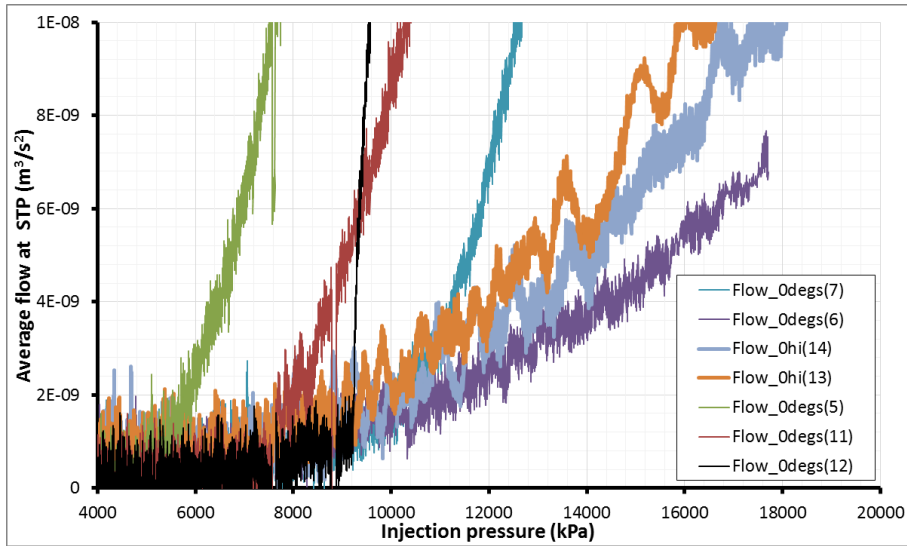


**Figure 69** – Gas entry pressure predicted from the average flow at STP for two tests conducted at higher gas injection rate, compared with five gas injection tests conducted on a fracture oriented 0° to the slip plane. As can be seen, repeatable gas entry pressure is seen for all tests, suggesting that injection rate does not alter gas entry pressure.

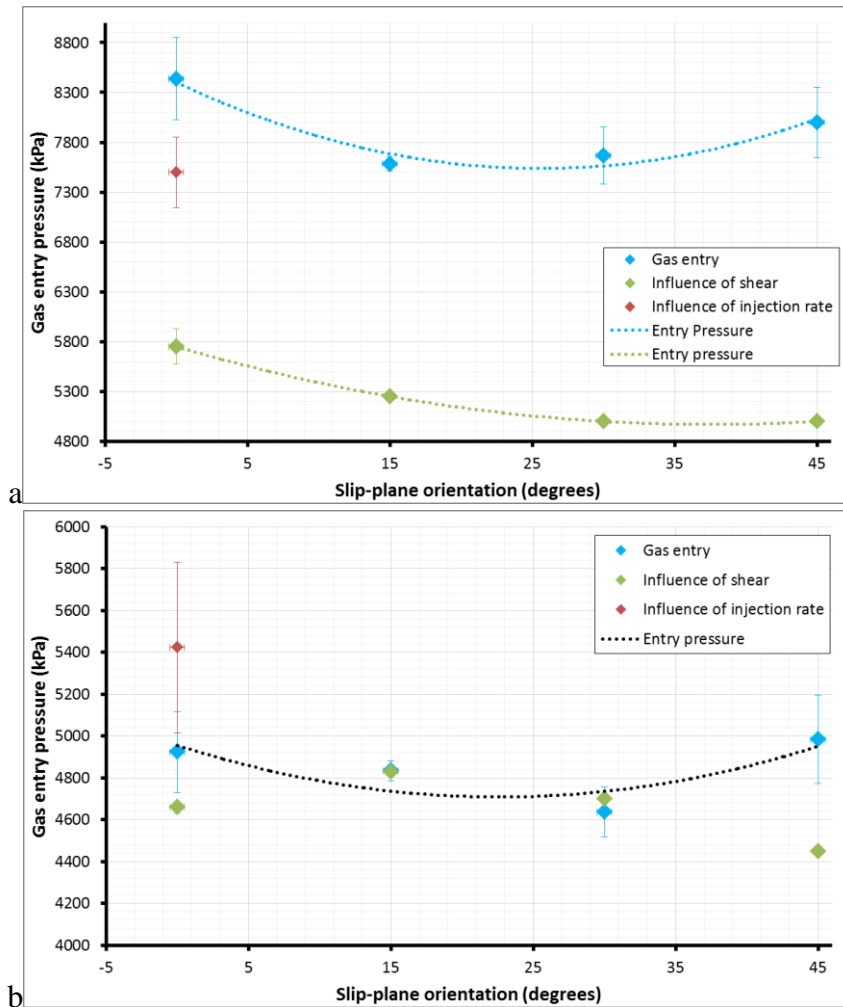


**Figure 70** – Gas entry pressure for all tests showing the influence of gas injection rate. a) gas entry determined from the STP gas flow into the fracture; b) gas entry determined from comparing pressure response with ideal gas law.

#### 4.11 IS GAS ENTRY AT DIFFERENT ANGLES SIMPLY RELATED TO NORMAL LOAD?

As shown in Section 3.1, fracture transmissivity is a function of vertical load. All gas injection experiments were conducted with identical boundary conditions with the loading system set to give 2 MPa on the fracture oriented at 0° to the slip-plane. However, the loading of the gouge perpendicular to the fracture angle would therefore differ depending on the fracture angle. As can be seen in Figure 71, the loading frame results in a normal load on the fracture of 2 MPa when the fracture is flat, reducing to a low of about 1.4 MPa when the fracture is 45°. If the change in gas entry pressure seen was simply due to changes in normal load on the fracture as a result of fracture angle it would be expected that a similar form would be seen in the relationship of both normal load and flow; which is clearly not the case in Figure 71a and Figure 71b. Therefore, although fracture transmissivity was seen to be a function of vertical load, the variation seen in gas entry pressure is not as a result of simple stress rotation about the fracture and must therefore be related to the horizontal stress generated within the fault gouge.

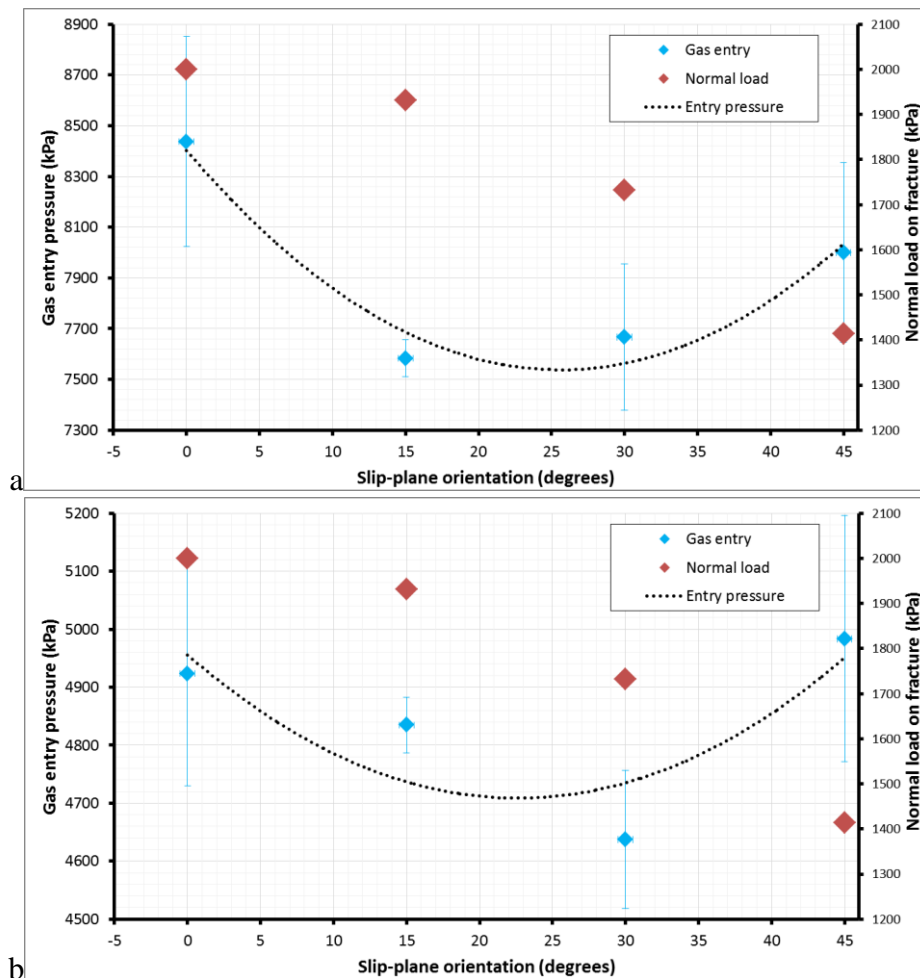


**Figure 71** – Comparing gas entry pressure with normal load on the fracture; a) gas entry pressure determined from STP flow into the fracture; b) gas entry pressure determined from ideal gas law. As can be seen, the variation in gas entry pressure cannot be explained from the variation of normal load with fracture orientation alone.

## 5 Time-lapse study of fracture flow

Five gas injection tests were conducted with the addition of time-lapse photography in order to identify the time of gas escaping the kaolinite gouge. Two GoPro HD Hero2 cameras were mounted on the apparatus and set to take a photograph every 30 seconds during the gas injection test. The photographs were assembled into time-lapse films, allowing an approximate time of bubbles appearing to be identified. The jpeg images were then examined in order to get a better time for the first appearance of gas bubbles.

### 5.1.1 Time-lapse test 1 (Test ASR\_Tau20\_15gGI; Gas test 10)

Close examination of the time-lapse images did not show any bubbles escaping the kaolinite gouge. The first time-lapse test was conducted with a single GoPro HD Hero 2 camera and it was decided to perform all subsequent tests using two cameras in order to observe more of the kaolinite gouge area. Figure 40 shows that gas peak pressure was close to being achieved and therefore gas was mobile within the gouge. Therefore it is possible that gas was escaping from a location not covered by the camera.

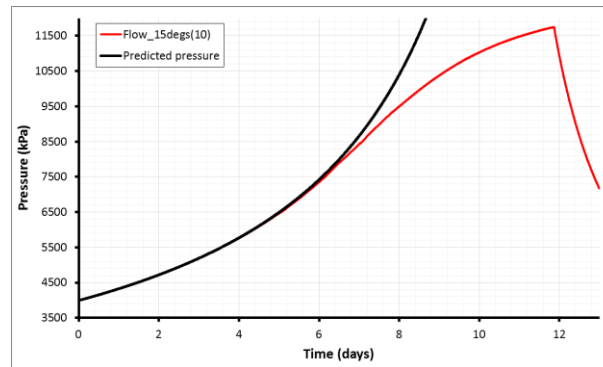


**Figure 72** – Time-lapse results for gas injection test 10 / ASR\_Tau20\_15gGI.

### 5.1.2 Time-lapse test 2 (Test ASR\_Tau21\_00gGI; Gas test 11)

Gas bubbles were identified in the second time-lapse test conducted. Gas initially started as isolated bubbles from a single exit point, which in time developed into a large stream of gas by the end of the test. The first identifiable bubble was seen at 20:12 on the 7/5/2012 when gas pressure was at 7,500 kPa (see Figure 73). This corresponds with the gas entry pressure identified from average flow at STP into the fracture (7,500 kPa), but is higher than the gas entry pressure predicted from the ideal gas law (5,475 kPa).

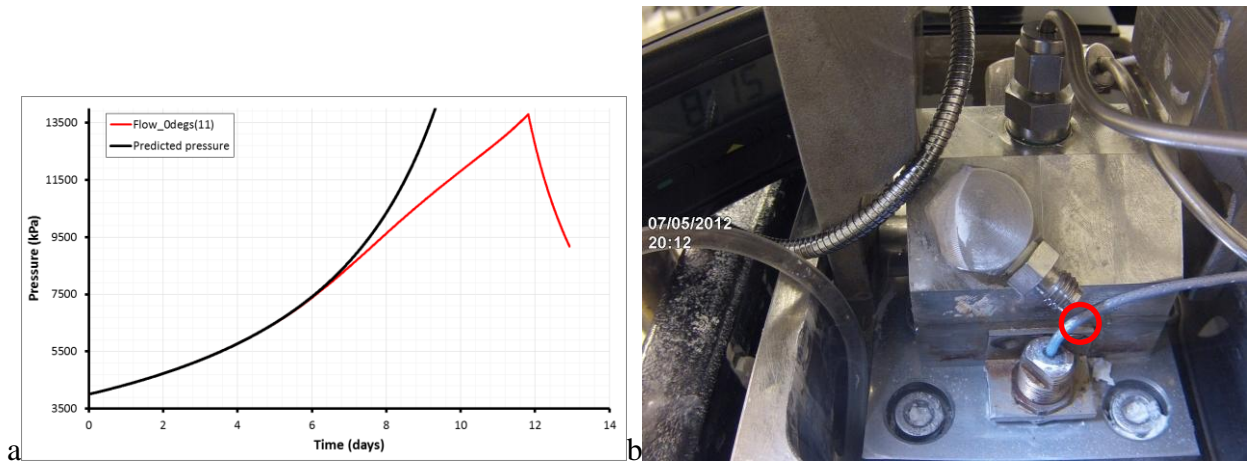


**Figure 73** – Time-lapse results for gas injection test 11 / ASR\_Tau21\_00gGI. a) Gas injection pressure compared with prediction from the ideal gas law; b) Photo showing first identifiable bubble coming from the kaolinite gouge.

**5.1.3 Time-lapse test 3 (Test ASR\_Tau22\_00gGI; Gas test 12)**

Gas bubbles were identified in the third time-lapse test conducted. This initially started as bubbles from a single exit point, which developed into a large stream of gas by the end of the test. The first identifiable bubble was seen at 02:51 on the 22/5/2012 when gas pressure was at 9,200 kPa (see Figure 74). This corresponds with the gas entry pressure identified from average flow at STP into the fracture (9,250 kPa), but is higher than the gas entry pressure predicted from the ideal gas law (5,170 kPa).



**Figure 74** – Time-lapse results for gas injection test 12 / ASR\_Tau22\_00g GI. a) Gas injection pressure compared with prediction from ideal gas law; b) Photo showing first identifiable bubble coming from the kaolinite gouge.

**5.1.4 Time-lapse test 4 (Test ASR\_Tau23\_00gGI; Gas test 13)**

Gas bubbles were not observed in the fourth time-lapse test conducted, despite near full coverage of the kaolinite gouge by the time-lapse cameras. It is possible that gas may have been escaping out of camera view. However, no signs of bubbles disturbing the water surface were seen. Figure 75 shows that by the end of the test the observed gas pressure was close to the predicted gas pressure. This suggests that little gas had been mobilised and may explain why no gas bubbles were observed. Therefore it is concluded that gas was only mobile within the gouge and had failed to exit the test sample.

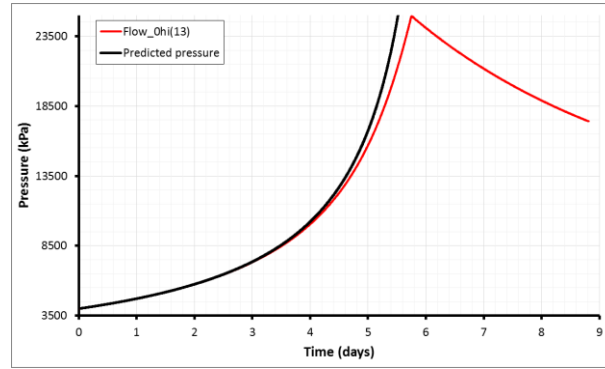


**Figure 75** – Time-lapse results for gas injection test 13 / ASR\_Tau23\_00g GI. Gas injection pressure compared with prediction from ideal gas law.

### 5.1.5 Time-lapse test 5 (Test ASR\_Tau24\_00gGI; Gas test 14)

Gas bubbles were identified in the fifth time-lapse test conducted. This initially started as bubbles from a single exit point, which developed into a large stream of gas from two separate locations. The first identifiable bubble was seen at 21:05 on the 11/6/2012 when gas pressure was at 17,000 kPa (see Figure 76). This pressure was significantly higher than the gas entry pressure identified from average flow at STP into the fracture (8,000 kPa) and the gas entry pressure predicted from the ideal gas law (6,000 kPa).

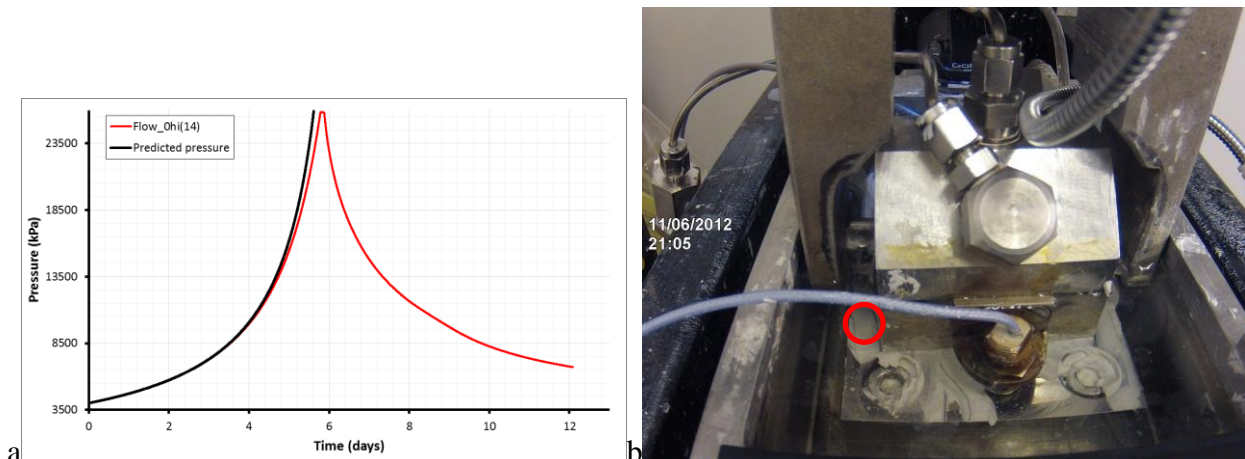


**Figure 76** – Time-lapse results for gas injection test 12 / ASR\_Tau22\_00g GI. a) Gas injection pressure compared with prediction from ideal gas law; b) Photo showing first identifiable bubble coming from the kaolinite gouge.

## 5.2 DISCUSSION ON TIME-LAPSE OBSERVATIONS

Of the five time-lapse tests conducted only three had observable gas bubbles escaping the kaolinite gouge. For two of these tests the pressure at which the first bubble was identified corresponds closely with the gas entry pressure predicted from average flow at STP into the fracture. Therefore it is possible that this technique identifies the gas breakthrough pressure (the pressure when gas is sufficient to allow escape from the sample). However, one test showed gas bubbles did not appear until a pressure greatly in excess of predicted gas entry. This test showed that observed gas pressure was close to predicted gas pressure, suggesting that little gas had entered the gouge.

Two tests did not observe gas bubbles. The first test may be as a result of limited camera coverage of the kaolinite gouge. The second test displayed a gas pressure close to the predicted pressure, indicating that little gas had entered the gouge and by the end of the test this gas had not migrated as far as the outside of the kaolinite gouge.

Two tests showed that gas migrated and exited the gouge at a single point, suggesting only one pathway had allowed gas escape. However, one test showed that gas initially escaped from a single location, which soon sealed and gas then escaped from two other locations diametrically opposed on the loading platen. This suggests that multiple pathways formed and continued to evolve even once gas was able to escape the system.

## 6 Water content of the gouge material

During the decommissioning of test ASR\_Tau08\_30gLU, five sub-samples of kaolinite gouge were taken and water content was determined. This was performed by weighing the samples before and after oven drying for 24 hours. All test materials were started with an initial water content of 80%. As shown in Figure 77, water content was greatly reduced. It is likely that water would have been driven off during normal loading. It can be seen that variation is seen in the final water content. Along the centre of the sample water content appears more reduced than on the left or right of the slip-plane. However, only small quantities of kaolinite were recovered, typically 0.01 – 0.02 g for each sample and therefore considerable error could be introduced by measuring such small samples.

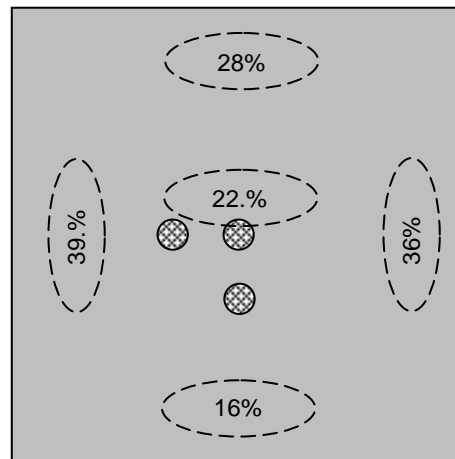


**Figure 77** – Water content of the kaolinite gouge material measured at five locations on the sample surface.

## 7 Conclusions

The complete experimental programme conducted 48 separate experiments. Two main types of experiment were conducted: 1). Loading-unloading tests, where fracture flow was monitored at constant injection pressure as normal load was increased in steps to a given level and then reduced back to the starting stress state; 2). Gas breakthrough experiments, where gas injection pressure was increased in a pressure ramp at constant normal load. These were conducted with and without active shear. In addition, a number of other experiments were conducted. The main conclusions from this study are summarised below:

### 7.1 LOADING-UNLOADING TESTS

A total of 17 loading-unloading experiments were conducted, all on a 30° slip-plane. Nine tests were conducted without a permeant in order to understand the behaviour of the kaolinite gouge whilst loading/unloading, five tests were conducted with water as the injection fluid, whilst three gas flow experiments were conducted.

**During a loading (vertical stress) and unloading cycle considerable hysteresis in flow was observed signifying the importance of stress history on fracture flow.**

As normal load was increased in steps, the flow along the slip plane steadily reduced. Tests initially may have had dissimilar flow rates to start, but generally achieved a similar flow rate of by 2.6 MPa normal load. On unloading, this flowrate did not significantly alter until normal loads of approximately 0.75 MPa. Therefore it can be noted that the “memory” of the maximum load experienced is retained. This illustrates the importance of stress history on predicting flow along discontinuities and has been used to explain the non-applicability of the critical stress approach in its simple form at the Sellafield site in the UK (Sathar *et al.*, 2012). All loading-unloading experiments showed marked hysteresis in flow.

**For the case of gas injection the change in flow is chaotic at low normal loads, whereas for water injection the flow reduces smoothly with increased normal load.**

Considerable difference is seen between the loading and unloading cycles during gas flow. On loading the progression of flow is chaotic. In all three tests, once normal load was increased from the starting value of approximately 0.3 to 0.5 MPa flow increases. All three tests show that increased normal load results in episodes of increasing and decreasing flow. This could possibly be explained by 3 possible mechanisms:

1. Gas flow is highly sensitive to water content of the gouge and the duration of the experiment means that full drainage is not possible;
2. The gouge is not remaining even in thickness along the complete length, i.e. increased load is resulting in a wedge shaped gouge;
3. Horizontal movement is occurring along the 30° slope as normal load is increased and there is some form of stick-slip, which means that the movement is uneven between steps.

It is difficult to rule out scenario (1) as this has not been investigated fully. However, wide variation in flow rates have not been observed, which suggests that a fairly homogenous paste of gouge has been created and that subtle, localised changes in saturation (caused by uneven drainage) is unlikely to be the main cause of this effect.

The second scenario (2) is not supported by the measurement of the gouge thickness during experimentation. Even reduction in gouge thickness was observed, with more chaotic variations in thickness seen during unloading. This is contrary to the flow data, where chaotic flow is seen during loading and even variation seen during unloading. Therefore this effect is unlikely to be caused by uneven thicknesses of gouge.

The third scenario (3) is also not supported by experimental observations. Horizontal movement occurred as a result of only increasing normal load. However, this increases relatively evenly and suggests that changes in normal load have resulted in the gouge moving evenly.

Observations of localised flow suggests that gas exploits sub-micronscale features within the clay, similar to features observed in bentonite. The exact cause of the chaotic behaviour has not been determined due to the macro-scale of measurement and the likely microscopic origin of this behaviour. However, the chaotic behaviour is repeatable and suggests that gas flow predictions of transmissivity are problematic. The “even” reduction in flow on unloading supports the “memory” effect of the clay introduced in the previous section.

**Hysteresis in horizontal stress observed during unloading demonstrates the importance of the ratio between horizontal stress and vertical stress and its control on flow.**

Considerable hysteresis was also observed in horizontal stress during loading-unloading experiments for both water and gas injection. The repeatability of the results shows that free movement of the gouge was achieved. The hysteresis in horizontal stress during unloading may be attributed to the cohesive strength of the kaolinite clay gouge. The ratio of horizontal stress to vertical stress also showed hysteresis. Subtle variation between water and gas injection experiments was seen during unloading once the ratio exceeded unity. Significant gas flow rate increase occurred when the horizontal stress to vertical stress ratio increased above unity during unloading.

Zoback *et al.* (1985) and Brudy *et al.* (1997) have shown that the ratio of horizontal stress to vertical stress is crucial in controlling permeability and in the movement of gas through fractures. The close relationship between fracture flow and the horizontal stress to vertical stress ratio during the unloading stages in the present experiments also points towards its significance in understanding the flow of fluid through discontinuities. In the case of a fractured rock formation undergoing uplift stress relaxation is likely to result in a high horizontal stress to vertical stress ratio.

Understanding the horizontal stress to vertical stress ratio is important in predicting the flow properties of discontinuities. Features experiencing high horizontal stress to vertical stress ratios are expected to be more conductive. High horizontal stress to vertical stress scenarios are likely to be more prevalent in regions experiencing stress relaxation due to structural uplift or removal of the overburden. Again, this highlights that an understanding of the stress history of a discontinuity is essential to effectively predict the present fluid flow properties of those features.

**Differences have been observed between injection fluids (water and helium), especially the hysteresis observed in flow. For water injection flow is only partially recovered during unloading, whereas for gas enhanced flow is seen at low normal loads.**

Observations of shear stress during loading-unloading experiments show that the gouge mechanically behaves the same way if water or gas is injected into a saturated kaolinite gouge. The similarities suggest that the gouge is neither hydrated by water injection (as it is already fully saturated), nor is it desaturated by gas injection.

However, considerable differences are seen in flow behaviour. For water injection, a pore pressure of 1 MPa is sufficient to initiate flow, whereas a gas pressure in excess of 3.5 MPa is required to initiate flow. This results in much lower flow rates observed in water injection tests. The differences suggest that the governing physics controlling gas movement is dissimilar to that controlling water movement.

As previously introduced, there is also considerable difference in the progression of flow during the loading cycle. At low normal loads this behaviour is chaotic in gas injection, whereas it is smooth for water injection. By 1.5 MPa normal load the two behaviours are similar, both decaying evenly with increasing normal load.

Differences are also seen during the unloading cycle. Both injection fluids show a similar initial response with considerable hysteresis seen and the slow recovery of flow. Dissimilarity is seen as normal load reduces below approximately 1 MPa. For the case of water injection, flow is always only partially recovered. For gas injection, at low normal loads flow increases to high levels much greater than that recorded at the corresponding normal load on the loading cycle. The enhanced flow becomes catastrophic and at low normal loads all gas in the gas reservoir is expelled through the slip-plane. Such catastrophic failure during water injection was not seen. This may in part be due to the expansion of gas as it propagates along the slip-plane as pressure reduces.

## 7.2 GAS BREAKTHROUGH EXPERIMENTS

A total of 26 gas breakthrough experiments were conducted on 0°, 15°, 30°, and 45° discontinuities; both with and without active shear. All tests were conducted in an identical manner with a known starting volume of 200 ml of helium at 4 MPa and a pressure ramp created by constant flow displacement of the ISCO syringe pump by 700µl/h.

**During gas breakthrough experiments episodic flow/fault valve behaviour was seen with a decrease in subsequent peak pressures and the form of the pressure response was different during subsequent breakthrough events.**

A single test was conducted (ASR\_Tau06) for a prolonged gas injection ramp to see if there was repeat gas entry with a total of seven steps conducted. The exact detail of this particular test is complicated due to need to refill the gas reservoir several times.

The first gas breakthrough at 0.2 MPa normal load resulted in the sudden catastrophic loss of gas pressure at 3.2 MPa as the gas reservoir was emptied through the slip-plane. Normal load was increased to 1.85 MPa to see if a secondary breakthrough could be initiated following fracture sealing due to increased normal load. This resulted in a distinct peak in gas pressure at 1.9 MPa, which was followed by a decay to 1.2 MPa and then slow recovery of gas pressure to another breakthrough at 1.6 MPa. Pressure dropped to 0.5 MPa and again recovered to another breakthrough event at about 1 MPa. This partial breakthrough was followed by pressure recovery to a plateau of 1.1 MPa. Normal load was increased to 2.25 MPa and a fifth breakthrough was initiated at 1.8 MPa.

The form of the breakthrough event changed during the experiment. The first event was a catastrophic total loss of pressure. The second event was a peak and trough, similar in form to that seen during gas injection in bentonite. The third event was a sudden drop in pressure by 1 MPa, and the fourth event could be described as the system reaching equilibrium and the attainment of a plateau.

These observations suggest that “fault-valve behaviour” has been demonstrated in the laboratory and the magnitude of subsequent break-through events reduced (at constant normal load) and the “form” of the breakthrough events changed with each successive feature. It also demonstrates that an increase in normal load resulted in a degree of self-sealing, although the “memory” of previous breakthrough events may still be apparent.

**Repeat gas injection testing has shown a consistent gas entry pressure but considerably different, non-repeatable, gas peak pressures.**

For all fracture orientations, considerable non-repeatability was seen in the gas pressure response during repeat testing. Two methods were used to determine gas entry pressure. The first compared the observed gas pressure with the ideal gas law, whereas the second was calculated from the average flow at STP into the fracture. For most tests there was considerable difference between the two estimates. However, time-lapse photography suggests that the method used for average flow at STP into the fracture is closely determining the gas breakthrough pressure, whereas comparing the recorded gas pressure with the ideal gas law determines the gas entry

pressure. For both methods of determining the gas entry pressure there was repeatability in the results, with occasional anomalously low entry pressures.

Repeat gas injection testing has suggested that the physical control on gas entry is repeatable, although in the presence of any form of imperfection gas is able to enter at lower pressures. Once gas starts to move within the slip-plane the progression of pressure is less predictable and depends on whether the evolving gas network locates an exit from the system. Similar results are seen for all discontinuity orientations. Time-lapse photography has shown that gas pathways continue to evolve even after an exit has been established from the gouge.

#### **Differences in gas entry pressure are seen dependent on the orientation of the fracture.**

Although some tests have shown anomalously low gas entry pressures, a general variation of gas entry pressure with discontinuity orientation was observed. The highest gas entry pressure, as expected, was seen on a flat slip-plane with an entry pressure of 8.5 MPa. The lowest gas entry pressure was recorded at 15° of 7.75 MPa. Generally, the results suggest that the lowest gas entry pressure would be observed at 25°.

All tests have been conducted at identical vertical loads. As discontinuity orientation varies, the load acting normal to the slip-plane will vary. Taking this geometrical effect into account, the variation seen in gas entry pressure is more complex than a simple stress rotation about the slip-plane.

The experimental study has clearly demonstrated a variation in fracture transmissivity with discontinuity orientation. This experimental study demonstrates that the critical stress theory is applicable in the absence of stress relaxation.

#### **Shear can be seen to reduce the gas entry pressure.**

Tests conducted on slip-planes oriented to the direction of active shear showed a lower gas entry pressure for kaolinite and a rotation of gas entry pressure minimum to 38°. For water injection fracture transmissivity was seen to reduce due to self-sealing as a result of shearing. Therefore the reduction in gas entry pressure and observed increase in flow (as postulated from a reduced peak pressure) suggests that shearing in kaolinite has the opposite effect of self-sealing to gas.

### **7.3 GENERAL OBSERVATIONS**

#### **The results show that the flow of fluids through clay filled fractures is non-uniform and occurs via localised preferential pathways.**

Five tests were conducted and recorded using time-lapse photography to observe the escape of gas from the slip-plane into the bath of the apparatus. These showed that a small, isolated stream of bubbles escaped from a single location. In most tests a single stream of bubble was created, i.e. a single pathway and a second pathway either had not formed or did not reach the edge of the slip-plane. In all tests the frequency of escaping bubbles increased, as did the size of the bubbles.

Fracture width data were inconsistent in recording dilation events at the onset of gas flow. However, some tests clearly showed dilation. This observation combined with the isolated single bubble stream show that gas propagated by means of a dilatant process.

#### **The pressure recorded within the slip-plane showed a negligible fracture pressure and did not vary much in all tests.**

In all tests, the two pressure ports located within the slip-plane registered pressure less than 50 kPa, effectively close to zero. Little variation was seen, although some changes occurred during loading-unloading experiments as a result of consolidation. However, no evidence of elevated gas pressures were seen during any experiment. This strengthens the observation of localised dilatant pathways as opposed to a distributed radial migration of gas.

## 8 References:

British Geological Survey holds most of the references listed below, and copies may be obtained via the library service subject to copyright legislation (contact [libuser@bgs.ac.uk](mailto:libuser@bgs.ac.uk) for details). The library catalogue is available at: <http://geolib.bgs.ac.uk>.

- BÄCKBLOM, G, CHRISTIANSSON, R, and LAGERSTEDT, L. 2004. *Choice of rock excavation methods for the Swedish deep repository for spent nuclear fuel*. (SKB.)
- BARTON, C A, HICKMAN, S, MORIN, R, ZOBACK, M D, and BENOIT, D. 1998. Reservoir-scale fracture permeability in the Dixie Valley, Nevada, geothermal field. *SPE/ISRM Rock Mechanics in Petroleum Engineering*, Stanford University, Stanford, California, 299-306.
- BARTON, C A, HICKMAN, S, MORIN, R H, ZOBACK, M D, FINKBEINER, T, SASS, J, and BENOIT, D. 1997. Fracture permeability and its relationship to in-situ stress in the Dixie Valley, Nevada, geothermal reservoir. *Twenty-Second Workshop on Geothermal Reservoir Engineering*, January 27-29, Stanford University, Stanford, California.
- BARTON, C A, ZOBACK, M D, and MOOS, D. 1995. Fluid flow along potentially active faults in crystalline rock. *Geology*, Vol. 23, 683-686.
- BERGE, P A, BLAIR, S C, and WANG, H F. 1999. Thermomechanical effects on permeability for a 3-D model of YM rock. *Rock Mechanics for Industry, Vols 1 and 2*, 729-734.
- BOSSART, P, MEIER, P M, MOERI, A, TRICK, T, and MAYOR, J-C. 2002. Geological and hydraulic characterisation of the excavation disturbed zone in the Opalinus Clay of the Mont Terri Rock Laboratory. *Engineering Geology*, Vol. 66, 19-38.
- BOSSART, P, TRICK, T, MEIER, P M, and MAYOR, J-C. 2004. Structural and hydrogeological characterisation of the excavation-disturbed zone in the Opalinus Clay (Mont Terri Project, Switzerland). *Applied Clay Science*, Vol. 26, 429-448.
- BRUDY, M, ZOBACK, M D, FUCHS, K, RUMMEL, F, and BAUMGÄRTNER, J. 1997. Estimation of the complete stress tensor to 8 km depth in the KTB scientific drill holes: Implications for crustal strength. *Journal of Geophysical Research-Solid Earth*, Vol. 102, 18453-18475.
- BYERLEE, J. 1978. Friction of Rocks. *Pure and Applied Geophysics*, Vol. 116, 615-626.
- CUSS, R J. 1999. An experimental investigation of the mechanical behaviour of sandstones with reference to borehole stability. PhD thesis, University of Manchester.
- CUSS, R J, HARRINGTON, J F, GRAHAM, C C, SATHAR, S, and MILODOWSKI, A E. 2012. Observations of heterogeneous pore pressure distributions in clay-rich materials. *Mineralogical Magazine*, Vol. Geological Disposal of Radioactive Waste: Underpinning Science and Technology.
- CUSS, R J, MILODOWSKI, A E, and HARRINGTON, J F. 2011. Fracture transmissivity as a function of normal and horizontal stress: First results in Opalinus Clay. *Physics and Chemistry of the Earth, Parts A/B/C*, in press.
- EVANS, K F. 2005. Permeability creation and damage due to massive fluid injections into granite at 3.5 km at Soultz: 2. Critical stress and fracture strength. *Journal of Geophysical Research. B. Solid Earth*, Vol. 110.
- FERRILL, D A, WINTERLE, J, WITTMAYER, G, SIMS, D, COLTON, S, ARMSTRONG, A, and MORRIS, A P. 1999. Stressed rock strains groundwater at Yucca Mountain, Nevada. *GSA Today*, Vol. 9, 1-8.
- FINKBEINER, T, BARTON, C A, and ZOBACK, M D. 1997. Relationships Among In-Situ Stress, Fractures and Faults, and Fluid Flow, Monterey, Formation, Santa Maria Basin, California. *AAPG Bulletin*, Vol. 81, 1975-1999.
- GUTIERREZ, M, ØINO, L E, and NYGÅRD, R. 2000. Stress-dependent permeability of a de-mineralised fracture in shale. *Marine and Petroleum Geology*, Vol. 17, 895-907.
- HEFFER, K, and LEAN, J. 1993. *Earth stress orientation - a control on, and guide to, flooding directionality in a majority of reservoirs*. Reservoir Characterization III. (Tulsa: PennWell Books.)
- IKARI, M J, and KOPF, A J. 2011. Cohesive strength of clay-rich sediment. *Geophys. Res. Lett.*, Vol. 38, L16309.
- ITO, T, and ZOBACK, M D. 2000. Fracture permeability and in situ stress to 7 km depth in the KTB Scientific Drillhole. *Geophysical Research Letters*, Vol. 27, 1045-1048.
- JAEGER, J C, COOK, N G W, and ZIMMERMAN, R W. 2007. *Fundamentals of rock mechanics*. (Wiley-Blackwell.) ISBN 0632057599
- LAUBACH, S E, OLSON, J E, and GALE, J F W. 2004. Are open fractures necessarily aligned with maximum horizontal stress? *Earth and Planetary Science Letters*, Vol. 222, 191-195.
- MARRY, V, ROTENBERG, B, and TURQ, P. 2008. Structure and dynamics of water at a clay surface from molecular dynamics simulation. *Physical Chemistry Chemical Physics*, Vol. 10, 4802-4813.

- MATILLA, J. and TAMMISTO, E. 2012. Stress-controlled fluid flow in fractures at the site of a potential nuclear waste repository, Finland. *Geology*, 40, No.4, pp.299-302.
- MOGI, K. 2007. *Experimental rock mechanics*. No. 3. (CRC.) ISBN 0415394430
- REEVES, H. 2002. The effect of stress and fractures on fluid flow in crystalline rocks, Cumbria, UK. PhD thesis, University of Durham.
- ROGERS, S F. 2003. Critical stress-related permeability in fractured rocks. *Fracture and in-Situ Stress Characterization of Hydrocarbon Reservoirs*, Vol. 209, 7-16.
- RUTQVIST, J, BÖRGESSON, L, CHIJIMATSU, M, HERNELIND, J, JING, L, KOBAYASHI, A, and NGUYEN, S. 2009. Modeling of damage, permeability changes and pressure responses during excavation of the TSX tunnel in granitic rock at URL, Canada. *Environmental Geology*, Vol. 57, 1263-1274.
- RUTQVIST, J, and STEPHANSSON, O. 2003. The role of hydromechanical coupling in fractured rock engineering. *Hydrogeology Journal*, Vol. 11, 7-40.
- TALBOT, C J, and SIRAT, M. 2001. Stress control of hydraulic conductivity in fracture-saturated Swedish bedrock. *Engineering Geology*, Vol. 61, 145-153.
- TSANG, C F, BERNIER, F, and DAVIES, C. 2005. Geohydromechanical processes in the Excavation Damaged Zone in crystalline rock, rock salt, and indurated and plastic clays - in the context of radioactive waste disposal. *International Journal of Rock Mechanics and Mining Sciences*, Vol. 42, 109-125.
- WALTHAM, A.C. (1994) *Foundations of Enginerring Geology*. Blackie Academic & Professional, 88pp.
- ZOBACK, M D, MOOS, D, MASTIN, L, and ANDERSON, R N. 1985. Well bore breakouts and in situ stress. *Journal of Geophysical Research-Solid Earth*, Vol. 90(B7), 5523-5530.

## 9 Appendix I

Test	Fracture angle	+/-	Method 1			Method 2		
			Gas entry pressure (kPa)	Average entry pressure	+/-	Gas entry pressure (kPa)	Average entry pressure	+/-
0degs(5)	0°	0.5°	5000	8440	413	4772	4920	193
0degs(6)			8000			4610		
0degs(7)			9000			4590		
0degs(11)			7500			5475		
0degs(12)			9250			5170		
15degs(8)	15°	0.5°	7500	7580	72	4850	4840	48
15degs(9)			7500			4732		
15degs(10)			7750			4922		
30degs(1)	30°	0.5°	5200	7670	289	4373	4640	120
30degs(2)			8000			7380		
30degs(3)			7000			4700		
30degs(4)			8000			4839		
45degs(15)	45°	0.5°	8500	8000	354	5046	4980	212
45degs(16)			7500			5373		
45degs(17)			5000			4531		
0hi(13)	0° <sup>#</sup>	0.5°	7000	7500	354	4845	5420	408
0hi(14)			8000			6000		
0Shear(18)	0° <sup>@</sup>	0.5°	5500	5750	177	4620	4660	28
0Shear(19)			6000			4700		
30Shear(20)	30° <sup>@</sup>	0.5°	7000	7000	100	4700	4700	100
45Shear(21)	45° <sup>@</sup>	0.5°	5000	5000	100	4450	4450	100
15Shear(22)	15° <sup>@</sup>	0.5°	5250	5200	100	4830	4830	100

**Table 17** – Results for gas entry pressure for all gas injection experiments. # high pressurisation rate; @ with shear; Method 1 = gas entry determined from STP gas flow into the fracture; Method 2 = entry pressure inferred from comparing pressure curve with ideal gas law.